

# UNIVERSITA' DEGLI STUDI DI PAVIA

FACOLTA' DI INGEGNERIA  
DIPARTIMENTO DI INGEGNERIA INDUSTRIALE E DELL'INFORMAZIONE

DOTTORATO DI RICERCA IN TECNOLOGIE PER LA SALUTE, BIOINGEGNERIA E BIOINFORMATICA  
XXXIII CICLO - 2020

## DIGITAL 3D FUNCTIONAL ATLAS OF THE MOUSE OVARY

PhD Thesis by  
**GIULIA FIORENTINO**

Advisor:  
Prof. Maurizio Zuccotti

PhD Program Chair:  
Prof. Silvana Quaglini





“Chi vuole guardare bene la terra deve tenersi alla distanza necessaria.”

I. C.



---

# Acknowledgements

---

Vorrei ringraziare molte persone, che, in diverso modo, hanno contribuito al mio percorso e a questo lavoro.

Innanzitutto, ringrazio il Prof. Zuccotti e la Prof.ssa Garagna: il vostro esempio e la vostra esperienza sono stati per me un costante stimolo e una grande opportunità di formazione professionale e crescita personale.

Grazie a Mario, Valeria e Paola, che mi hanno sempre consigliato con saggezza, guidato con gentilezza e che, insieme a Cinzia e ai ragazzi di LBS, hanno reso il percorso più leggero.

Grazie alla Dott.ssa Annapaola Parrilli, per l'importante contributo dato a una parte di questo lavoro, e per aver sempre dimostrato un sincero interesse per la tematica di ricerca.

Grazie a Giulia, la prima persona a cui è toccato l'arduo compito di formarmi, che mi ha insegnato principi di cui faccio sempre tesoro.

Grazie a Davide e a Sara, persone imprescindibili, che mi hanno accompagnata in questo percorso con fedeltà, intelligenza e fiducia, sapendomi fornire il giusto sostegno, fondamentali consigli e un'adeguata dose di risate.

Infine, ringrazio i miei genitori, due modelli fuori dall'ordinario, che mi hanno insegnato il valore di curiosità, pazienza e determinazione, e che, con l'aiuto di Emanuele e Nicolò, mi hanno dimostrato quanto sia potente destrutturare la normalità e guardarne i singoli elementi da una prospettiva nuova.



---

## Abstract (Italiano)

---

L'infertilità femminile è una malattia che colpisce un numero crescente di donne. Secondo l'OMS, 1/3 delle donne sottoposte a chemio o radioterapia per il trattamento del cancro (~ 1 milione / anno negli Stati Uniti e ~ 300mila / anno in Italia o Regno Unito) sono a rischio di Insufficienza ovarica prematura. A questi dati si somma il 15% delle coppie infertili. La chiave per lo sviluppo di strategie per il trattamento dell'infertilità femminile è migliorare la nostra conoscenza del processo di follicologenesi, maturazione degli oociti e rimodellamento vascolare, in particolare per come si verificano nel loro contesto naturale tridimensionale (3D).

La maggior parte della nostra conoscenza di questi processi è stata ottenuta con approcci che portano alla perdita dell'integrità 3D dell'organo, alterandone così la naturale organizzazione spaziale degli eventi.

L'obiettivo principale del mio lavoro di tesi è stato costruire un modello 3D *in-silico* del piccolo ovario di topo e, a tal fine, ho progettato una pipeline organizzata in cinque fasi principali:

1. *Fissazione*: La prima fase della pipeline prevede l'isolamento e la fissazione dell'ovario in modo da poterlo riutilizzare per le successive analisi *ex-vivo*.

2. *Tomografia*: La tomografia computerizzata (CT) è un metodo di imaging basato sui raggi X che produce una vera ricostruzione 3D di un oggetto, con voxel cubici e risoluzione isotropa.

Inizialmente, l'imaging microCT dell'ovario di topo adulto ha consentito l'identificazione, la mappatura 3D e la conta dei follicoli dal secondario tipo 4 (T4) al preovulatorio T8, insieme alla ricostruzione del sistema vascolare principale. È importante sottolineare che i nostri risultati evidenziano che l'intera superficie ovarica ospita un numero uguale di ciascuna tipologia follicolare, suggerendo una distribuzione omogenea del loro reclutamento e della successiva crescita.

Ulteriori esperimenti sono stati condotti utilizzando l'analisi nanoCT dell'ovario prepuberale di topo. I risultati presentati sono i primi del loro genere e hanno consentito una caratterizzazione e localizzazione 3D estremamente accurata dei follicoli appartenenti a tutti gli stadi della follicologenesi, dal minuscolo T1 primordiale al T8 preovulatorio. Degna di nota è, inoltre, la possibilità di osservare chiaramente singole cellule e componenti subcellulari con una risoluzione vicino all'istologica (250 nm/pixel).

Presi insieme, i risultati di micro e nanoCT forniscono la prima ricostruzione isotropa 3D dell'ovario di topo, mantenendo bene la sua integrità e facilitandone l'ulteriore analisi con gli altri approcci descritti lungo la pipeline.

3. *Tissue clearing*: Il metodo di clearing iDISCO+ combinato con l'imaging 3D confocale dell'intero ovario di topo adulto, ha consentito l'identificazione di tutti i tipi di follicoli, dal T1 al T8, e del sistema vascolare fino ai capillari più sottili che circondano i singoli follicoli in crescita. Grazie all'utilizzo di marcatori molecolari, insieme ai risultati morfologici, questo approccio apre la possibilità di rivelare informazioni funzionali su specifiche strutture ovariche.
4. *Spettrometria di massa*: L'imaging con spettrometria di massa MALDI (MALDI-MSI) combinato con la cromatografia liquida LC-ESI-MS/MS ha permesso di studiare il proteoma dell'intero ovario di topo durante la follicologenesi e di identificare *in-situ* il profilo peptidico dei tipi follicolari.  
L'analisi LC-ESI-MS/MS ha generato una lista di 382 proteine, 75 delle quali svolgono un ruolo chiave nella biologia ovarica. L'analisi delle componenti principali (PCA) che confronta gli spettri di massa MALDI-MSI dei singoli tipi di follicolo con quelli dell'intera follicologenesi ha evidenziato la loro clusterizzazione e ha suggerito un cambiamento progressivo nel contenuto di peptidi durante la crescita del follicolo dal preantrale T5 al pre-ovulatorio T8. Inoltre, è interessante notare che la PCA ha mostrato la presenza di due distinti cluster all'interno della classe T8, e che questi, quando analizzati statisticamente, hanno rivelato 45 proteine differenzialmente espresse. Di queste, 9 hanno un ruolo specifico nella maturazione degli oociti e nello sviluppo preimpianto (ad esempio, fattori di effetto materno come DNMT1, NALP5 e KHDC3), suggerendo la presenza, all'interno del compartimento T8 pre-ovulatorio, di follicoli con diversa competenza allo sviluppo.
5. *Istologia*: Un ulteriore livello di indagine che ha lo scopo di far emergere informazioni cito-funzionali dall'intero ovario è dato dall'analisi istologica dell'organo che è stato precedentemente studiata con le metodologie sopra descritte. A tal fine, ho sviluppato un nuovo metodo, denominato Confocal Histology, che impiega la proprietà fluorescente dell'Eosina Y insieme ad un'analisi al microscopio confocale di sezioni istologiche di ovario di topo da 20 µm. Questo approccio ha consentito di definire una topografia di tutti i follicoli ovarici, da T1 a T8, con risoluzione estremamente elevata, e di classificare gli ovociti racchiusi secondo la loro organizzazione cromatinica.

In conclusione, i risultati di questo lavoro in più fasi servono come *proof-of-concept* e pongono le basi per la costruzione di un Atlante funzionale 3D digitale

dell'ovario di topo. Nel prossimo futuro, ho intenzione di utilizzare questa pipeline non solo per migliorare la nostra comprensione delle dinamiche della follicologenesi durante lo sviluppo dell'ovario in condizioni normali, ma la applicherò per studiare i cambiamenti che si verificano durante l'invecchiamento, in presenza di patologie o dopo somministrazione di ormoni o farmaci.

---

# Abstract (English)

---

Female infertility is a disease that affects an increasing number of women. According to the WHO, 1/3 of women that undergo chemo- or radiotherapy for cancer treatment (~1 million/year in the USA and ~300 thousand/year in Italy or UK) are at risk of Premature ovarian failure. These add up to a 15% of couples that are infertile. Key to the development of strategies to treat female infertility is to further our understanding of the process of folliculogenesis, oocytes maturation, together with vasculature remodelling, particularly as they occur in their natural three-dimensional (3D) environment.

Most of our knowledge of these processes has been obtained with approaches that lead to the loss of the 3D organ integrity, therefore altering the natural spatial organisation of the events.

The main objective of my thesis work was to build an *in-silico* 3D model of the tiny mouse ovary, and, to this end, I designed a pipeline organised in five main steps:

1. *Fixation*: The first and crucial step of the pipeline involves ovary isolation and fixation so that it can be used for subsequent *ex-vivo* analyses.

2. *Tomography*: Computed Tomography (CT) is an X-rays based imaging method which produces a true 3D reconstruction of an object, with cubic voxels and isotropic resolution.

At first, microCT imaging of the adult mouse ovary allowed the identification, 3D mapping and counting of the stages of follicle growth from the secondary type 4 (T4) to completion of folliculogenesis, and the reconstruction of the major vasculature. Importantly, our results highlight that the whole ovarian surface houses an equal number of each follicle type, suggesting a homogeneous distribution of follicle recruitment and subsequent growth.

Further experiments were done using the nanoCT analysis of the pre-pubertal mouse ovary. The results presented are the first of its kind and allowed an extremely accurate characterisation and 3D localisation of follicles belonging to all the stages of folliculogenesis, from the tiny primordial T1 to the pre-ovulatory T8. Noteworthy is, also, the possibility to clearly observe single cells and subcellular components with near-histological resolution (250 nm/pixel).

Taken together, micro- and nanoCT results provide the first 3D isotropic reconstruction of the mouse ovary, well maintaining its integrity and facilitating its further analysis with the other approaches described along the pipeline.

3. *Tissue Clearing*: The tissue clearing method iDISCO+ combined with the 3D optical confocal imaging of the whole adult mouse ovary allowed the identification of all follicle types, from T1 to T8, and of the vasculature down to the thinnest capillaries surrounding individual growing follicles. Thanks to the use of molecular markers, alongside with the morphological results, this approach opens the possibility to reveal functional information on specific ovarian structures.
  
4. *Mass spectrometry*: Here, I present the first attempt to use MALDI Mass Spectrometry Imaging (MALDI-MSI) combined with Liquid Chromatography Electrospray Ionization Tandem Mass Spectrometry (LC-ESI-MS/MS) to investigate the proteome of the entire mouse ovary during folliculogenesis, and to identify *in-situ* the peptide signature of the follicular types.  
LC-ESI-MS/MS analysis generated a reference list of 382 proteins, 75 of which playing a key role in ovarian biology. Principal component analysis (PCA) comparing the MALDI-MSI mass spectra of individual follicle types with those of the entire folliculogenesis highlighted their clustered localisation, and suggested a progressive change in peptide content during follicle growth from the preantral T5 to the fully-grown T8. Interestingly, PCA showed also the presence of two distinct mass spectra clusters in the T8 follicle class, that, when statistically analysed, revealed 45 proteins differentially present. Of these, 9 have a specific role in oocyte maturation and preimplantation development (e.g., maternal effect factors like DNMT1, NALP5 and KHDC3), suggesting the presence, within the pre-ovulatory T8 compartment, of follicles with different developmental competence.
  
5. *Histology*: A further layer of investigation that is intended to bring out cyto-functional information from the whole ovary is given by the histological analysis of the organ that has been previously studied with the methods described above.  
To this end, I developed a novel method, named Confocal Histology, which employs the fluorescent properties of Eosin Y together with a confocal microscopy analysis of 20 µm-thick mouse ovary histological sections. This approach allowed to define a topography of all the ovarian follicles, from T1 to T8, with extremely high resolution, and to classify the enclosed oocytes according to their chromatin organisation.

In conclusion, the results of this multi-step work serve as proof-of-concept and set sound bases for building a 3D functional Atlas of the mouse ovary. In the next future, I plan to use this pipeline not only for improving our understanding of folliculogenesis dynamics during the development of the ovary under normal conditions, but I will apply it to study the changes occurring during ageing, in the presence of pathologies or after hormones or drugs administration.



---

# Contents

---

<b>1. <i>In-silico</i> 3D functional reconstruction of the ovary .....</b>	<b>1</b>
1.1. <i>Purpose of a 3D functional reconstruction of an organ .....</i>	<i>1</i>
1.2. <i>Key tools available .....</i>	<i>2</i>
1.3. <i>The mammalian ovary.....</i>	<i>6</i>
1.3.1. <i>Anatomy and histology .....</i>	<i>6</i>
1.3.2. <i>Origin and development of the female gamete .....</i>	<i>8</i>
1.3.2.1. <i>From germ cells to primary oocytes .....</i>	<i>8</i>
1.3.2.2. <i>Folliculogenesis and gamete selection .....</i>	<i>8</i>
1.3.2.3. <i>The Surrounded Nucleolus (SN) and Non-Surrounded Nucleolus (NSN) oocyte model .....</i>	<i>11</i>
1.3.3. <i>Ovarian vasculature and neo-angiogenesis .....</i>	<i>12</i>
1.4. <i>Aim of the work: in-silico 3D functional reconstruction of the mammalian ovary.....</i>	<i>14</i>
1.4.1. <i>Why an in-silico 3D ovary .....</i>	<i>14</i>
1.4.2. <i>State-of-the-art .....</i>	<i>15</i>
<b>2. A novel pipeline for the in-silico 3D functional reconstruction of the mouse ovary .....</b>	<b>17</b>
<b>3. Tomography .....</b>	<b>21</b>
3.1. <i>Micro-Computed Tomography.....</i>	<i>21</i>
3.1.1. <i>PFA fixation and Lugol's solution staining represents an optimal preparation protocol for the ovarian microCT imaging .....</i>	<i>21</i>
3.1.2. <i>1.5 µm/pixel microCT of the adult mouse ovary shows follicles from the secondary T4 to the fully-grown T8 and corpora lutea, with subcellular details.....</i>	<i>23</i>
3.1.3. <i>Combined 3D rendering of microCT sections of the ovary and of the main vasculature .....</i>	<i>25</i>
3.1.4. <i>3D mapping of growing T4 to T8 follicles and corpora lutea to describe the trajectory of follicles recruitment and growth .....</i>	<i>26</i>
3.2. <i>Nano-Computed Tomography.....</i>	<i>29</i>
3.2.1. <i>NanoCT of the young mouse ovary shows follicles from the primary T3 to the fully-grown T8, with subcellular details .....</i>	<i>30</i>
3.2.2. <i>NanoCT analysis at 0.25 µm/pixel allows the completion of the tomographic reconstruction of folliculogenesis within the mouse ovary .....</i>	<i>33</i>
<b>4. Tissue Clearing combined with 3D optical imaging .....</b>	<b>39</b>
4.1. <i>The iDISCO+ clearing protocol combined with confocal microscopy allows the identification of all the different follicle types, from T1 to T8, in association with the surrounding capillaries meshwork .....</i>	<i>39</i>
<b>5. Mass spectrometry .....</b>	<b>45</b>
5.1. <i>LC-ESI-MS/MS analysis identifies the proteome of the mouse ovary..</i>	<i>45</i>

5.2. Follicles classification, counting and annotation of the corresponding MALDI-MSI mass spectra.....	47
5.3. Principal Component Analysis of MALDI-MSI mass spectra suggests follicle-specific peptide signatures during folliculogenesis.....	49
5.4. Receiver Operating Characteristic (ROC) analysis of T8 mass spectra highlights differences in the peptide content within the pre-ovulatory follicle class.....	59
<b>6. Histology .....</b>	<b>63</b>
6.1. Confocal histology.....	63
6.1.1. Two-photon microscopy brings up the fluorescent property of Eosin .....	63
6.1.2. Eosin stains the protein components of ovarian tissue, follicle cells and oocytes.....	66
6.1.3. Confocal microscopy reveals an accurate topography of follicles within the 20 µm-thick ovarian sections and describes the chromatin organisation of the enclosed SN or NSN oocytes .....	67
6.2. Classical histology .....	70
6.2.1. Hematoxylin and Eosin staining of ovarian sections pre-treated with Lugol's solution highlights the main vasculature and capillaries meshwork surrounding individual follicles .....	70
<b>7. Conclusions and future objectives .....</b>	<b>73</b>
<b>References .....</b>	<b>77</b>
<b>Appendix .....</b>	<b>91</b>
8.1. Animals and reagents .....	91
8.2. Micro-Computed Tomography.....	91
8.2.1. Ovaries preparation.....	91
8.2.2. MicroCT imaging and 3D model reconstruction .....	91
8.2.3. Histology .....	92
8.2.4. Follicle classification, counting and 3D localisation .....	92
8.2.5. Statistical analysis .....	93
8.3. Nano-Computed Tomography.....	93
8.3.1. Ovaries preparation.....	93
8.3.2. NanoCT imaging and 3D model reconstruction .....	94
8.4. Tissue clearing .....	94
8.4.1. Immunostaining and clearing.....	94
8.4.2. Confocal imaging.....	95
8.4.3. Data analysis .....	95
8.5. Mass spectrometry.....	95
8.5.1. Ovary fixation and slides preparation .....	95
8.5.2. MALDI-MSI .....	95
8.5.3. LC-ESI-MS/MS .....	96
8.5.4. Proteins identification .....	96
8.5.5. STRING (Search Tool for the Retrieval of Interacting Genes/Proteins) analysis .....	97
8.5.6. PubMed analysis .....	97

8.5.7. Statistical analyses .....	97
8.6. <i>Confocal histology</i> .....	97
8.6.1. Ovary preparation and staining .....	97
8.6.2. Two-photon imaging.....	98
8.6.3. Confocal imaging.....	98
8.6.4. Data processing and analysis .....	98
8.7. <i>Histology</i> .....	98
8.7.1. Ovary preparation and staining.....	98
8.7.2. Sections digitalisation and analysis .....	99



---

# Chapter 1

---

## ***In-silico* 3D functional reconstruction of the ovary**

### **1.1. Purpose of a 3D functional reconstruction of an organ**

In the last years, many efforts of the scientific community have been directed to the creation of *in-silico* three-dimensional (3D) functional reconstructions of entire organs or organisms capable to include morphological and functional information down to the single cell level and to their sub-cellular components.

These models aim to localise each single cell inside the organ and to integrate this spatial information with a wide range of functional features, such as differentiation trajectory, epigenetic modification and gene and protein expression signatures.

Only recently, the integration of advanced molecular and imaging techniques with an impressively high computing power allowed early attempts to translate and combine 2D anatomical images with functional data into organ 3D reconstructions.

Several network programs shared data obtained with the analysis of organ serial sections together with gene or protein expression datasets from tissue disaggregates. Amongst these programs, the eMouseAtlas ([www.emouseatlas.org](http://www.emouseatlas.org)), an interactive *in-silico* anatomy atlas adapted from the Kaufman's "The Atlas of Mouse Development" [1], gives the opportunity to look through hundreds of anatomical, histological, immunohistochemical and *in-situ* hybridisation images ranging from the 1-cell embryo to the adult.

Another noteworthy initiative is the "Allen Brain Atlas" (<https://portal.brain-map.org>), initiated in September 2003 and constantly updated, working towards the mapping of gene expression data in the neuroanatomy of mouse and human brains, in physiological or pathological conditions (i.e., Parkinson's, Alzheimer's, and Autism). The atlas aligns brain scans, medical and psychological data with *in-situ* hybridisation, that spatially localise gene expression patterns; thus, the resulting 3D morpho-functional model assigns to

each gene a specific 3D coordinate and figures out, in colours, which proteins are expressed in different regions. The project follows a policy gathered to open data, collaborative and multidisciplinary research, thus allowing scientists from any discipline to look at the findings while designing their own work.

More recent and ambitious is 'The Human cell atlas project' ([www.humancellatlas.org](http://www.humancellatlas.org)), launched in 2017 [2] and aimed at producing an interactive 3D atlas of each human cell type that could be used for predictive modelling and used to gain functional and structural information from the organ scale to the single-cell resolution. This project takes advantage of the newly developed single cell omics, a high-resolution approach used for the precise characterisation of metabolic and functional state of heterogeneous cell populations, to shed light on their intricate single-cell interplay [3]. However, this project still lacks reconstructed 3D models of each organ type as *in-silico* organ anatomical environments that incorporate the identity of each single cell type together with its spatial position. Comprehensibly, this step is, of the whole project, as much difficult as trying to characterise the specific molecular signature of each cell.

Altogether, these three atlases provide inspired visions, procedures, instrumentation and technical advancements that might serve as fundamental guidelines to promote and extend the *in-silico* 3D functional modelling to other organs, including mammalian gonads.

## 1.2. Key tools available

The *in-silico* 3D reconstruction of an organ is a multi-step process that requires an accurate combination of biological techniques and instrumentation with bioengineering tools and data processing software. The pipeline infers the geometrical 3D structure of the organ through four main steps, beginning with the collection of 2D serial images, their registration, segmentation and ending with 3D rendering (Figure 1).

1) Image acquisition: Images are acquired either on histological serial sections or directly on the entire organ using optical or tomographic sectioning. With histological samples, digitalisation is an additional step required to convert physical sections into a digital collection of images covering all the object volume. Digital histological slide scanners are a fast and reliable system for whole-slide acquisition. By optically scanning the histological slide, they create a 2D high-resolution digital image, with a magnification ranging from 20 to 40X. Alternatively, sections may be digitalised using a light microscope equipped with a motorised XYZ stage and a stitching software. A whole section is captured at high magnification in multiple tiles with partially overlapping margins. The overlapping regions are then used to direct a proper merging into a single wide-field histological image [4]. Among the available stitching system, Leica microscopes propose the LAS X Navigator. Instead, whole-organ optical sectioning is performed with confocal laser scanning microscopy (CLSM) or light-sheet fluorescence microscopy (LSFM), capable to acquire a

series of thin slices within the sample thickness, while removing the contribution of the out-of-focus light in each image plane. Samples are prepared either with whole-mount [5] or tissue clearing [6], [7] immuno-fluorescence, the latter more efficient with larger specimens. Tissue clearing methods make organs permeable to molecular markers and optically transparent by removing lipids, the main responsible components for refractive index inhomogeneity. Five different clearing approaches have been developed: solvent-based, aqueous-based, simple immersion, hyper-hydration or hydrogel-embedding [7]. Finally, tomography is a technique that, by using several types of penetrating electromagnetic waves, produces a true 3D reconstruction of an organ, with cubic voxels and isotropic resolution [8]. During scanning, the sample is rotated to collect 2D projections from different rotation angles. Then, these images are used to reconstruct stacks of tomographic sections across the total 3D volume. Moreover, tomography not only gives access to the inner structure of fixed objects but also to whole living organisms in their full complexity.

2) Registration: This is the process of alignment of points that are common in subsequent images to obtain a coordinated and coherent stack. This is a crucial step when 3D reconstruction is made from histological serial sections, but it is not required with confocal or tomographic images which are immediately available for segmentation and 3D visualisation. Two types of algorithms, the rigid [9] or the elastic [10] transformation, are the most commonly used and are implemented in both open source (e.g., ImageJ, NIH) and commercial (e.g., Amira or Avizo, Thermo Fisher Scientific) software. The rigid algorithm rotates and translates images to match pixels; instead, the elastic algorithm uses a scaling factor to stretch pixels and match them perfectly to those of a reference image.

In biomedicine, registration algorithms are also implemented in the field of multimodal imaging [11]. They are used to compute a spatial correspondence between images generated on the same sample with a sequence of different techniques to gain morphological and functional information.

3) Segmentation: Also called “annotation”, this process leads to the partitioning of a 2D image into multiple regions of interest (ROIs), each with a set of pixels that has a biological meaning. Segmentation can be performed using either one or a combination of the following five methods: *i*) the pixel-based method segments each pixel according to its grey intensity value (thresholding algorithm; [12]); *ii*) the edge-based method identifies and joins front pixels to form the ROI boundaries (level-set function; [13]); *iii*) the region-based method, instead, considers exclusively the grey levels of neighbour pixels and joins them together (region-growing algorithm; [14]); *iv*) deep learning technologies, capable of highlighting hidden patterns, unseen by the naked eye, and use them for improved structure identification (convolutional neural network; [15]); *v*) a manual approach. The last two methods are often required due to the complexity of segmentation of certain biological structures, such as the ovary itself. Among the different software employed, ImageJ, ITK-SNAP

(UPenn and UNC), 3D Slicer (NIH), Imaris (Oxford Instruments) and Amira or Avizo implement segmentation algorithms.

4) 3D rendering: This term refers to Computer Graphics methods that use lightening and shading techniques to represent, on a two-dimensional monitor, the 3D volume and the depth of the analysed organ. Following ROIs segmentation, 3D rendering of an organ is achieved using two main algorithm families: The Surface Rendering (SR) and the Volume Rendering (VR) [16]. SR uses a mesh of polygons capable to approximate an isosurface from the segmented perimeter of the organ, resulting in a final object with an opaque and luminous surface. For example, the *marching cubes* is the most commonly used SR algorithm for extracting isosurfaces from a dataset [17], [18]. Rather, VR shows not only the surface of an organ, but also its internal biological characteristics. VR algorithms, such as volume ray casting, work on voxels - three-dimensional counterparts of the two-dimensional pixels - by exploiting their shading, opacity and colour features codified through RGBA values (Red, Green, Blue, Alpha, the latter specifies the opacity). 3D rendering of histological sections presents drawbacks when trying to infer tissue structures within the section thickness, as the interpolation performed to join two serial sections remains the trickiest step to solve. Among the different software employed, ImageJ, ITK-SNAP, 3D Slicer, Imaris and Amira or Avizo implement 3D rendering algorithms.

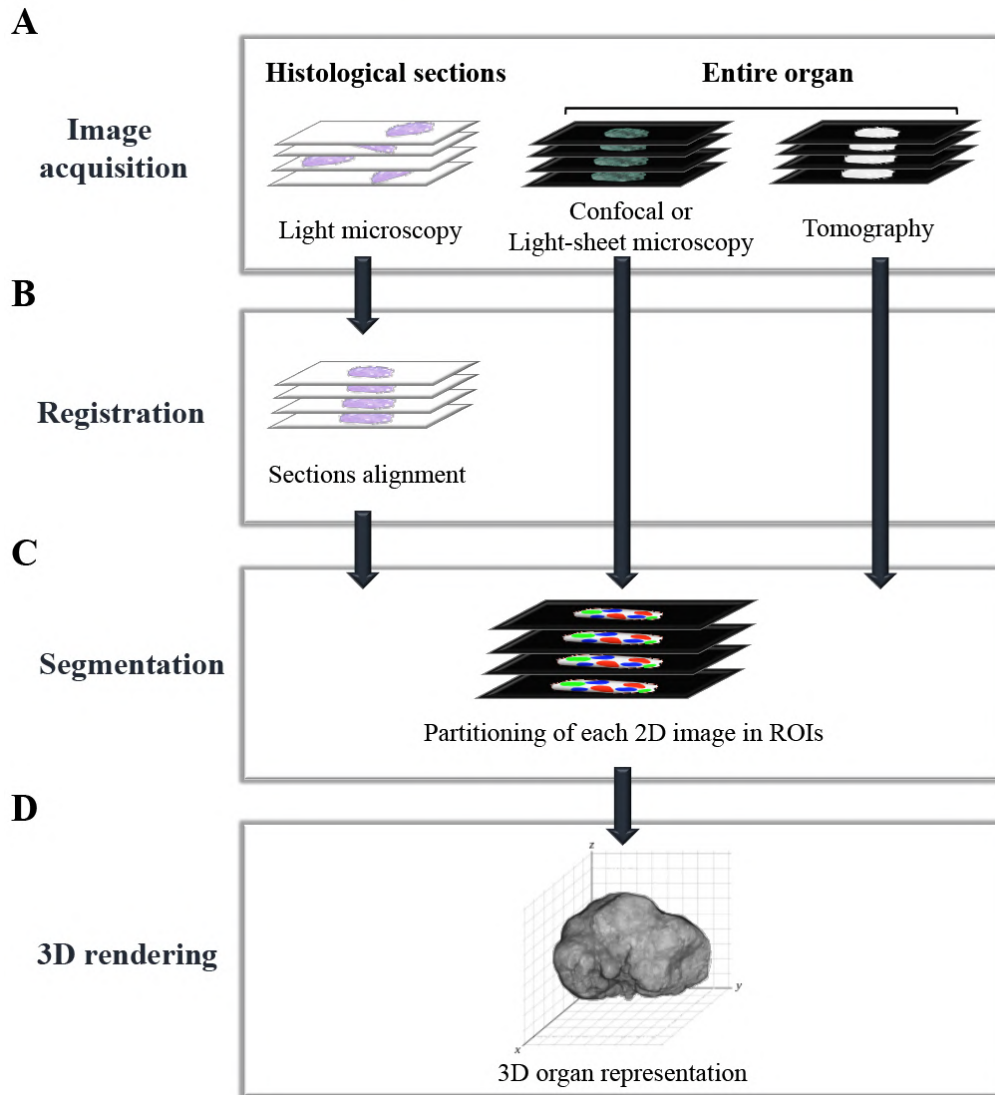


**Figure 1. Four main steps of the *in-silico* organ 3D reconstruction pipeline.** **A)** Image acquisition is performed either from histological serial sections with light-microscopy or directly on the whole organ using optical or tomographic sectioning. **B)** Registration, a required processing for the 3D reconstruction from histological sections, aligns points that are common in subsequent images to obtain a coordinated and coherent stack. **C)** Segmentation is the process of partitioning each 2D image into multiple regions of interest (ROIs) with a specific biological meaning. **D)** 3D rendering, the final step, gives a representation of organ 3D volume and depth by modulating light, shades and transparency.

## 1.3. The mammalian ovary

### 1.3.1. Anatomy and histology

The mammalian ovary is a small paired organ of flattened oval shape located in the pelvic region on either side of the uterus; it has a dimension of about two per one per one millimetre in adult mice, while it is larger in humans.

The surface of the ovary is constituted by the germinal epithelium of cuboidal cells, which covers a thick capsule of connective tissue, named tunica albuginea.

The internal ovarian tissue mainly consists of a fibrous stroma highly differentiated in the most external cortex and the internal medulla. For their cellular and extracellular composition, these two main histo-functional regions have different overall mechanical properties and stiffness. These regions are, also, characterised by the presence of a different follicular component. Specifically, the cortex is the stiffest portion of the ovary that houses numerous small follicles and tiny capillaries; the medulla, instead, is located in the centre of the organ and provides a softer environment that hosts growing follicles and the largest vasculature branches (Figure 2).

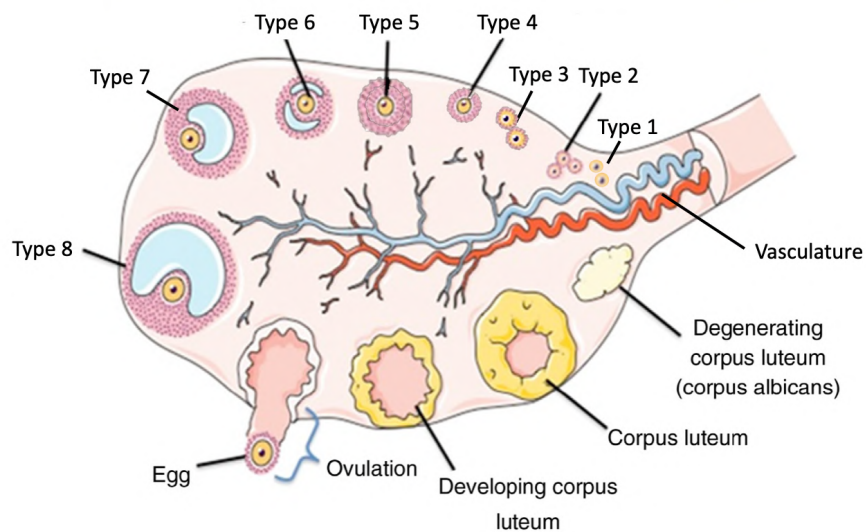


**Figure 2.** Schematic representation of the mammalian ovary showing the external cortex region, rich in follicles, and the internal medulla, highly supplied by blood vasculature.

The ovarian follicle is the essential functional unit, composed by an oocyte surrounded by follicular cells, and its growth is tightly associated with the correct maturation of the female gamete [19]. An accurate classification of the stages of follicle growth was proposed by Pedersen and Peters [20] (Figure 3), which identified eight follicle types based on their size and histological

characteristics. By observing the ovarian tissue under the microscope, type 1 (T1) and type 2 (T2) follicles, also known as small primordial, are constituted by a 15-20  $\mu\text{m}$  diameter oocyte surrounded by few or a complete layer of flattened granulosa cells, respectively. Type 3 (T3) primary follicles, instead, have a diameter of 30  $\mu\text{m}$ , with the oocyte surrounded by a complete ring of cuboidal follicle cells. T3 follicles are additionally divided into type 3a and 3b on the basis of the number of cuboidal follicle cells, which is less than 20 cells or between 20 and 60 on the largest cross-section, respectively. After the beginning of growth, type 4 (T4) secondary follicles have a size in diameter of 60  $\mu\text{m}$  and are surrounded by two complete layers of follicle cells, from 61 to 100 on the largest cross-section. At this stage, the growing oocyte begins to be covered by a specialised extracellular matrix named zona pellucida (ZP). Type 5 (T5) follicle is a transitory stage characterised by increasing layers of granulosa cells and the formation of a theca, an additional somatic cell layer that begins to be vascularised and supports folliculogenesis by synthesising steroidal hormones [21]. Type 5 stage is furthermore distinguished in type 5a and 5b on the basis of the number of granulosa cells in the largest cross-section, ranging from 101-200 in T5a to 201-400 in T5b. In type 6 (T6) follicles the formation of an antrum filled with follicular fluid begins, and they reach a diameter of 150  $\mu\text{m}$  in size. Type 7 (T7) is a large fully-grown follicle with a diameter of 300  $\mu\text{m}$  in size and more than 600 cells on the largest cross-section. Notably, some of these cells strictly surround the oocyte and form the cumulus oophorus. The pre-ovulatory type 8 (T8) follicle shows a single antrum cavity, a size in diameter of 400  $\mu\text{m}$  and is ready to ovulate a large and mature oocyte of about 80  $\mu\text{m}$  in diameter surrounded by cumulus cells.

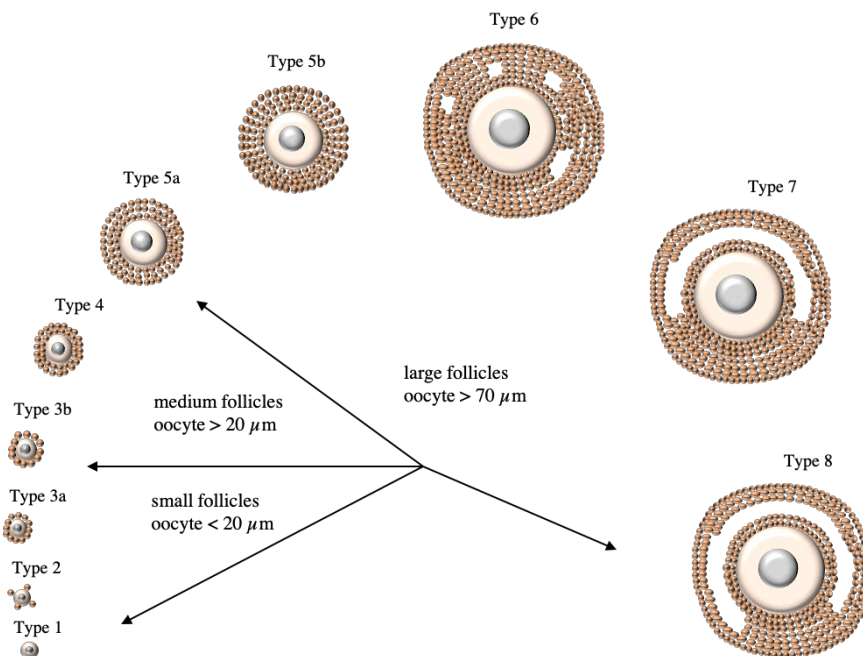


**Figure 3.** Classification of follicles and oocytes during their growth and maturation, from the primordial type 1 to the pre-ovulatory type 8 follicle.

## **1.3.2. Origin and development of the female gamete**

### **1.3.2.1. From germ cells to primary oocytes**

In the mouse, oogenesis begins during foetal life, when about forty PGCs migrate from the allantoic region of the 7.5 day *post coitum* (dpc) embryo to the genital ridges, where they undergo repeated and incomplete divisions to form cysts enclosing up to thirty interconnected germ cells [22], [23]. At 12.5 dpc oogonia will enter meiosis I and the cysts undergo breakdown until soon after birth [24]. At the early stages of meiosis, oogonia and oocytes are linked by intercellular bridges that allow the exchange of proteins and important substances, like hormones, through their cytoplasm. In the mouse and other Mammals, like rabbit, cow and sheep, these intercellular connections drive the synchronous divisions of germ cells [25]. Primary oocytes continue meiosis I until they reach the diplotene stage (E14.5), where meiotic arrest occurs. With the beginning of puberty, pools of primary oocytes periodically re-engage in meiosis, concluding meiosis I during ovulation. The divisions that occur in cytokinesis I are asymmetrical, resulting in the formation of two different cells: a large secondary oocyte, a haploid cell (1n, 2c) which contains the majority of the initial cytoplasm, and a small polar body (1n, 2c).

At each cycle, a group of about forty oocytes undergo maturation, most of them undergo atresia, while few ovulate into the fallopian tube where, if sperm are present, fertilisation can occur. After fertilisation, the oocyte completes meiosis II, by the end of which the second polar body is expelled. Finally, the mature oocyte is a haploid cell, meaning that each of its chromosomes consists of a single chromatid (DNA content = 1c). Instead, if the secondary oocyte does not undergo fertilisation, the second meiotic division does not occur, and the oocyte is discharged from the body through menstruation.

### **1.3.2.2. Folliculogenesis and gamete selection**

Folliculogenesis is the biological process that leads the maturation and complete growth of the follicular structure together with the enclosed oocyte. The folliculogenetic process is tightly regulated by biomechanical forces combined with exogenous and endogenous hormonal control (Figure 4), and it is coordinated and coupled with oogenesis through gap junction communications.

In Mammals, the initial recruitment of primordial follicles from the resting ovarian reserve is a gonadotropin-independent process driven by mechanical forces of the cortical extracellular matrix (ECM) [26].

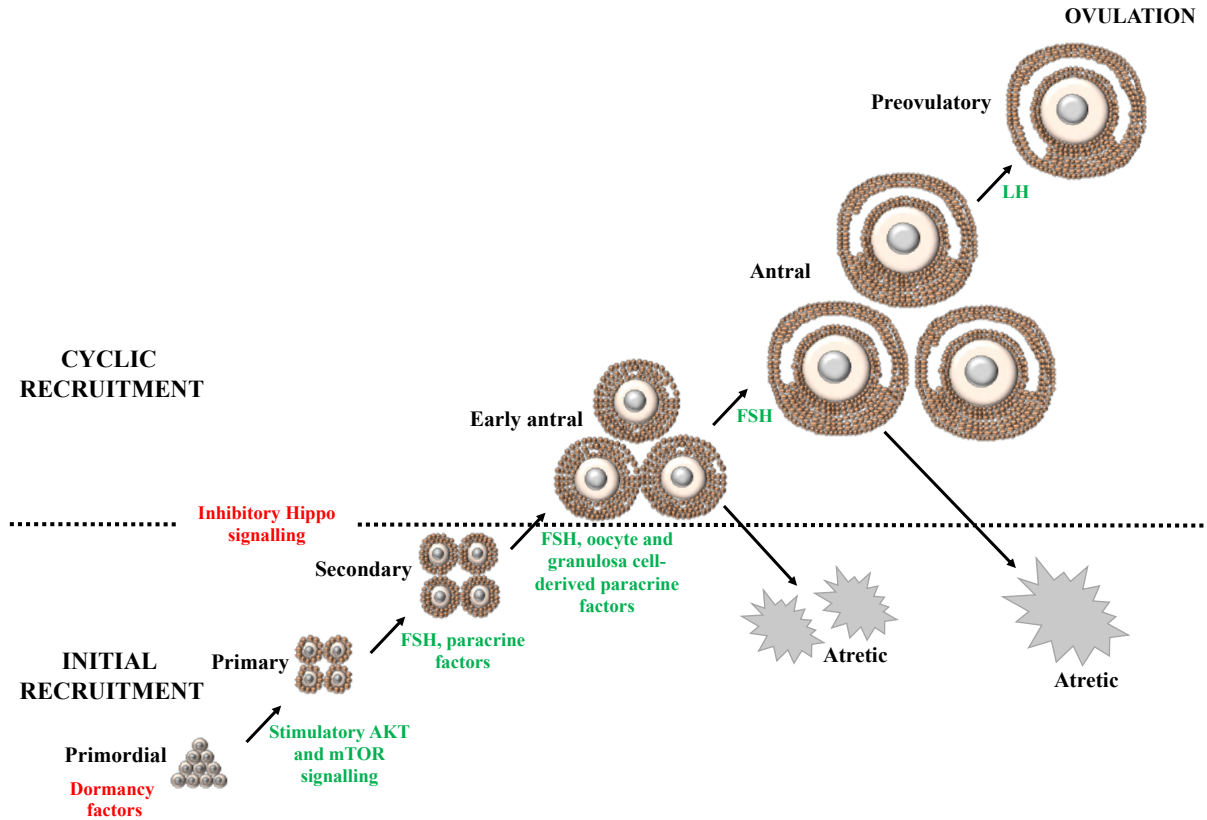


**Figure 4.** Schematic representation of the initial and cyclic recruitment of follicles occurring to accomplish folliculogenesis, with in red the inhibitory factors, and in green the main regulative players.

A higher degree of stiffness in the cortical region, sensed by integrins mechanoreceptors, causes the activation and the inactivation of Hippo and Akt pathways, respectively [27], [28], [29]. This transcriptional change triggers, through a cascade of molecular events involving the PI3K/AKT signalling pathway, the transition from quiescence to follicle activation [30]. Thus, primordial follicles initiate their growth (Figure 5), the enclosed oocytes increase their size and start to produce zona pellucida components (ZP; a glycoprotein layer required for fertilisation and embryo pre-implantation development), the surrounding granulosa cells differentiate toward a more cuboidal shape and proliferate until the oocyte is surrounded by two or more layers of cells, forming secondary (T4) and larger preantral follicles (T5), respectively. Starting with sexual maturity, the hypophysis releases the Follicle Stimulating Hormone (FSH), whose action leads to the cyclical recruitment of a group of early antral follicles for the subsequent stages of folliculogenesis [26], [31]. At this point, among granulosa cells, some cavities containing follicular fluid, rich in metabolites and hormones [19], start to form and follicles enter the antral stage (T6). Gradually, the small cavities aggregate to form the unique antrum of the fully-grown (T7) and pre-ovulatory (T8) stage. In this phase, the action of FSH drives the induction on granulosa cells of receptors for

the Luteinizing Hormone (LH), whose surge leads to the completion of the first oocyte meiotic division, the follicle rupture and ovulation [30], [32]. Few follicles, in poly-ovulatory species (i.e., mouse) or only one, in mono-ovulatory species (i.e., human), will express a number of LH receptors sufficient to be ovulated [33], [19]. Whether or not follicles will reach ovulation depend on the frequency and amplitude of LH pulses induced in the pituitary [34], [19]. Those follicles receptive to LH start to produce oestradiol, leading to a drop of FSH concentration and a atresia of the rest of the antral follicles.

After ovulation, the follicle degenerates into a *corpus luteum* (CL), a highly differentiated endocrine structure formed by the residual follicle cells, that specialises in progesterone synthesis throughout fertilisation until the placenta will be able to start its own production; whereas, if fertilisation does not occur, this structure progresses in *corpus albicans* leading to a fall of progesterone and an increasing surge of FSH concentration [35].

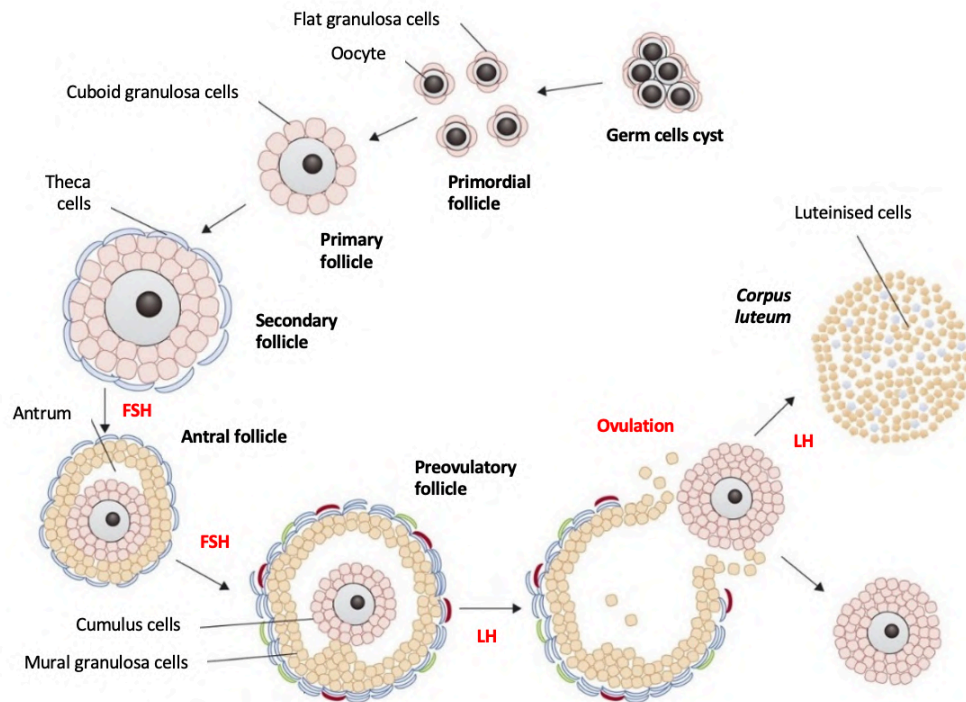


**Figure 5.** The process of folliculogenesis, from the formation of germ cells cyst, through all the stages of follicle growth, ovulation and *corpus luteum* development (modified from [36]).

During each folliculogenetic cycle, only few antral follicles reach the pre-ovulatory stage; the remaining follicles undergo atresia, a form of programmed cell death, and arrest their growth mainly during the transition from the preantral to the antral stage [37], [38].

### 1.3.2.3. The Surrounded Nucleolus (SN) and Non-Surrounded Nucleolus (NSN) oocyte model

Within the antral follicle compartment of the great majority of the mammalian ovaries (mouse and human included [39]) two different types of oocytes have been identified based on their chromatin organisation. Indeed, after isolation from antral follicles and staining with Hoechst 33342 (a supravital fluorochrome that binds to the A-T rich regions of the DNA), they can be distinguished in surrounded nucleolus (SN) oocytes, characterised by a ring of Hoechst-positive chromatin condensed around the nucleolus (Figure 6A), and non-surrounded nucleolus (NSN) oocytes, with a more dispersed chromatin organisation (Figure 6B).

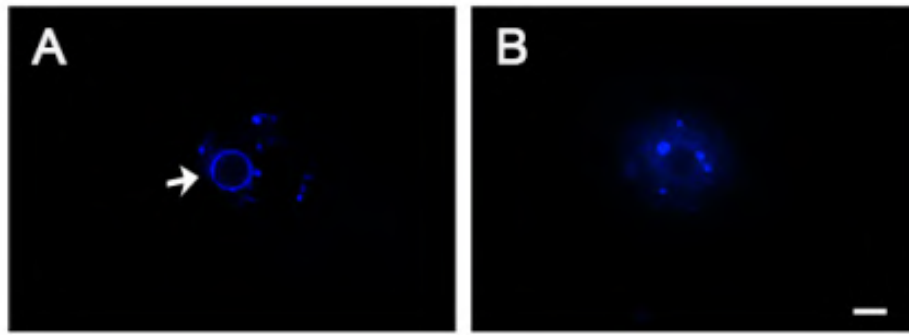


**Figure 6.** Mouse antral oocyte nucleolus stained with Hoechst 33342. **A)** Surrounded Nucleolus (SN) oocyte; **B)** Non-Surrounded Nucleolus (NSN) oocyte. Bar, 5  $\mu\text{m}$ .

During folliculogenesis the amount of SN and NSN oocytes varies on the basis of the different phases of ovarian cycle. In the mouse, NSN oocytes are present from the early stages of primordial follicles, in which oocytes have a diameter of 10-40  $\mu\text{m}$ , while SN oocytes presence is observed in a later stage, since the cells reach a diameter of 40-50  $\mu\text{m}$  [32]. The differences described above have a huge biological meaning, since they have been associated with the oocyte developmental competence. In fact, when fertilised, only SN oocytes reach the blastocyst stage and may develop to term, whereas NSN oocytes arrest development at the two-cell stage [40], [41], [42].

### **1.3.3. Ovarian vasculature and neo-angiogenesis**

The ovary is supplied by a complex vascular system: the ovarian branch of the abdominal artery enters the organ at the hilum site, where it divides into smaller arterioles, that, then, cross the medulla region, reaching the cortex as thin capillaries, and enveloping individual growing follicles within a meshwork [43].

This rich dynamic network of blood vessels delivers follicles with oxygen, growth factors, gonadotrophins and steroid precursors to sustain their growth and regulate their fate of survival or atresia [44]. In literature, there are evidences that a denser and more permeable vasculature correlates with the development of an healthy follicle, as it occurs for the abundant meshwork surrounding the selected dominant follicle in mono-ovulatory species [45], and that, on the contrary, a degenerating capillary meshwork surrounding a follicle is a sign of atresia [46]. Besides this gross knowledge, the complex functional relationship among vasculature and growing follicles continues to be poorly understood.

At each cycle, the process of neo-angiogenesis plays a role of paramount importance in guiding vasculature remodelling around growing follicles (Figure 7; [47]), making the ovary a unique example of organ that undergoes a physiological cyclical angiogenesis, whose activation in the adult usually occurs after a wound or is restricted to tumours development [48].

The stromal vasculature, made of small calibre arterioles, sustains, by passive diffusion, the metabolic activity of primordial through secondary follicles [49]. When follicles reach the preantral stage, FSH stimulates the surrounding theca cells to produce and release several pro-angiogenic factors outside the follicle into the stromal compartment. Among them, a diffusion gradient of VEGFA (Vascular endothelial growth factor A), sensed by the VEGFR2 receptor on proximal vascular endothelial cells, has a key role in the activation of the NOTCH pathway, that, in turn, triggers the sprouting of new capillaries towards individual growing follicles [50], until the formation of two main concentric networks of vessels [51]. At the late pre-ovulatory follicle, an inner concentric network of capillaries undergoes first a sprouting across the granulosa cells layer, and, then, initiates an extensive proliferation towards the internal portion of the follicle to supply with oxygen and macromolecules both the somatic and germ cell components in preparation to oocyte ovulation [52]. Also, sequential contractions of the capillaries surrounding the pre-ovulatory follicle determine local changes of blood pressure that favour the apical rupture during ovulation [53].

Immediately after, the increased activity of the VEGFA-VEGFR2 signalling pathway in the remaining CL induces a strong blood vessels proliferation needed to accomplish its endocrine function and its gradual regression [54], [55].

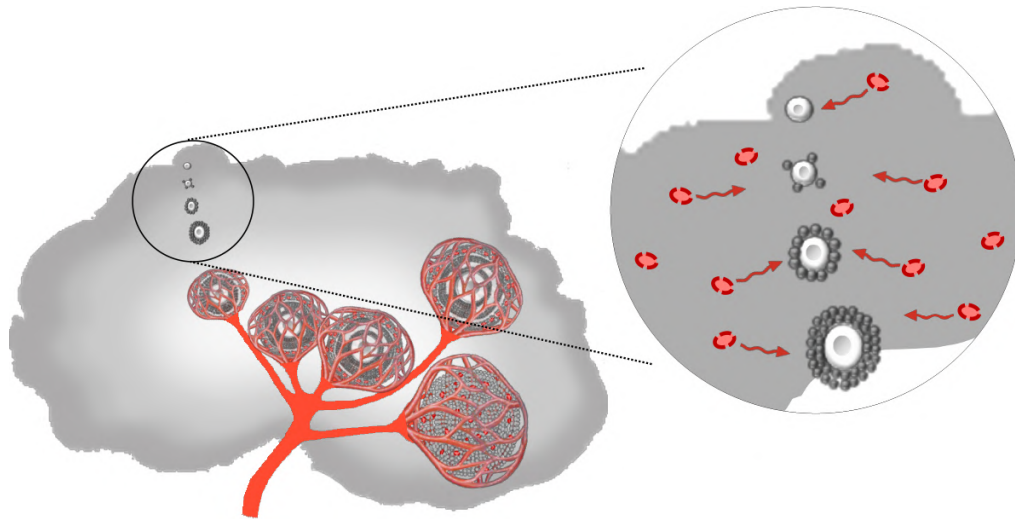


**Figure 7. Remodelling of the blood vasculature during folliculogenesis.** A rich network of capillaries contributes to supply follicles with oxygen, nutrients and signalling molecules throughout folliculogenesis. During the initial stages of follicle growth, from primordial to secondary, this contribution occurs through a passive diffusion mechanism (enlargement, wavy arrows); then, after recruitment, a meshwork of capillaries, generated thanks to a process of neo-angiogenesis, encapsulates each follicle and *corpus luteum*.

The physiological process of neo-angiogenesis is extremely important for the correct function of the organ, in particular during follicle recruitment, growth, and survival; but also for the production of developmentally competent oocytes and the creation of a CL [57]. A dysregulation of neo-angiogenesis can lead to infertility, ovarian cancer and several ovarian disorders, such as Polycystic Ovary Syndrome (PCOS), Ovarian Hyperstimulation Syndrome (OHSS) and Massive Ovarian Oedema (MOO) [56].

## **1.4. Aim of the work: *in-silico* 3D functional reconstruction of the mammalian ovary**

### **1.4.1. Why an *in-silico* 3D ovary**

Female infertility is a disease of the reproductive system that affects an increasing number of women. According to the WHO, 1/3 of women that undergo chemo- or radiotherapy for cancer treatment (~1 million/year in the USA and ~300 thousand/year in Italy or UK) are at risk of Premature Ovarian Failure (POF). These add up to a 15% of couples that are infertile [58]. Key to the development of strategies to treat female infertility is to further our understanding of the process of folliculogenesis and oocyte maturation, particularly as they occur in their natural 3D environment.

The mammalian ovary is a highly dynamic organ that cyclically undergoes morpho-functional changes. At birth, it contains thousands of follicles, but only hundreds, during the reproductive period of an individual, will complete their growth to eventually ovulate a mature oocyte. All the others will be eliminated at some point during folliculogenesis. Most of our understanding of the process of follicle growth and oocyte maturation and selection has been obtained with approaches that lead to the loss of the 3D integrity of the organ, therefore altering the natural spatial organisation of the events occurring during the accomplishment of ovarian functions. Specifically, the ovary is disaggregated into its follicular units, which are either directly analysed with molecular biology techniques, further matured *in vitro*, or cultured in media containing matrices with the aim of maintaining the follicle 3D organisation [59], [60]. Alternatively, the female gonad is fixed and sectioned for histological or immunohistochemical studies to extract 2D anatomical or functional data, respectively.

During the last decades, a number of studies proposed evidences that the correct follicle growth and acquisition of oocyte developmental competence are strictly related to a continuous, but still poorly understood, remodelling of the ovarian tissue and vasculature [61], [56], [62], as well as a crosstalk between follicle cells and oocytes [32], [63].

The aim of my thesis work is to present the 3D analysis and reconstruction of the mammalian ovary as an approach that could not only further improve our understanding of its tissue architecture, but, when combined with specific functional markers, it would help to reveal the multidimensional flow of molecular information that contributes to its biological function.

To this end, I designed and propose here a novel pipeline for the 3D morpho-functional analysis and reconstruction of the mouse ovary. This is a multi-step work finalised to obtain an *in-silico* 3D model that will provide the spatial coordinates to precisely localise functional data with different resolution levels, from tissue-specific immunohistochemical details, through protein and gene expression profiles, and single-cell data, laying the foundation for the creation of a 3D Atlas of the mammalian ovary. This Atlas would contribute to our

comprehension of folliculogenesis dynamics, not only during the developmental of the organ under normal conditions, but, importantly, during ageing, in the presence of pathologies or after hormones or drugs administration.

Furthermore, the results obtained might be used to design an educational tool that combines an interactive informatic platform and 3D printed hand-held models, to enable visual inspection and direct manipulation of ovaries under normal or pathological conditions.

### **1.4.2. State-of-the-art**

During the past five years, using 3D optical imaging, tomography or 3D histology techniques, a few studies attempted a 3D analysis and representation of the intact mammalian ovary at different embryonic and postnatal stages, under normal or pathological conditions. Among these, eight completed the whole four steps of the reconstruction pipeline (described in Chapter 1.2), from image acquisition, registration (when needed), segmentation and rendering, up to the proposal of 3D models of the ovary. Although these investigations allowed to revisit, or study for the first time in a 3D framework, some aspects of oocytes and follicles maturation as well as blood vessels formation and remodelling in the normal or pathological ovary, in foetus or in the adult, the 3D modelling proposed is still preliminary and sometime rudimental.

Specifically, tissue clearing combined with optical imaging allowed the acquisition of molecular details on the inside 3D organisation of the ovary, describing *i*) the temporal, spatial and quantitative dynamics of the oogenetic process, from the entry of oogonia into meiosis (foetus) to the first follicles recruitment (puberty) and their subsequent maturation (adult) [64], [65], [66], [67], [68], and *ii*) the 3D relationship between growing follicles and their surrounding capillaries [67], [69]. Worth of mentioning among the studies of this kind is that performed by Feng et al. [67] which, by using the CLARITY tissue clearing method [70] combined with an advanced image processing tool (Imaris), described and produced *in-silico* models of the spatial relationship between follicles during mouse life, from birth to senescence, and the ovarian blood vessels remodelling throughout folliculogenesis in a 3D context. By applying the Imaris Spot transformation algorithm on 3D images, this approach allowed the semi-automated segmentation and counting of the different follicle types confirming an age-dependent follicle loss. Furthermore, the tracing of the PECAM1 fluorescent signal (an endothelial cell marker) with the Imaris Filament algorithm, allowed the modelling of a follicle-vasculature spatial interaction map, which showed that *i*) follicles are not randomly distributed inside the organ volume, but are located along main vasculature branches; *ii*) after FSH-mediated follicle recruitment, the avascular primordial follicles start growing and initiate secretion of the vascular endothelial growth factor A (VEGFA) to promote neo-angiogenesis; *iii*) in VEGFA mutant mice or in mice treated with axitinib, a VEGF receptor-targeted tyrosine kinase inhibitor, vasculature remodelling is arrested, thus impairing ovulation.

Although this approach highlighted crucial aspect of the ovary biology, the optical imaging remains limited to the production of distorted 3D models of the organ, stretched out along the z-axis, due to the lack of an equal resolution on the three axes [71], [72].

Conversely, the tomographic approaches attempted to reconstruct the folliculogenetic process inside the volume of the ovary with ultrasonography [73], [74], [75], micro-Magnetic Resonance Imaging (MRI; [76]), laboratory-based X-ray micro Computed Tomography (microCT; [77]) and phase contrast CT [78] were intrinsically capable to generate 3D models with isotropic resolution, but provide an uneven anatomical characterisation of the organ, with the only identification of follicles present in the pre-ovulatory compartment. A single study used synchrotron radiation CT (SR-CT; [79]) to localise smaller growing follicles generically assigned to the preantral stages.

Although the number of studies conducted so far is small, the results obtained already show the importance of working on 3D modelling of the gonads and highlight how this perspective will improve our knowledge on several key features of ovary biology.

Altogether, these researches disclose the potentialities of a 3D approach to gain insights into the biology of the ovary, and, also, to propose key technical novelties along all the steps of the reconstruction process, from image acquisition to the optimisation and development of new image processing tools.

---

# Chapter 2

---

## A novel pipeline for the *in-silico* 3D functional reconstruction of the mouse ovary

During the three years of Ph.D., I collaborated with biologists and engineers of the University of Pavia and of public and private research centres - including the Center of X-ray Analytics Empa (Zurigo, Switzerland) where I spent a two-month training period - to define a novel pipeline of methodologies pertaining to different expertise to be applied for the analysis of a single ovary.

In this Chapter I will give an overview of the rationale behind the pipeline designed, and, then, I will describe the six different specific technologies selected to study the ovary, highlighting their main principles and strengths.

The pipeline implies the effort to combine very recent biological and engineering technologies with more traditional techniques revisited in an innovative way. The idea is to reuse the same fixed ovary for sequential 3D and 2D morpho-functional imaging analyses combined with data processing through bio-engineering tools, aiming at integrating different information into an *in-silico* 3D model.

Figure 8 shows the overall design in which, after fixation, the same ovary undergoes non-disruptive techniques, as tomography and tissue clearing, which analyse the entire organ maintaining its tridimensionality; then, the ovary is processed to obtain histological sections to investigate specific molecular aspects, such as the protein signature of each follicle type with mass spectrometry or the oocytes chromatin organisation as marker of developmental competence. Next, the data obtained at these different investigation levels, from follicular to single-cell scale, might be represented and integrated into the coherent reference space of each single analysed ovary.

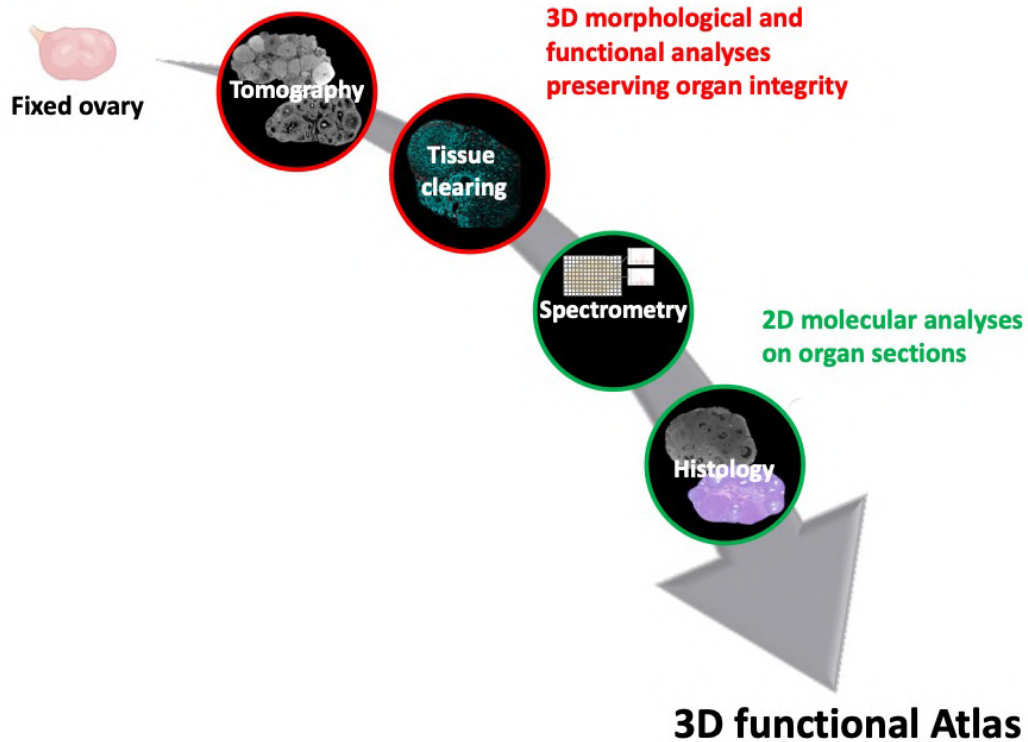


**Figure 8. Overall pipeline design.** A PFA-fixed ovary first undergoes tomography and tissue clearing, two non-disruptive techniques which analyse the entire organ, providing 3D morpho-functional information; then, the same ovary is sectioned to investigate more in-depth molecular details with spectrometry and histological approaches. The combination of the data obtained will be combined into a 3D functional Atlas of the mouse ovary.

More in details, the pipeline structure follows these sequential approaches:

- ***Fixation:*** The first and crucial step of the novel pipeline involves ovary isolation and fixation in paraformaldehyde (PFA), which preserves the organ with its specific tissue organisation, cells composition and sub-cellular proteins and macromolecules signatures [80], so that the organ can be used for subsequent serial analyses.
- ***Tomography:*** After being fixed, the ovary is stained with Lugol's solution for imaging with micro- or nano-Computed Tomography. microCT is a tomographic method which produces a true 3D reconstruction of an object, with cubic voxels and an isotropic resolution in the range of 20 to 1  $\mu\text{m}/\text{pixel}$  [81]. It has been extensively used with hard tissues, such as bones [82], [83] and teeth [84], [85], [86], whose histological composition makes them naturally radiopaque to X-rays. However, its application in soft tissues imaging is often restricted by the need of contrast agents, whose unstable interaction with tissue components results in a partial capacity to highlight the presence of different structures within the organs [87], [88], [89], [90].

Nano-Computed Tomography (nanoCT), instead, is an ultra-high-resolution imaging technique that goes beyond the resolution capacity of a microCT system [91], reaching 1000-100 nm/pixel. As microCT, nanoCT is widely used for a variety of three-dimensional studies, from material [92] to life science application [93], [94], [95].

The morphological data obtained with both tomographies are processed and displayed in 2D with Dataviewer or ImageJ and modelled in 3D with CTVox or Avizo.

- Tissue clearing: Subsequently, the same ovary is destained, treated with the iDISCO tissue clearing method [96] and labelled with specific antibodies or fluorescence stains to localise molecular markers. Specifically, the iDISCO protocol has been developed for the analysis of the brain and is a solvent-based approach, which exploits a long incubation in dimethyl sulfoxide, methanol and dichloromethane to make lipid-rich adult organs permeable to multiple molecular markers, and optically transparent by removing lipids, the main responsible components for refractive index inhomogeneity. When combined with fast optical imaging systems, such as confocal or light sheet microscopy, this approach allows to interrogate the whole organ volume and to characterise its internal structures with qualitative information. The obtained optical sections are processed and displayed in 2D or 3D with ImageJ (NIH).

- Mass Spectrometry: This step requires the whole organ sectioned into serial sections for the *in-situ* analysis of the peptide content of the follicular types with Matrix-Assisted Laser Desorption/Ionization mass-spectrometry imaging (MALDI-MSI). MALDI-MSI, also referred to as molecular histology, is a recent and emerging omics, which allows the *in-situ*, simultaneous, label-free detection of thousands of analytes maintaining their tissue localisation on histological sections [97], [98]. MALDI-MSI has been recently used in a number of biomedicine applications, among which the study of differentiation processes [99], or for the discovery of candidate biomarkers in tumoral and non-tumoral diseases [100]. The mass spectra of individual follicle types are pre-processed, segmented and statistically analysed with SCiLS Lab MVS 2019c Pro software (Bruker) to highlight differences in the peptide content during follicle growth and oocyte maturation.

- Histology: Then, the same sections are stained to be studied with histological approaches, such as confocal or classical histology. Confocal Histology is a new type of technique developed in our laboratory, that combines the fluorescent property of Eosin with confocal 3D optical imaging to identify developmentally competent (SN) or incompetent (NSN) oocytes. The use of 3D optical imaging allows to acquire information even below the specimen surface, even within thicker sections, without losing precious subcellular details. As an alternative to Eosin, it is possible to stain sections with a large panel of classical histological dyes, widely used in biomedicine [101], [102]. This approach allows to acquire, with light microscopy, images at very high-resolution, depending on the magnification lenses used, to identify different aspects of the

## A novel pipeline for the *in-silico* 3D functional reconstruction of the mouse ovary

---

ovarian cell biology, and to highlight the smallest capillaries around individual growing follicles. Data generated with these two histological approaches add morphological and key functional aspects (i.e., the developmentally competence of oocytes) to the 3D model.

In the following Chapters, I will describe the process of optimisation of each of the six techniques on individual ovaries, and I will show and discuss the results obtained so far, with the aim of applying all analyses to the single ovary and to create a 3D Atlas.

---

# Chapter 3

---

## Tomography

### 3.1. Micro-Computed Tomography

Here, I describe the optimised contrast protocol and the microCT imaging procedure that allowed the 3D mapping and counting of the stages of follicle growth from the secondary T4 to completion of folliculogenesis, and the identification of the major vasculature inside the adult mouse ovary [103].

#### 3.1.1. PFA fixation and Lugol's solution staining represents an optimal preparation protocol for the ovarian microCT imaging

The preparation of the adult mouse ovary for microCT analysis was performed by combining and testing three different fixative types [Carnoy, Bouin's solution or 4% Paraformaldehyde (PFA)] and four contrast agents (Iodine tincture, Phosphotungstic acid, Uranyl acetate or Lugol's solution). Then, microCT scanning at 5  $\mu\text{m}/\text{pixel}$  was used to compare the different preparation protocols.

Of the three fixatives, Carnoy caused a shrinkage of the ovary, which persisted even during the microCT scanning period and led to the acquisition of fuzzy images (data not shown). The Bouin's solution, while preserving a good histological organisation, increased tissue hardness and reduced its accessibility to the contrast solution, resulting in an uneven contrast agent penetration and patchy images (data not shown). On the contrary, 4% PFA, a water-based fixative, turned out to be the best compromise as it maintained a good histology and it enabled an optimal contrast agent diffusion inside the organ volume.

Once chosen the PFA as optimal fixative, treatment with the contrast agent was performed for different incubation periods, ranging from 15 min to 8 hr, followed by a washing period ranging from 30 sec to 15 hr. Iodine tincture (Figure 9A), an alcohol-based solution, favoured the organ shrinkage, Phosphotungstic acid (Figure 9B) showed a reduced capacity to penetrate in depth through the ovarian multistratified and complex epithelium, and, although Uranyl acetate (Figure 9C) resulted in a good and homogeneous contrast, it was discarded due to the uranium toxicity and difficulty in its routine handling and disposal.

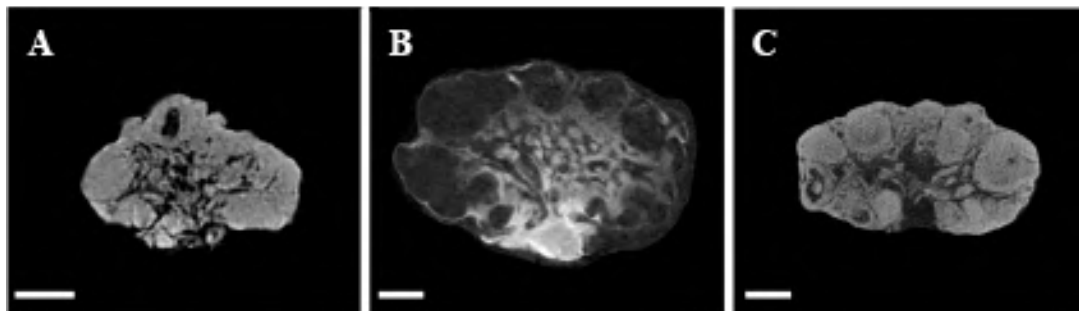


**Figure 9.** Representative 5  $\mu\text{m}/\text{pixel}$  microCT images of PFA-fixed mouse ovaries treated with different contrast agents. **A)** Iodine tincture. **B)** Phosphotungstic acid. **C)** Uranyl acetate. Bar, 500  $\mu\text{m}$ .

Compared to either Iodine tincture, Phosphotungstic acid or Uranyl acetate, the staining with water-based Lugol's solution for 3 hr, followed by a washing period of 15 hr, produced the best results (Figure 10A). Contrast was homogeneous throughout the whole organ volume, highlighting distinctly marked follicles. Figure 10B shows the corresponding histological cross-section, in which follicles from the small T4 secondary (red arrowhead) to the largest antral T8 follicles and *corpora lutea* are visible.

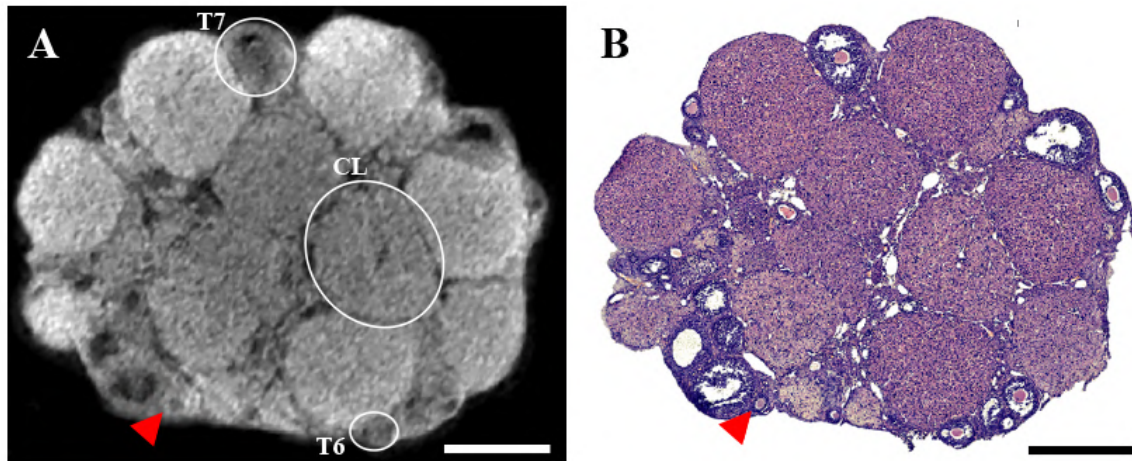


**Figure 10.** **A)** A representative 5  $\mu\text{m}/\text{pixel}$  microCT image of the mouse ovary after PFA fixation and contrast with Lugol's solution, clearly showing various *corpora lutea* (CLs), T7, T6 and T4 follicles (red arrowhead). **B)** Hematoxylin and Eosin stained cross-section corresponding to the microCT image shown in (A). Bar, 500  $\mu\text{m}$ .

### 3.1.2. 1.5 $\mu\text{m}/\text{pixel}$ microCT of the adult mouse ovary shows follicles from the secondary T4 to the fully-grown T8 and *corpora lutea*, with subcellular details

Using the optimised protocol described above, we extended the microCT analysis to a new group of three ovaries, isolated from three adult females, using a 1.5  $\mu\text{m}/\text{pixel}$  resolution. This resolution allowed the identification of all the phases of follicle growth, with the exception of primordial and primary follicles. Figure 11A shows the eight main stages of mouse folliculogenesis [20], [104], from the resting pool of tiny primordial T1 and T2 follicles, followed by the primary T3 and secondary T4 follicles, until reaching the fully-grown antral T8 stage.

Figure 11B shows a representative microCT image of an ovary in which we could pinpoint equatorially sectioned follicles ranging from the small secondary T4, with 60  $\mu\text{m}$  size in diameter, through all the growing stages until the largest T8 and CLs, with 320 and 480  $\mu\text{m}$  size in diameter, respectively. In antral follicles, the Lugol's radiopacity brought up differences in density among the follicle's internal components. Specifically, the enlargement of Figure 11B displays the microCT identification of the layers of granulosa cells, antrum, cumulus cells, zona pellucida, and of the oocyte with its nucleus inside a T8 follicle.

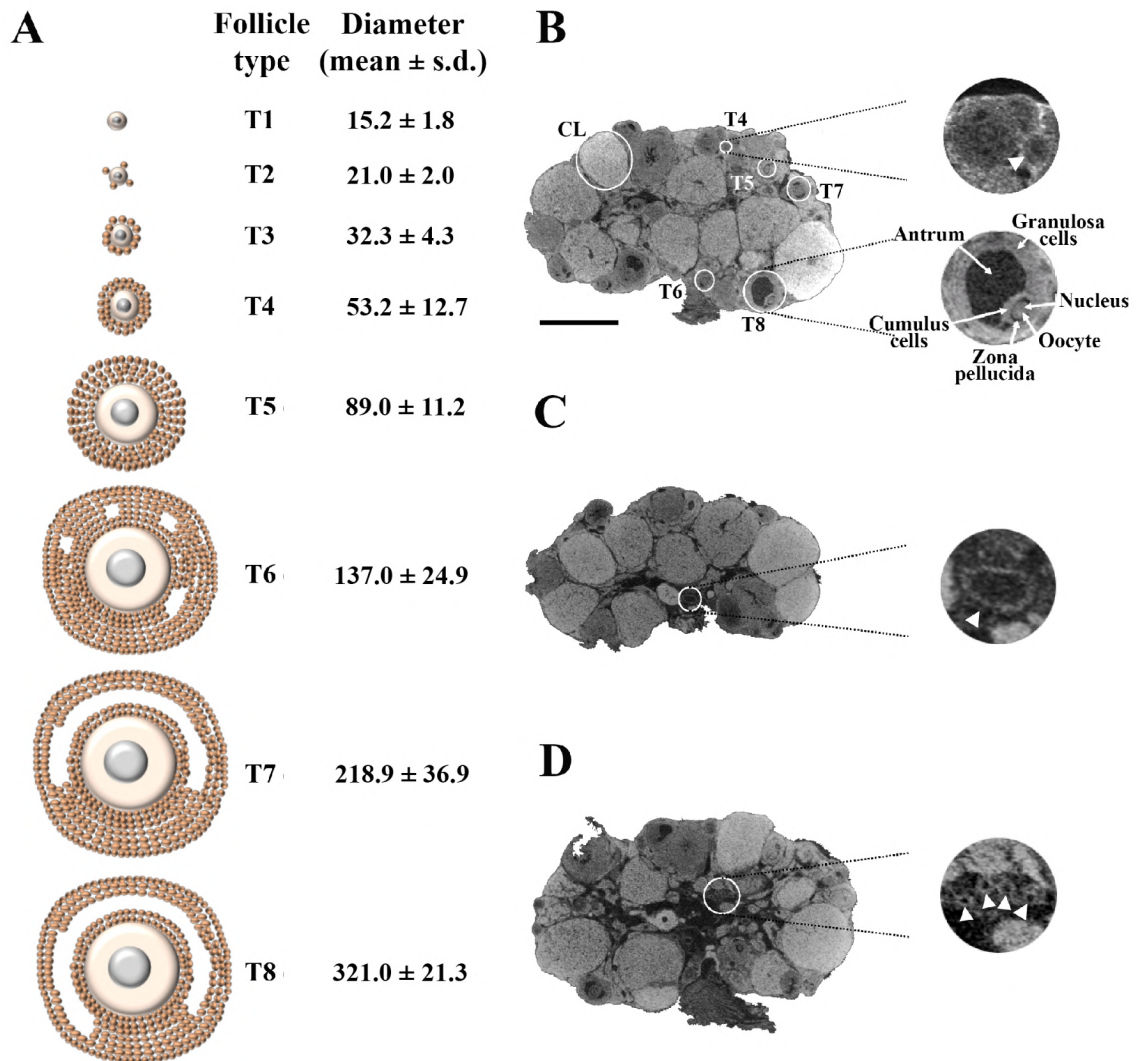


**Figure 11.** **A)** Schematic representation of the eight main stages of the mouse folliculogenesis, with their corresponding size in diameter (mean  $\pm$  s.d.), during the preantral (T1-T4) and antral (T5-T8) growth phases. **B)** A representative microCT section highlighting follicles from T4 to T8 and CL. On the right-hand side (top), an enlargement of a secondary T4 follicle (arrow); and an enlargement of a fully-grown T8 follicle (bottom), in which the different cytological components (i.e., granulosa cells, antrum, cumulus cells, zona pellucida and oocyte with its nucleus) are clearly visible. **C)** microCT section with an enlargement of a vessel (arrowhead; 150  $\mu$ m in diameter) at the ovarian hilum site. **D)** microCT section with an enlargement of a group of small vessels (arrowheads; 35  $\mu$ m in diameter) in the medulla region. Bar, 500  $\mu$ m.

MicroCT allowed also the identification of the main ovarian vasculature branches, ranging from the largest vessels at the ovarian hilum site (150  $\mu$ m size in diameter; Figure 11C), to smaller vessels present in the medulla region (35  $\mu$ m size in diameter; Figure 11D).

### 3.1.3. Combined 3D rendering of microCT sections of the ovary and of the main vasculature

These digital microCT images were further analysed, segmented and reconstructed with a volume rendering software in a 3D model of the ovary which combined both follicular and vascular components (Figure 12), showing how the latter reach and supply the different organ regions.

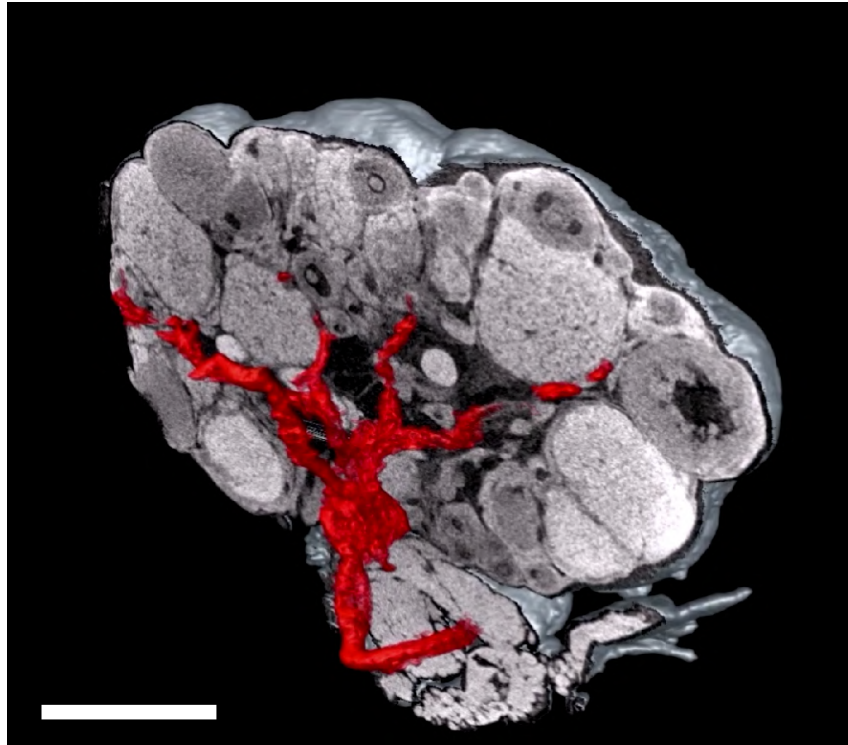


**Figure 12.** Combined 3D reconstruction of the main vasculature with the ovarian follicular component. Bar, 500  $\mu\text{m}$ .

### 3.1.4. 3D mapping of growing T4 to T8 follicles and *corpora lutea* to describe the trajectory of follicles recruitment and growth

Alongside with the opportunity to draw, on each single 1.5  $\mu\text{m}/\text{pixel}$  section, a detailed territorial map of the follicles identified with different colours depending on the belonging class (Figure 13A), this microCT analysis permitted also follicles classification, their volume rendering with 3D spatial localisation (Figure 13B), and their precise counting (Figure 13C and Table 1).

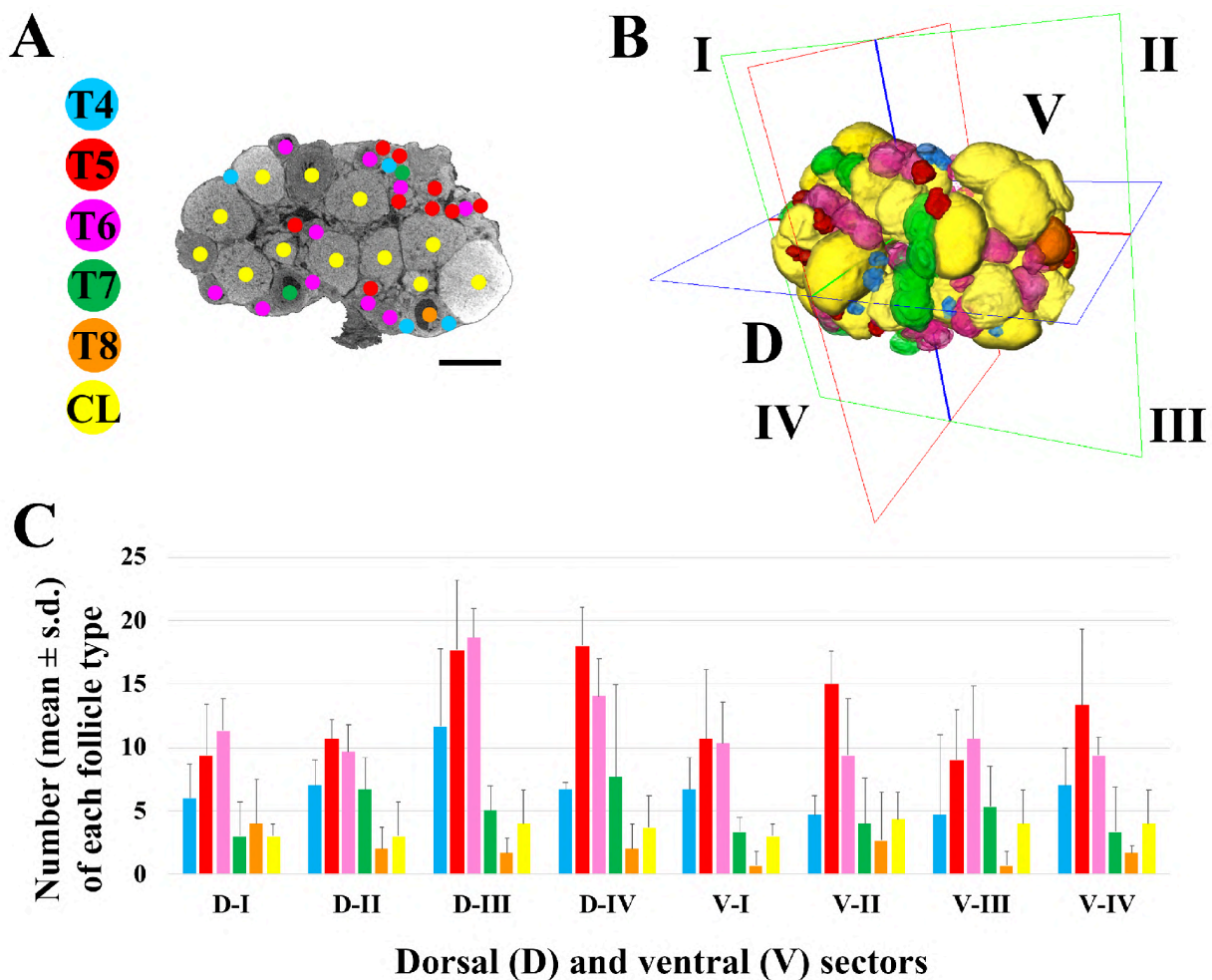


**Figure 13.** **A)** Representative microCT image of T4-CL mapping procedure performed through all ovary sections ( $1070.3 \pm 93.6$ ). Bar, 500  $\mu\text{m}$ . **B)** Volume rendering of T4-T8 follicles and CLs present in the ovary, and virtual segmentation of the organ's dorsal and ventral into eight equal sectors. **C)** Histogram describing the distribution of each follicle type and CL into the eight dorsal or ventral sectors of three ovaries from three different female mice.

Table 1 shows the total number of T4-CL follicles counted in the ovary ( $334.0 \pm 48.8$ ), in which T5 and T6 are the most abundant ( $103.7 \pm 20.1$  and  $93.3 \pm 14.2$ , respectively).

To precisely locate the follicular structures within each ovary, the spatial reference system used was the anatomical orientation of the organ in relation to the anterior-posterior and dorsal-ventral body axes. When the microCT ovarian sections were virtually divided into two equivalent halves along the anterior-posterior axis, we counted the same total number of follicles in the anterior ( $162 \pm 34.4$ ) and posterior ( $172 \pm 14.4$ ) regions ( $p > 0.05$ ), and an even distribution ( $p > 0.05$ ) of each follicle type (data not shown). Similarly, when the ovary was halved along the dorsal-ventral axis, the number of both total and of each specific follicle type was equally allocated between the two regions ( $186.3 \pm 32.5$  and  $147.7 \pm 18.6$ , respectively), although dorsally a slight, but not significant ( $p > 0.05$ ), higher total number was found.

**Table 1.** Follicle type number (mean  $\pm$  s.d.) counted in each of the four dorsal (D-I to D-IV) and ventral (V-I to V-IV) sectors in which the three ovaries studied were sectioned. Statistical analysis with Student’s t-test of the number of follicles present in the dorsal or ventral regions did not show significant differences ( $p > 0.05$ ). Statistical analysis with one-way ANOVA followed by the Bonferroni’s post-hoc test performed comparing the number of each follicle type among the eight sectors (horizontal comparison) did not highlight significant differences ( $p > 0.05$ ). Instead, the same analysis, when done comparing follicle types within the same ovarian sector (vertical comparison), brought up the following significant differences ( $p < 0.05$ ): D-I, no significant differences; D-II, T5 vs T8, T5 vs CL, T6 vs T8, T6 vs CL; D-III, T5 vs T8, T5 vs CL, T6 vs T8, T6 vs CL; D-IV, T4 vs T5, T5 vs T8, T5 vs CL, T6 vs T8; V-I, T5 vs T8, T6 vs T8; V-II, T4 vs T5, T5 vs T7, T5 vs T8, T5 vs CL; V-III, no significant differences; V-IV, T5 vs T7, T5 vs T8. Also, the comparison of the total number of each follicle type present in the ovary showed significant differences between T5 vs T7 and T5 vs T8.

Follicle type	Total number follicles	Dorsal				Ventral			
		$186.3 \pm 32.5$ / $147.7 \pm 18.6$							
		D-I	D-II	D-III	D-IV	V-I	V-II	V-III	V-IV
<b>Total</b>	$334.0 \pm 48.8$	$36.7 \pm 12.1$	$39.0 \pm 5.3$	$58.7 \pm 4.2$	$52.0 \pm 12.3$	$34.7 \pm 10.0$	$40.0 \pm 11.5$	$34.3 \pm 14.6$	$38.7 \pm 14.6$
<b>T4</b>	$54.3 \pm 12.2$	$6.0 \pm 2.6$	$7.0 \pm 2.0$	$11.7 \pm 6.1$	$6.7 \pm 0.6$	$6.7 \pm 2.5$	$4.7 \pm 1.5$	$4.7 \pm 6.3$	$7.0 \pm 3.0$
<b>T5</b>	$103.7 \pm 20.1$	$9.3 \pm 4.0$	$10.7 \pm 1.5$	$17.7 \pm 5.5$	$18.0 \pm 3.0$	$10.7 \pm 5.5$	$15.0 \pm 2.6$	$9.0 \pm 4.0$	$13.3 \pm 6.0$
<b>T6</b>	$93.3 \pm 14.2$	$11.3 \pm 2.5$	$9.7 \pm 2.1$	$18.7 \pm 2.3$	$14.0 \pm 3.0$	$10.3 \pm 3.2$	$9.3 \pm 4.5$	$10.7 \pm 4.2$	$9.3 \pm 1.5$
<b>T7</b>	$38.3 \pm 23.4$	$3.0 \pm 2.6$	$6.7 \pm 2.5$	$5.0 \pm 2.0$	$7.7 \pm 7.2$	$3.3 \pm 1.1$	$4.0 \pm 3.6$	$5.3 \pm 6.2$	$9.3 \pm 3.5$
<b>T8</b>	$15.3 \pm 8.5$	$4.0 \pm 3.5$	$2.0 \pm 1.7$	$1.7 \pm 1.1$	$2.0 \pm 2.0$	$0.7 \pm 1.1$	$2.7 \pm 3.8$	$0.7 \pm 1.1$	$1.7 \pm 0.6$
<b>CL</b>	$29.0 \pm 4.4$	$3.0 \pm 1.0$	$3.0 \pm 2.6$	$4.0 \pm 2.6$	$3.7 \pm 2.5$	$3.0 \pm 1.0$	$4.3 \pm 2.1$	$4.0 \pm 2.6$	$4.0 \pm 2.6$

Then, we proceeded by segmenting both the dorsal (D-I to D-IV) and ventral (V-I to V-IV) region into four, equally partitioned, sectors. Sectors contained an equal total number of follicles ( $41.7 \pm 12.6$ ;  $p > 0.05$ ) and an identical number of each follicle type, with the exception of T5 and T6, which resulted the most numerous in all sectors ( $p < 0.05$ ), and of fully-grown T8, the smallest group (Figure 13C and Table 1).

### 3.2. Nano-Computed Tomography

NanoCT analysis was carried out in collaboration with dr. A. Parrilli, (Center of X-ray Analytics Empa Zurigo, Switzerland), and allowed us to extend the tomographic analysis to smaller mouse ovaries, aged between 4 and 25 days after birth (days post natal, dpn), without reducing the final images quality. In this time window, the organ houses the early subsequent cycles of follicular recruitment and growth, however it has not yet undergone the first ovulation. In particular, the 25 dpn ovary contains numerous follicles at all the stage of growth - from T1 to T8 - derived from about 7 subsequent recruitment waves, but, in the absence of the first ovulation, it does not contain CLs (Figure 14).

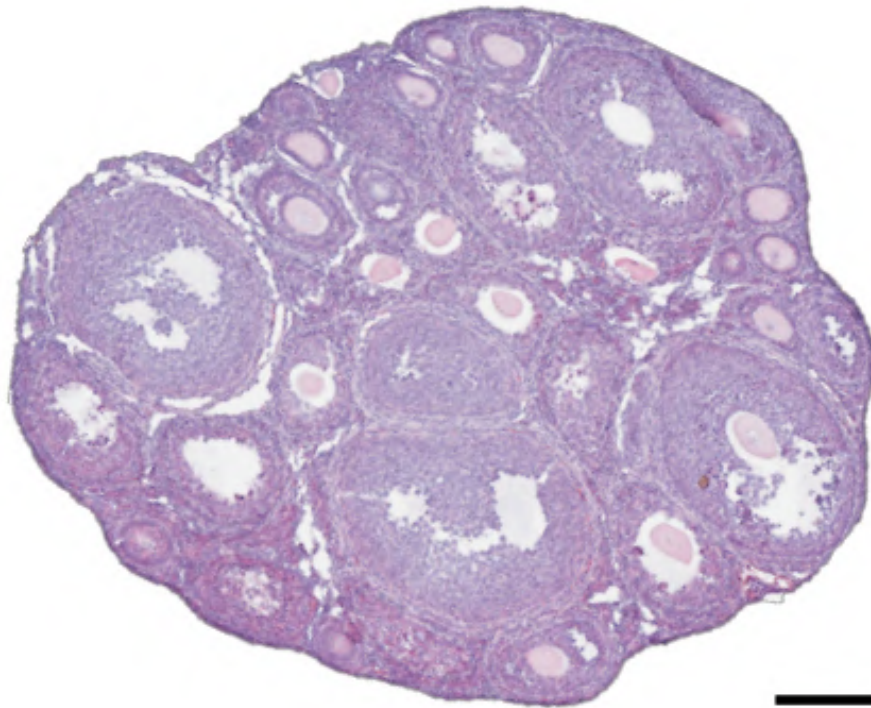


**Figure 14.** Representative histological section of a 25 dpn ovary stained with Hematoxylin and Eosin. Bar, 200  $\mu$ m.

The main objective of this analysis is to take advantage of the absence of CLs and of the smaller organ size to obtain a faster and more accurate count and localisation of the follicle types within the ovarian volume, and to reconstruct the dynamics of folliculogenesis during the first decisive stages of organ development and preparation to puberty.

### 3.2.1. NanoCT of the young mouse ovary shows follicles from the primary T3 to the fully-grown T8, with subcellular details

Ovaries of 4 to 25 dpn females were prepared with the protocol previously developed for microCT. However, after fixation in PFA, it was necessary to adapt the contrast time with Lugol's solution according to the decreasing size of each ovary, from 3 hours used for the adult (also valid for ovaries from 25 to 16 dpn), to very short periods as described in Material and Methods (Table 9).

Ovaries were then analysed with the nanoCT EasyTom XL system (RX Solutions) using a scanning resolution between 1 and 0.650  $\mu\text{m}/\text{pixel}$ . Figure 15 shows a panel with a representative section for each of the samples acquired during the ovarian development until 25 dpn. Despite the nominal resolution used, the contrast agent showed a gradually reduced ability to interact differentially with tissue components and bring out the structures inside the ovaries from 4 to 13 dpn. This finding is likely due to the smaller and less mature follicular structures contained and, as a consequence, to their homogeneity in terms of density.

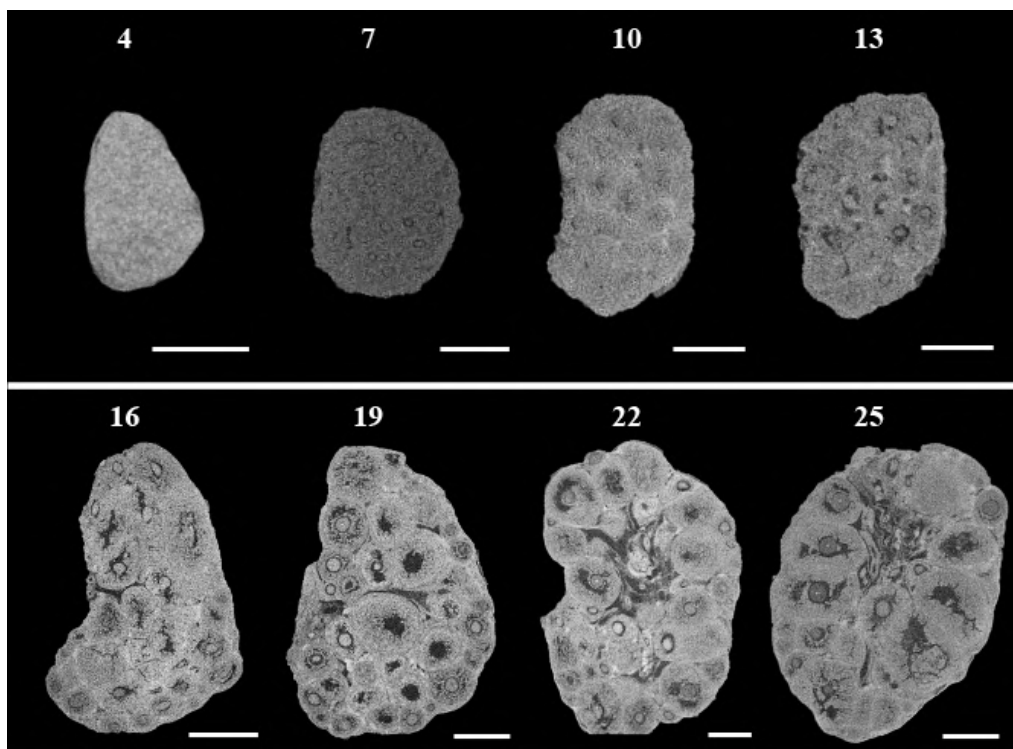


**Figure 15.** Panel showing representative nanoCT sections of all ages analysed between 4- and 25-days post natal (dpn). Bar, 200  $\mu\text{m}$ .

For the 25 dpn ovary, the analysis of nanoCT sections allowed the identification of the main blood vasculature and of follicles from T3 to T8

(Figure 16), extending the tomographic spatial 3D reconstruction of folliculogenesis to the primary follicle.

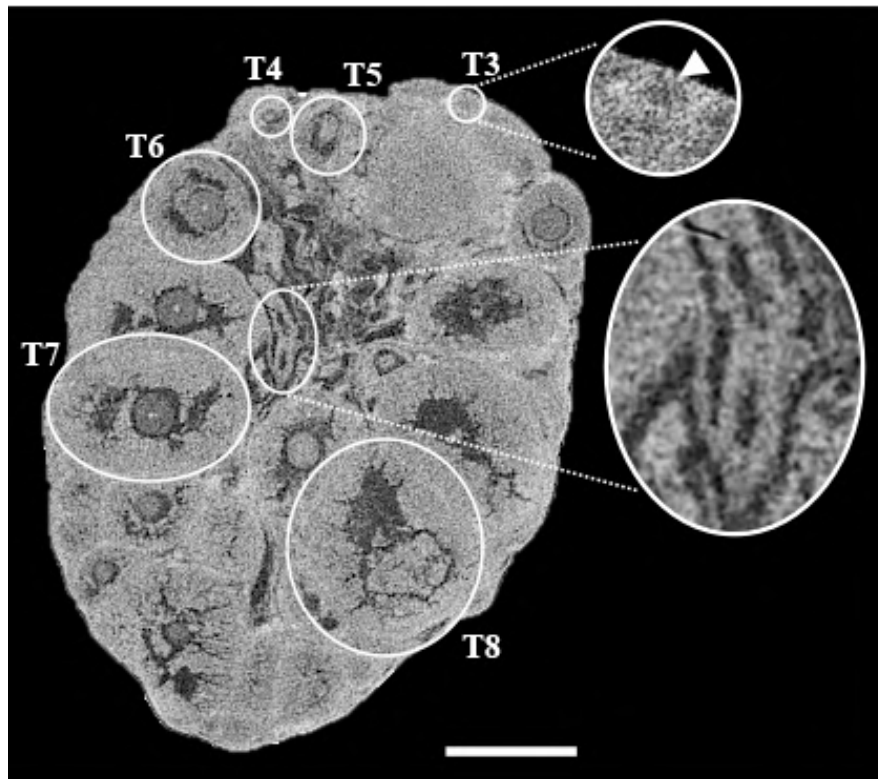


**Figure 16.** Representative nanoCT section of a 25 dpn mouse ovary. On the right-hand side (top), an enlargement of a primary T3 follicle (white arrowhead); on the right-hand side (bottom), an enlargement of two large blood vessels. Bar, 200  $\mu\text{m}$ .

After dataset pre-processing, follicles were individually segmented with a combination of ImageJ functions and plug-ins (i.e., ROIs manager, thresholding, binarization and logic operations). Finally, the segmented sections were processed with the volume and surface rendering algorithms implemented by Avizo software, obtaining the 3D models (Figure 17). Figure 17F shows the result of the gradual combination in a coherent reference space of the models related to the individual follicular types, from T3 to T8.

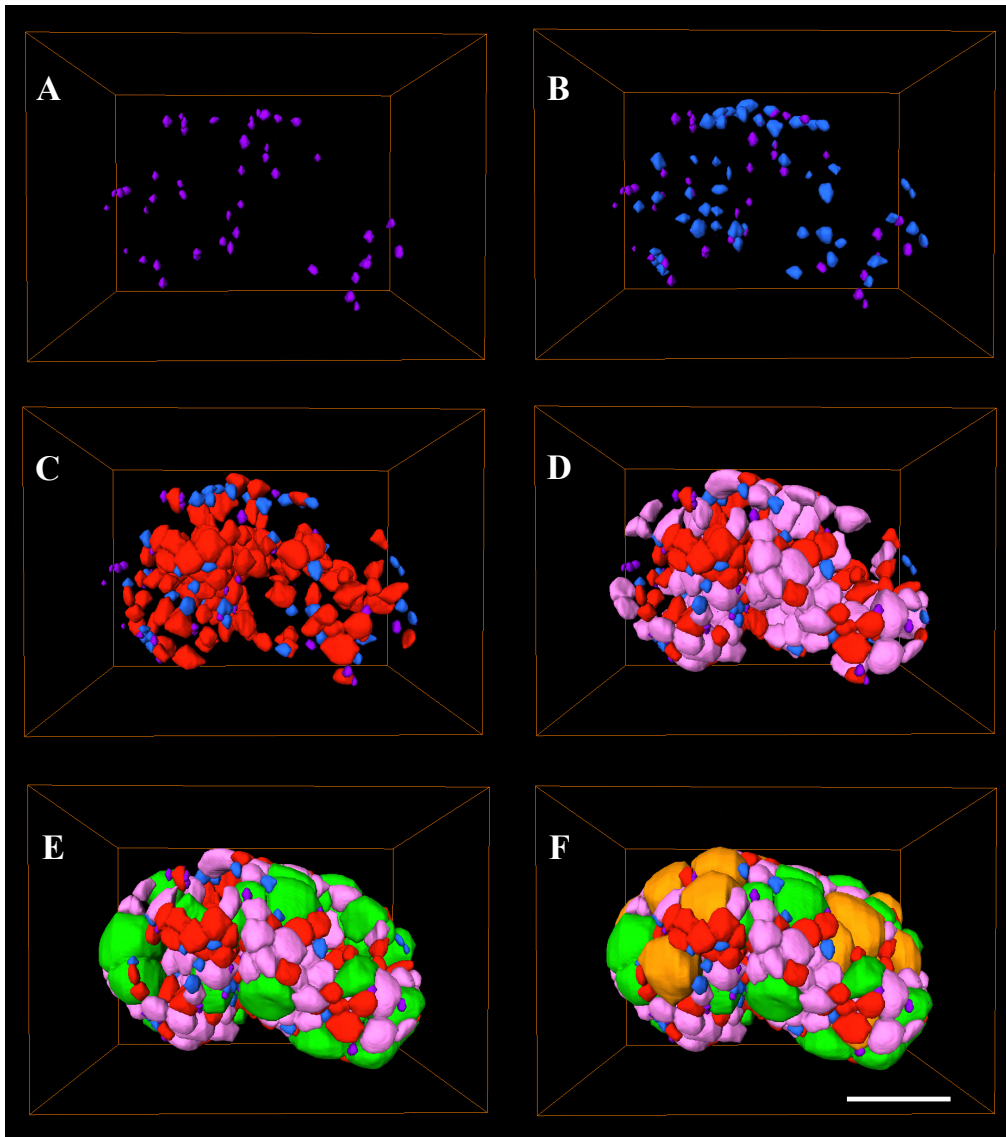


**Figure 17.** 3D reconstruction of the 25 dpn mouse ovary one step at a time, in which the colours represent follicles belonging to different classes. **A)** Shows the 3D localisation of T3 follicles; in **B-C-D-E)** there is the addition of one follicle type at a time, from T4 (**B**); through T5 (**C**) and T6 (**D**), to T7 (**E**); **F)** Shows the complete 3D model including follicles from primary T3 to fully grown pre-ovulatory T8. T3, purple; T4, blue; T5, pink; T6, red; T7, green; T8, orange. Bar, 500  $\mu\text{m}$ .

Currently, we are proceeding to count and locate all the follicles as described above for the microCT (Chapter 3.1.4).

### **3.2.2. NanoCT analysis at 0.25 $\mu\text{m}/\text{pixel}$ allows the completion of the tomographic reconstruction of folliculogenesis within the mouse ovary**

Subsequently, the acquisition of the ovaries from 4 to 25 days was further optimised by combining the embedding of each ovary into a tiny cube of paraffin wax with the replacement of the flat panel with a Charge-Coupled Device (CCD) camera. Particularly, the first modification allowed to place on the rotating sample holder a much smaller and more stable specimen, leading to the prevention of micro-vibrations during scanning and a closer location of the sample in relation to the X-ray source. In addition, the use of a CCD camera allowed the increase of the resolution, from the maximum of 0.65  $\mu\text{m}/\text{pixel}$ , reached with the flat panel, to a 0.25  $\mu\text{m}/\text{pixel}$  with the CCD.

Figure 18B shows the improved resolution in a representative 16 dpn ovary section compared to the flat panel detector results (Figure 18A). Beyond this difference in the nominal resolution used, images acquired with the CCD camera showed a better discrimination of smaller structures, with a single-cell accuracy, never obtained before. Subcellular structures were also visible, besides those describe above (Chapter 3.1.2.): the oocyte nucleus within the T4 follicle (Figure 18B, enlargement), the single layers and type of follicular cells surrounding the gamete, altogether important classification elements. Also, this improvement allowed to extend the identification of follicle types, including the primordial T1 and T2, with a diameter of about 15 and 19  $\mu\text{m}$  in size, respectively (Figure 18B, enlargements).

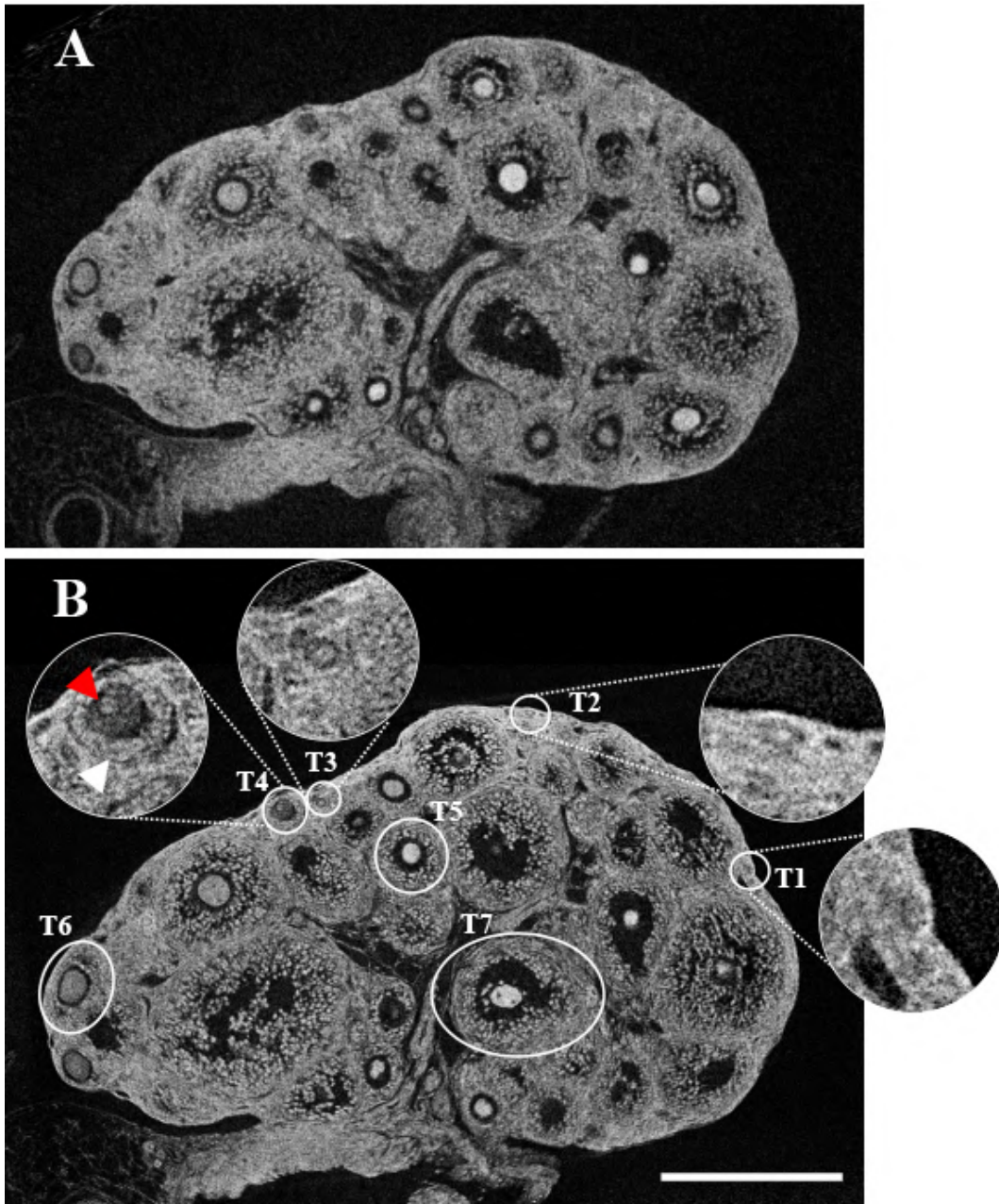


**Figure 18.** Comparison between representative nanoCT sections of the same 16 dpn paraffin-embedded ovary. **A)** nanoCT section acquired with flat panel at final resolution of  $0.65\ \mu\text{m}/\text{pixel}$ ; **B)** nanoCT section acquired with CCD camera at final resolution of  $0.25\ \mu\text{m}/\text{pixel}$ , in which follicles from T1 to T8 are visible. Within the T4 enlargement, the red arrowhead indicates the oocyte's nucleus and the white arrowhead the two layers of follicle cells surrounding the oocyte. Bar,  $200\ \mu\text{m}$ .

Overall, the analysis described in Chapters 3.1 and 3.2 constitute the first tomographic analyses of the mouse ovary during different periods of its development.

The microCT procedure allows the observation of the internal structure of the adult mouse ovary with its main ovarian artery branches, and the mapping of the 3D position of follicles from T4 through T8 and CLs, with unprecedented precision. This procedure is robust and has the advantage of being faster than other classical methods like histology or tissue clearing [64], [65], [105], [68], [69], [106]. Also, follicle counts on microCT datasets are more accurate than those obtained starting from histological serial sections, which rely on stereological approaches or correction factors in order to convert the count of sectioned follicles into a single and reliable number [107], [108], [109].

In the literature there is a single work [77] carried out *ex vivo* to verify the efficacy of microCT for the characterisation of the ovarian structures of seven mammalian species. However, this study does not include the mouse ovary, and in the rat ovary, the smallest among the analysed species and with a volume about three times greater than the murine, they were able to visualise only the antral T6 to T8 follicles.

The reason why we could not identify follicles smaller than T4 may depend on the reduced size of its enclosed oocyte ( $< 20 \mu\text{m}$  in diameter) - much similar to that of the companion follicle cells - and on the absence around the germ cell of a zona pellucida, which begins to be fully present in T4 follicles, and that, with its glycoprotein layer, may create the right conditions for the contrast agent to be deposited.

Besides the observation of growing follicles, the tomographic procedure identified allowed, for the first time, the identification of the main functional cellular and subcellular compartments that constitute the growing follicle. Thus, the granulosa, antrum, cumulus cells, zona pellucida, and oocyte together with its nucleus, were clearly brought up not only in the largest T8 follicles, but also, when present, in smaller follicle types. The observation of a subcellular component such as the nucleus might be explained with an on-site specific contrast created by a differential local density of a tightly dense nucleolus surrounded by centromeric heterochromatin [110].

The *in-silico* reconstruction of the ovary with isotropic resolution allowed an accurate counting of each T4 to T8 follicles and CLs comprised dorsally and ventrally. Our results highlight a homogeneous distribution of all the different follicle types not only between the dorsal and ventral region, but also among the eight sectors in which they were divided. Specifically, each sector houses an equal number of follicles, including CLs and, also, each follicle type is equally represented, with T5/T6 and fully-grown T8 being the most and least abundant, respectively. Taken as a whole, these data suggest that every cycle of follicle recruitment occurs simultaneously in all the eight sectors, is homogeneously distributed all-over the cortex, and that follicles initiate and terminate their growth within the same ovarian sector (Figure 19).

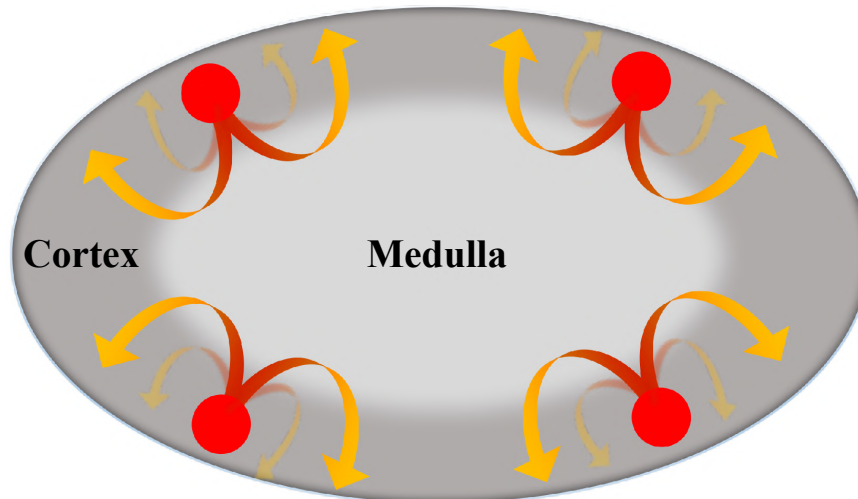


**Figure 19. Graphical model describing the trajectory of follicles recruitment and growth.** Follicle recruitment (red circle) occurs simultaneously in the cortex of all the eight sectors in which the ovary was virtually segmented. Then, follicles initiate growth towards the medulla (red segment of the arrow), increasing their size until they re-emerge into the cortical region (yellow segment of the arrow) from where, as fully-grown antral follicles, they could undergo ovulation.

Then, local biomechanical signals might regulate the follicles growth and migration towards the softer medulla environment [29] until they re-emerge, as T8 follicles, and expose the follicular apex to the cortex surface from where they could be ovulated, leaving the CLs behind.

This is consistent with studies suggesting that the early stages of folliculogenesis, i.e., primordial follicle activation from the ovarian resting pool, depend on biomechanical signalling induced and regulated mainly by the local stiffness of the cortical region in which primordial follicles are housed, which, due to an unchanging composition of extracellular matrix and stroma components, is homogeneous all over the ovary [111]. Only the subsequent phases of growth, from the early antral follicle onwards, are modulated by the synergic and spatially targeted action of hormonal, paracrine and autocrine signalling [31].

The nanoCT analysis presented is the first of its kind and allows an extremely accurate characterisation and 3D localisation of follicles belonging to all the stages of folliculogenesis, from the tiny primordial T1 to the pre-ovulatory T8, within the young mouse ovary.

As evolution of the previous study performed using microCT on the adult mouse ovary, we started by maintaining the same sample preparation procedure with PFA fixation, Lugol's solution treatment and scanning with each ovary fixed at the bottom of a small Eppendorf tube filled with water; however, during acquisition, we used the flat panel, a more efficient detector in terms of scanning time [112]. These analyses allowed to clearly distinguish follicles from the

primary T3 to the subsequent growing stages within ovaries from 16 to 22 dpn, and until the pre-ovulatory T8 in the 25 dpn pre-pubertal ovary. The possibility to discriminate and recognise internal structures in smaller ovaries from 13 to 4 dpn is reduced, perhaps because they only house follicles at the first stages of growth, from primordial T1-T2 to at least T5 follicles. These stages of folliculogenesis are all characterised by the absence of an antrum, and only from T4 and T5 the zona pellucida begins to be deposited around the oocyte [113]. As previously observed with microCT analysis, antrum and zona pellucida are crucial histological components for CT imaging as they show a density distinctly lower than that of the adjacent structures. The absence of these two components, which interact mildly with the contrast agent, and, therefore, have a very low radiopacity, makes the tissue more homogeneous, and reduces the establishment of the intensity difference used for follicle identification or classification.

When watched in the 3D reconstructed model (Figure 17), follicles appear to be homogeneously distributed, with T3 and T4 at the beginning of their growth, located in a more peripheral position, within the cortex region of the organ. Then, during growth, follicles increase their volume and encroach on the more internal and biomechanically permissive medulla. Finally, T8 follicles expose the follicular apex to the ovarian surface in preparation to ovulation [114].

Then, we presented an improved preparation protocol that combines the paraffin-embedding of each ovary before scanning with the use of a highly sensitive CCD detector. Although the flat panel represents the best compromise between accuracy and scanning time (for the analysis of the paraffin-embedded 16 dpn ovary showed in Figure 18, the flat-panel took 2 hr vs 8 hr of the CCD detector), the use of the higher sensitive CCD camera allows to complete the first tomographic reconstruction of the early folliculogenetic cycles within the mouse ovary, with a precise identification of all follicle types, from primordial T1 to fully-grown T8.

Worth of mentioning is, also, the possibility to clearly observe single cells and subcellular components within the ovarian tissue organisation (Figure 18B, T4 follicle enlargement). Despite the loss of information within the section thickness, histology still represents the gold standard to study the tissues cellular organisation, with a resolution limit attesting at 0.2 - 0.23  $\mu\text{m}/\text{pixel}$  [115]. Our results brought up the possibility to use nanoCT at 0.25  $\mu\text{m}/\text{pixel}$  as a fast, non-destructive, accurate 3D analysis complement to histological examination of tissues, in normal or pathological conditions.

In conclusion, the results obtained with the optimised preparation protocol and the nanoCT imaging procedure proposed, laid down the bases for the spatial analysis of the early recruitments within the prepubertal mouse ovary, and for the 3D localisation of follicles involved in the first ovulation with the aim to define ovarian functional regions.

Taken together, the application of micro- and nanoCT analyses provides the first 3D isotropic reconstruction of the mouse ovary, well maintaining its integrity and facilitating its further analysis with the other approaches described in our pipeline. As an example, the use of PFA fixative preserves protein

components, thus allowing additional investigations into more specific molecular functional markers, that will be central for the building of a 3D functional Atlas.

---

# Chapter 4

---

## Tissue clearing combined with 3D optical imaging

In this Chapter, I will describe the results obtained by combining iDISCO+ [96], a tissue clearing method, with 3D optical confocal imaging to clear, immune-stain and analyse the whole adult mouse ovary, identifying all follicle types and the ovarian vasculature down to the thinnest capillaries surrounding individual follicles. Alongside with the morphological analysis, this approach opens the possibility to reveal functional information on specific ovarian structures.

### **4.1. The iDISCO+ clearing protocol combined with confocal microscopy allows the identification of all the different follicle types, from T1 to T8, in association with the surrounding capillaries meshwork**

Although several tissue clearing techniques have been developed [6], [7], all of them are based on the reduction of light scattering through the massive removal of molecules that confer tissue opacity, and the matching of sample refractive index with that of the surrounding solutions, which reduces laser beam perturbation during the imaging across the entire organ volume [6], [116].

Figure 20 shows the best iDISCO+ clearing result of the whole ovary obtained following protocol optimisation by varying the incubation time. The use of alcoholic solutions such as methanol for pre-treatment, and Dichloromethane combined with Dibenzyl ether (DBE) during the clearing phases, led to a dehydration of the organ and to a mild isotropic shrinkage.

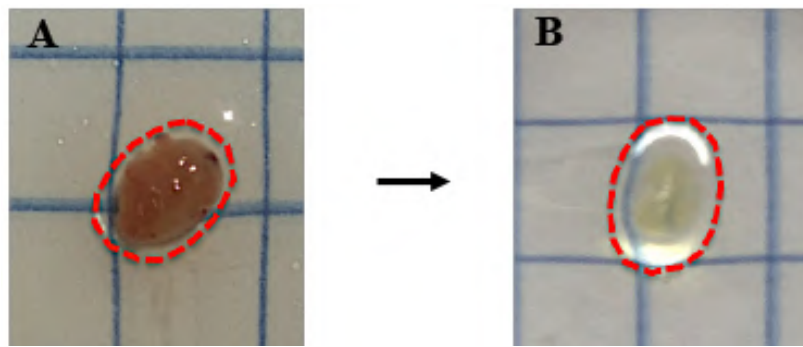


**Figure 20.** Ovary of a 6-week-old mouse fixed in 4% PFA **A)** before and **B)** after iDISCO+ protocol; note the resulting clearing of the organ.

To evaluate the antibodies and fluorescent dye ability to penetrate within the entire organ volume, optical images were acquired using the Leica SP8 confocal microscope equipped with a long working distance 25X objective; intact cleared ovaries were mounted into a well modelled with Sugru, an inert modulable glue, directly stack to a coverslip and filled with DBE.

Ovaries treated with the iDISCO+ in the absence of staining did not display tissue autofluorescence (data not shown); instead, when the ovary was labelled with the nuclear dye DAPI (Figure 21A) and a secondary antibody capable of binding mouse immunoglobulins naturally present within blood vessels (Figure 21B), this approach showed a good marking of both nuclear structures and vasculature ramifications (Figure 21C). Thanks to the high-resolution confocal images obtained, it was possible to observe all follicular types, from primordial T1 to pre-ovulatory T8. Also, the vascular network clearly emerged both as larger arterioles in the stroma (Figure 21C, arrow) and as very thin capillaries within the theca layers of growing follicles (Figure 21C, arrowheads).

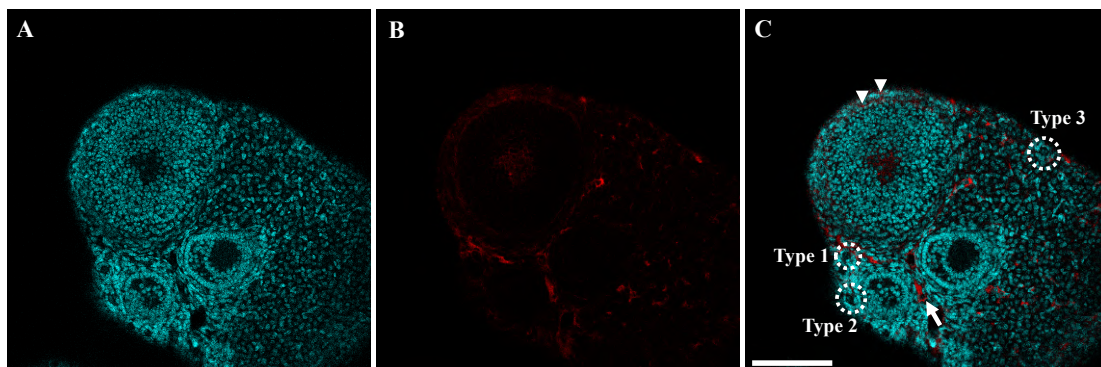


**Figure 21.** Representative section (25X) of a portion of a mouse ovary stained with **A)** DAPI and **B)** with anti-mouse IgG, highlighting cell nuclei and blood vessels, respectively; **C)** merge of both fluorescent signals showing the interaction between follicles and surrounding vasculature. Bar, 100  $\mu$ m.

The 3D organisation of the rich capillary meshwork surrounding each growing follicle was particularly visible when optical sections were processed to obtain their volume rendering (Figure 22).

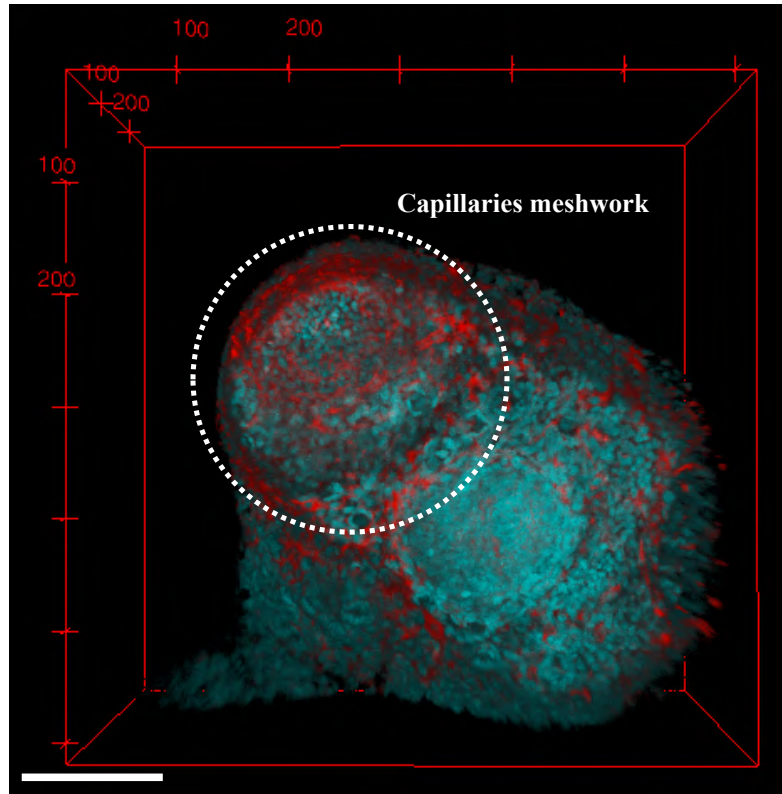


**Figure 22.** Volume rendering of a portion of a mouse ovary (25X) stained with DAPI and **B**) anti-mouse IgG, highlighting cell nuclei and blood vessels, respectively. The white circle highlights the external surface of a growing follicle surrounded by a rich capillaries meshwork. Bar, 100  $\mu$ m

Then, with the long-term goal to integrate the results obtained through the different pipeline steps, the compatibility of performing iDISCO+ after the tomographic procedure was evaluated. To this regard, an ovary previously analysed with microCT was treated with iDISCO+ and then stained with DAPI.

Figure 23 shows an adequate DAPI penetration and the proper maintenance of the 3D tissue organisation.

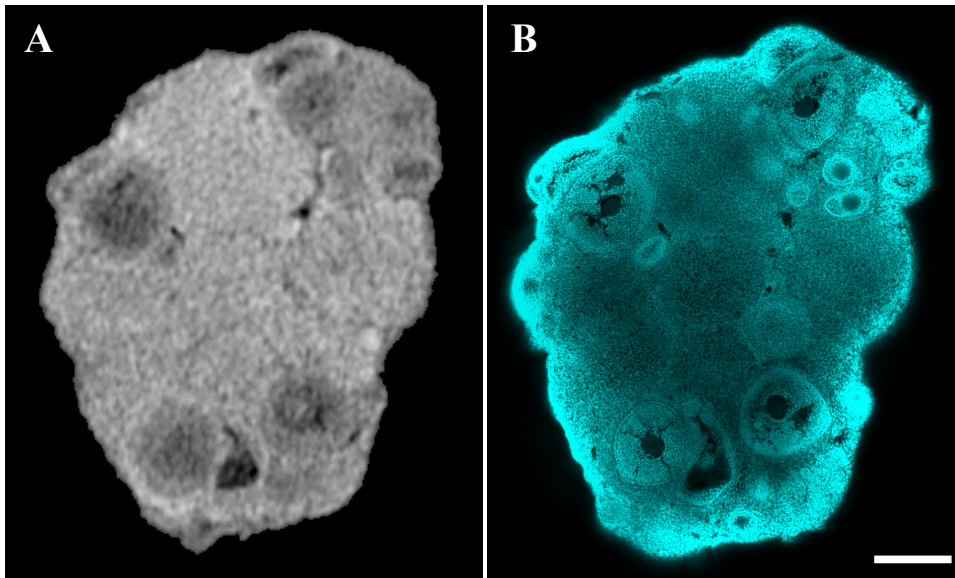


**Figure 23.** A) Representative microCT section acquired at  $5\mu\text{m}/\text{pixel}$ ; B) confocal image (25X) of the mouse ovary treated with iDISCO+ and stained with DAPI, that corresponds to the section shown in A). Bar,  $200\ \mu\text{m}$ .

Here, we presented a method for the whole-mount immunolabeling and volume imaging of the intact mouse ovary, that allowed the identification of all the follicles types, together with the surrounding capillaries meshwork.

At the time we started this analysis, the CLARITY method had been used for the clearing and 3D imaging of the mammalian ovary [67], [117]; however, we chose to optimise the iDISCO+ protocol for its broader compatibility with a wide panel of staining approaches and, also, because its reagents are readily available and costless [96], [106].

Since iDISCO+ was initially proposed for imaging the whole mouse brain or mouse embryos at different developmental stage, its optimisation for the study of the small ovary involved the modification of different incubation times, both for permeabilisation or blocking and for antibodies or dyes staining, starting from the short periods suggested for smaller embryos, but then reaching three days of antibody incubation used for more complex structures. This difficulty of making permeable the entire ovary may depend on the presence of the external tunica albuginea as well as the great abundance of connective tissue in the internal ovarian medulla.

Among the changes made so far with respect to the iDISCO+ protocol, organ perfusion has been replaced with ovary fixation in 4% PFA after its isolation. Given the small organ size (1x2x1 mm), the simple diffusion of the fixative through the tissue is sufficient to replace perfusion. Importantly, it allowed us to bring up the 3D vasculature architecture directly by targeting the immunoglobulins naturally present in the blood fixed within vessels.

A main limit emerged during the development of this method lies in the high corrosivity of the DBE, the solution in which the ovary reaches the refractive index matching and in which imaging is performed. The need to maintain the ovary immersed in DBE hinders the use of commercial microscopes because of the high risk to damage the microscope lenses. Thus, up to date, the analysis was carried out on single portions of the ovary by using a confocal microscope equipped with a 25X objective with a working distance of 1.5 mm. The 25X magnification as well as the limited working distance made difficult to image the entire organ surface and depth. Each ovarian single section, as the one shown in Figure 23, may be acquired only by stitching different field of views, resulting in an extremely time-consuming procedure.

To properly evaluate the diffusion capacity of antibodies and dyes within the volume, whole mount imaging through light-sheet microscopy would be needed [118]. To this regard, I am planning to take advantage of the results of a recent study on the mouse ovary which combines iDISCO+ with the clearing method named CUBIC [119], resulting in a more efficient penetration and in a final step based on the use of aqueous clearing reagents compatible with the most common light-sheet microscopes [106].

As further development of my research, I foresee the possibility to use, on the same organ, microCT imaging, followed by tissue clearing will allow to assemble a 3D model with data on the localisation and 3D organisation of the tiny primordial and primary follicles and of the thin capillaries surrounding growing follicles. Furthermore, when this approach will be used for the identification of molecules known to be markers of oocytes developmental

potential, i.e., Oct4, Stella or Nobox [120], [121], [122], this technique will allow the completion of the 3D mapping not only of the structures present in the ovary, but also of the quality, in terms of developmental competence, of the contained oocytes.

---

# Chapter 5

---

## Mass spectrometry

In this Chapter, I will present the first attempt to use MALDI-MSI combined with Liquid Chromatography Electrospray Ionization Tandem Mass Spectrometry (LC-ESI-MS/MS) to investigate the proteome of the entire mammalian ovary during folliculogenesis, and to identify *in-situ* the peptide signature of growing follicles.

### 5.1. LC-ESI-MS/MS analysis identifies the proteome of the mouse ovary

The LC-ESI-MS/MS analysis of a 25 dpn mouse ovary allowed the separation and the identification of its whole peptide content. Specifically, by using the Mascot software to search the peptide mass values against the SwissProt proteins database, 382 proteins were identified with a mass range comprised between 502 and 6,362.

The Protein-Protein Interaction Networks Functional Enrichment Analysis of the protein list using STRING (Search Tool for the Retrieval of Interacting Genes/Proteins) and KEGG (Kyoto Encyclopedia of Genes and Genomes) or Reactome, brought up, among several highly significant signalling pathways, PI3K-Akt (17 proteins;  $p < 0.003$ ), ECM-receptor interaction (12;  $p < 0.0001$ ), Cellular response to stress (25;  $p < 0.0001$ ), Cell cycle (22;  $p < 0.001$ ), Developmental Biology (16;  $p < 0.03$ ) and Cell surface interaction at the vascular wall (7;  $p < 0.02$ ).

Table 2 shows the results of the following PubMed analysis, which highlighted a crucial functional role for 75 out of the 382 proteins in the biology of the ovary, specifically in follicle growth ( $n = 21$ ), oocyte maturation ( $n = 9$ ), ovulation ( $n = 5$ ), oocyte quality ( $n = 26$ ), fertilisation ( $n = 3$ ), luteolysis ( $n = 1$ ), angiogenesis ( $n = 1$ ) and ovary pathologies ( $n = 9$ ).

**Table 2.** List of 75 proteins identified with LC-ESI-MS/MS analysis with a role in the biology of the ovary. TCs, theca cells; GCs, granulosa cells; CCs, cumulus cells; CL, *corpus luteum*; ER, endoplasmic reticulum; ECM, extracellular matrix.

## Mass spectrometry

Function	Protein	Cell type	Cell localisation
<b>Follicle growth</b>	ALDOA	Follicle and oocyte	Cytosol
	ANXA5	Follicle (GCs)	Ubiquitous
	APOE	Follicle (TCs)	ECM
	VIME	Follicle (GCs)	Cytoskeleton
	APOA1	Follicle (CCs)	ECM
	PAWR	Follicle (GCs)	Nucleus
	CALU	Follicle and oocyte	ER/Golgi/ECM
	GATA4	Follicle (GCs)	Nucleus
	SLTM	Follicle and oocyte	Nucleus
	SMC1A	Follicle and oocyte	Nucleus
	TPM2	Follicle (GCs)	Cytoskeleton
	LAMB2	Follicle (GCs)	ECM
	SGTA	Follicle and oocyte	Nucleus/Cytoplasm
	SF3A1	Follicle (GCs)	Nucleus
	HYOU1	Follicle (CCs)	ER
	RCN1	Follicle (GCs)	ER
	KI67	Follicle (GCs)	Nucleus
CIRBP	Follicle (CCs)	Nucleus	
NUMA1	Follicle (GCs)	Plasma membrane/Cytoskeleton/Nucleus	
CO3A1	Follicle (CCs)	ECM	
DESM	Follicle (CCs)	Plasma membrane/Nucleus	
<b>Oocyte maturation</b>	ACTBL	Oocyte	Cytoskeleton
	BIP	Oocyte	ER
	CALR	Follicle (CCs)	ER
	ENOA	Oocyte	Plasma membrane
	LAMA2	Oocyte	ECM
	NUCL	Oocyte	Nucleus
	PDIA4	Oocyte	ER
	PLIN1	Oocyte	ER
STMN1	Oocyte	Cytoskeleton	
<b>GV-to-MII transition and developmental competence</b>	MATR3	Oocyte	Nucleus
	DNMT1	Oocyte	Nucleus
	DNMT3A	Oocyte	Nucleus
	FLNA	Oocyte	Cytoskeleton
	FMR1	Follicle (GCs)	Nucleus/Plasma membrane
	KHDC3	Oocyte	Nucleus
	NASP	Oocyte	Nucleus
	SRSF1	Follicle (GCs)	Nucleus
	TOP2B	Oocyte	Nucleus
	UBB	Oocyte	Nucleus
	NALP5	Oocyte	Nucleus
	MAP1B	Oocyte	Cytoskeleton
	RBM3	Oocyte	Nucleus
	SFPQ	Oocyte	Nucleus
	DDX3X	Oocyte	Cytosol
	14-3-3T	Oocyte	Cytosol
	CD2AP	Oocyte	Cytoskeleton
	SAE1	Oocyte	Nucleus/Cytoplasm
	SUMO3	Oocyte	Nucleus
	EIF3A	Oocyte	Nucleus/Cytoskeleton/Cytoplasm
PDIA6	Oocyte	Plasma membrane/ER	
RBP2	Oocyte	Nucleus	
TOP1	Oocyte	Nucleus	
PRDX1	Oocyte	Cytoplasm	
DAB2	Oocyte	Nucleus	
NONO	Oocyte	Nucleus	
<b>Ovulation</b>	CSPG2	Follicle (GCs)	ECM
	NID2	Follicle (TCs)	ECM
	ZYX	Follicle (GCs)	Nucleus/Cytoskeleton
	PDIA3	Follicle (GCs)	ER
	GELS	Stroma, endothelial cells and follicle (TCs)	ECM/Cytoskeleton
<b>Fertilisation</b>	PPIA	Oocyte	Cytosol
	ZP3	Oocyte	Plasma membrane/ECM
	PEBP1	Oocyte	Cytoplasm
<b>Luteolysis</b>	DDX5	Follicle (CL)	Nucleus
<b>Angiogenesis</b>	TSP1	Endothelial cells	ER/ECM
<b>Ovary pathologies</b>	CCAR2	Ovary	Nucleus
	ADRM1	Ovary	Nucleus/Cytoplasm
	CHD4	Ovary	Nucleus/Cytoskeleton
	SET	Follicle (GCs)	Cytosol/ER/Nucleus
	LDHB	Follicle (CCs)	Cytoplasm
	HMG A2	Follicle (GCs)	Nucleus
	LARP4	Follicle (GCs)	Cytosol
	OGFR	Ovary	Nucleus
MYPT1	Ovary	Cytoskeleton	

## 5.2. Follicles classification, counting and annotation of the corresponding MALDI-MSI mass spectra

MALDI-MSI was performed on all the 133 sections obtained from a 25 dpn ovary. After histological staining, a total of 276 follicles were classified, based on histological features and dimensions [20] (Figure 24), and manually annotated with the SCiLS Lab MVS 2019c Pro software.

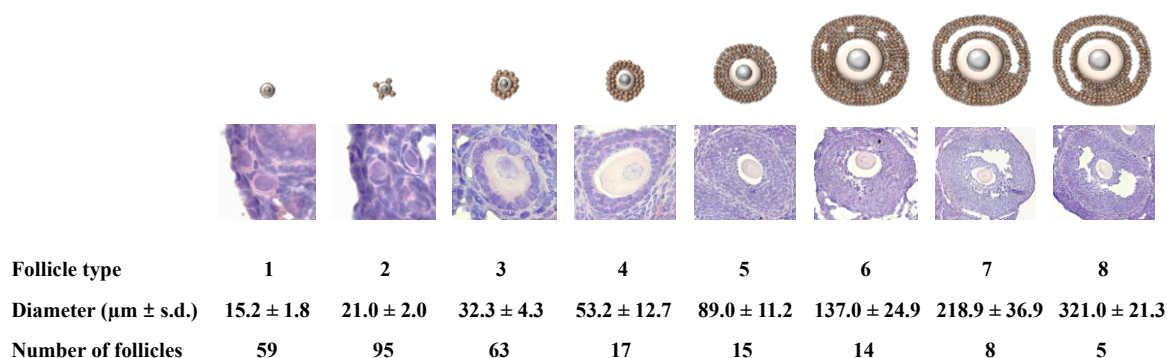


**Figure 24.** Classification of follicles from MALDI sections, based on size and histological features.

As a consequence of their volumetric expansion, follicles at different stages of folliculogenesis occupied an increasing number of sections. Primordial T1 and T2 follicles were comprised only in one section, primary T3 follicles in 2 - 3 sections and secondary T4 follicles in an average of 11 sections. Preantral T5 follicles were annotated in an average of 17 sections, T6 follicles in 19 sections, and the largest follicles T7 and T8 in 32 and 40 sections, respectively.

Using SCiLS Lab MVS 2019c Pro software, histological sections with the annotated follicles were co-registered with the mass spectra generated from the MALDI-MSI analysis. Through the process of co-registration, the absolute intensity of each peptide was associated with its histological localisation, thus allowing the maintenance of peptide *in-situ* spatial distribution (Figure 25A).

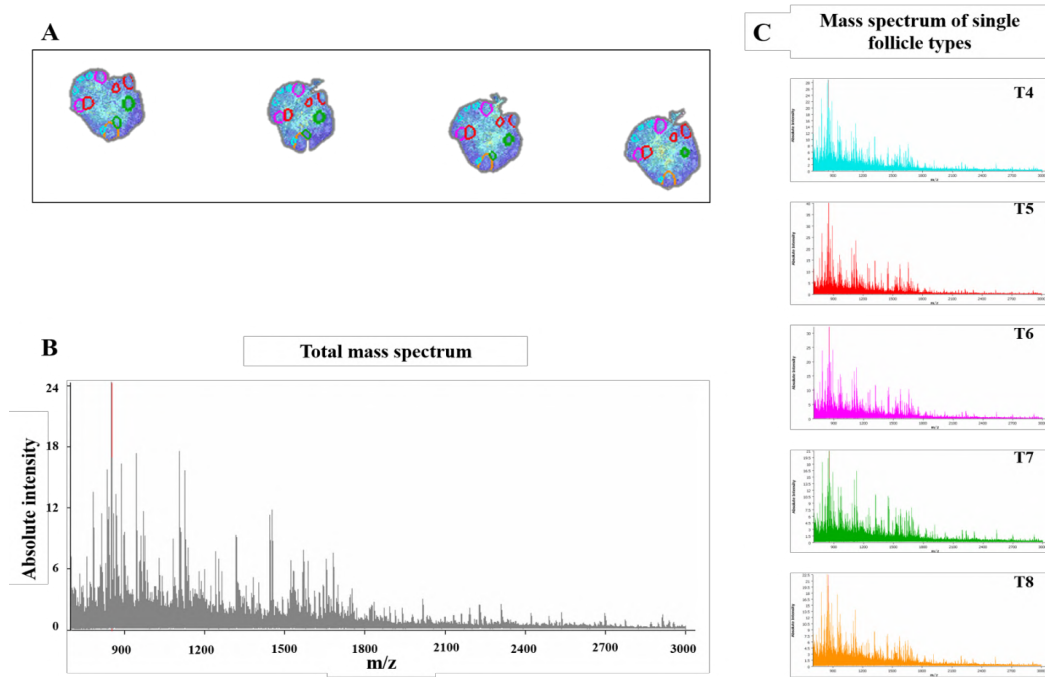


**Figure 25.** A) Follicles annotation on histological sections and co-registration of their mass spectra using SCiLS Lab MVS 2019c Pro software. B) The total mass spectrum generated from the MALDI-MSI analysis, in the x-axis the mass to charge ratio and in the y-axis the absolute intensity. C) Mass spectra of single follicle types; T4, light blue, T5, red, T6, pink, T7, green and T8, orange.

Annotations of all follicles, from the primordial to the pre-ovulatory, resulted in a total number of 56,200 mass spectra (Figure 25B). The mass spectrum of each follicle type is a plot with the x-axis representing the m/z value, whereas the y-axis displays the absolute intensity of each peptide.

T1, T2 and T3 follicles have a lower number of spectra (T1 = 32, T2 = 60 and T3 = 288) compared to the other classes (average number of spectra = 11,164), for this reason T1, T2 and T3 could not be included in the comparison, and thus they were excluded from subsequent analyses. The total number of spectra for T4, T5, T6, T7 or T8 was 1,674, 6,991, 7,628, 19,254 or 20,276, respectively. Since the number of spectra of T7 and T8 follicles was much higher compared to that of the other types, this difference was equilibrated by considering only those histological sections in which the oocyte was comprised. This choice led to the analysis of a comparable number of spectra (T7 = 6,740; T8 = 6,184) among follicle types.

### 5.3. Principal Component Analysis of MALDI-MSI mass spectra suggests follicle-specific peptide signatures during folliculogenesis

Mass spectra of each follicular class were compared to the entire mass spectra obtained grouping together all the classes. Figure 26 highlights the contribution of each follicle type (red cloud) to the overall data (grey cloud) and brings out the localisation changes occurring during follicle growth from the T4 to the T8 follicle. Within the Principal Component Analysis (PCA) 3D visualisation, mass spectra of T4 to T6 follicles appeared mostly clustered on the back view of the data cloud; whereas T7 and T8 spectra were mainly flipped on the opposite front view, as confirmed by the corresponding side views. Also, the side views suggested a shift in the 3D position, from left to right, during follicle growth from T5 to T8.

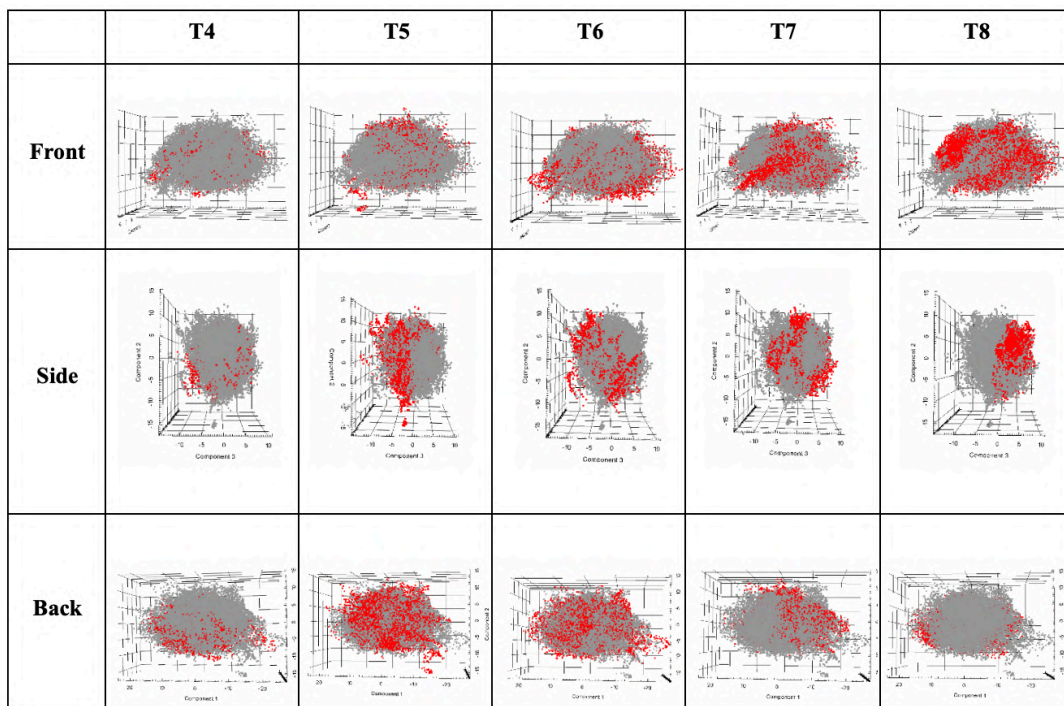


**Figure 26.** 3D Principal component analysis of each follicular class mass spectra (red) compared to the mass spectrum of all classes together (grey), visualised from the front, side and back view.

Then, PCA was performed to compare the mass spectra of each single follicle to those of its entire follicle class. To have a precise timing of their growth progression, follicles belonging to the same class were further classified and ordered by counting the number of granulosa cells at the equatorial section.

First, T4 are medium follicles surrounded by two layers of follicle cells and with a cell number comprised between 61 and 100 [20]. The 17 T4 follicles analysed presented a mean number of  $70 \pm 13$  granulosa cells and an average number of spectra of  $98 \pm 50$  (Table 3).

The comparison of the spectra of the whole 17 annotated T4 follicles (Figure 27, blue cloud) with the spectrum of each single T4 (Figure 27, red cloud) highlighted a defined spatial localisation within the PCA 3D representation of T4.4, T4.5 and T4.16 follicles; instead, T4.6, T4.11, T4.15 and T4.17 were more dispersed within the blue cloud.

However, the lower number of mass spectra recorded for T4 resulted in a more scattered data representation compared to that of the subsequent follicular types.

**Table 3.** Histological and Mass spectrometry parameters of 17 T4 follicles: number of spectra and number of follicle cells at the equatorial section (a classification procedure proposed by Pedersen and Peters, 1968).

<b>Follicle</b>	<b>Number of spectra</b>	<b>Number of follicle cells (equatorial section)</b>
T4.1	136	48
T4.2	13	50
T4.3	72	53
T4.4	41	58
T4.5	100	62
T4.6	103	67
T4.7	71	68
T4.8	108	69
T4.9	53	71
T4.10	71	73
T4.11	171	74
T4.12	34	77
T4.13	130	79
T4.14	88	80
T4.15	150	84
T4.16	187	90
T4.17	146	92
<b>Mean ± St. Dev.</b>	<b>98 ± 50</b>	<b>70 ± 13</b>

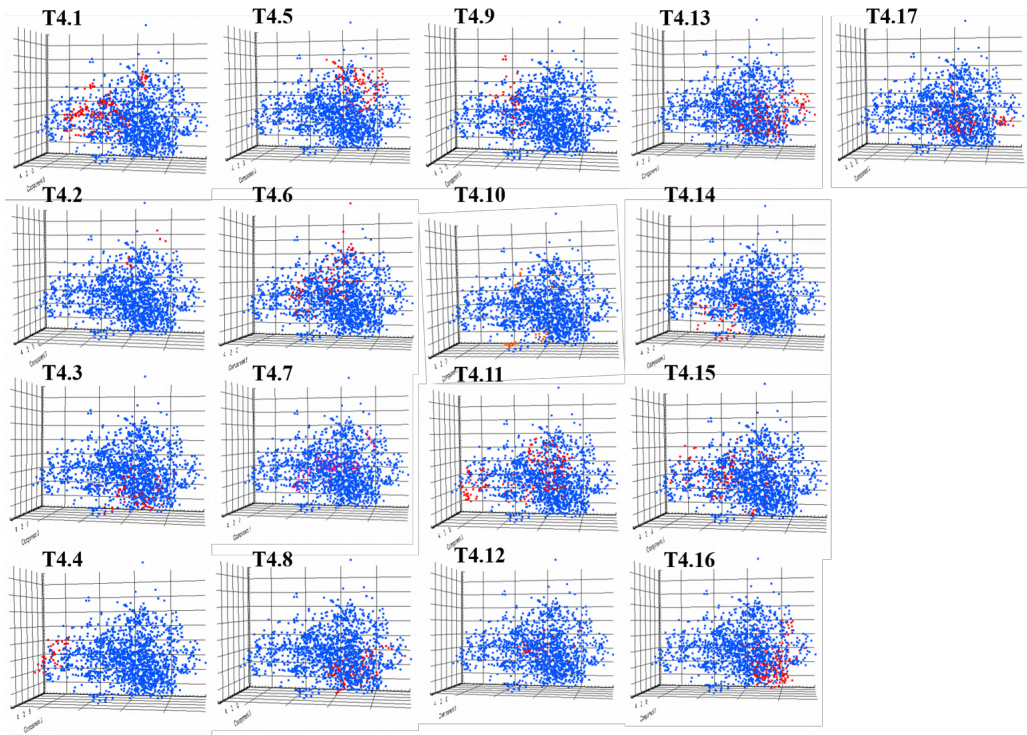


**Figure 27.** Principal component analysis of 17 T4 follicles mass spectra. In blue, the whole mass spectra of T4 follicles, whilst in red each selected follicle.

T5 is a transitory class, between medium and large follicles, identified based on size, number of follicle cells at the equatorial section and histological features, such as the absence of an antrum and more than two layers of granulosa cells (Table 4). T5 has a number of follicle cells comprised between 101 and 400 [20]. The number of T5 follicle cells at the equatorial region ranged between 92 and 486, with a mean of  $466 \pm 343$ , the average number of spectra for T5 follicles was  $217 \pm 114$ , attesting the high variability and heterogeneity intrinsic to this class.

Interestingly, groups of T5 showed a similar PCA spatial localisation: T5.1 – T5.4 (bottom of the blue cloud), T5.5 – T5.9 (top of the blue cloud), whereas the remaining T5.10 – T5.15, while remaining individually clustered, displayed a specific spatial localisation (Figure 28).

**Table 4.** Histological and Mass spectrometry parameters of 8 T5 follicles: number of spectra and number of follicle cells at the equatorial section.

Follicle	Number of spectra	Number of follicle cells (equatorial section)
T5.1	136	92
T5.2	205	105
T5.3	435	131
T5.4	100	138
T5.5	147	138
T5.6	200	142
T5.7	307	147
T5.8	174	180
T5.9	345	208
T5.10	827	226
T5.11	364	228
T5.12	1,010	300
T5.13	841	359
T5.14	973	376
T5.15	927	486
<b>Mean ± St. Dev.</b>	<b>466 ± 343</b>	<b>217 ± 114</b>

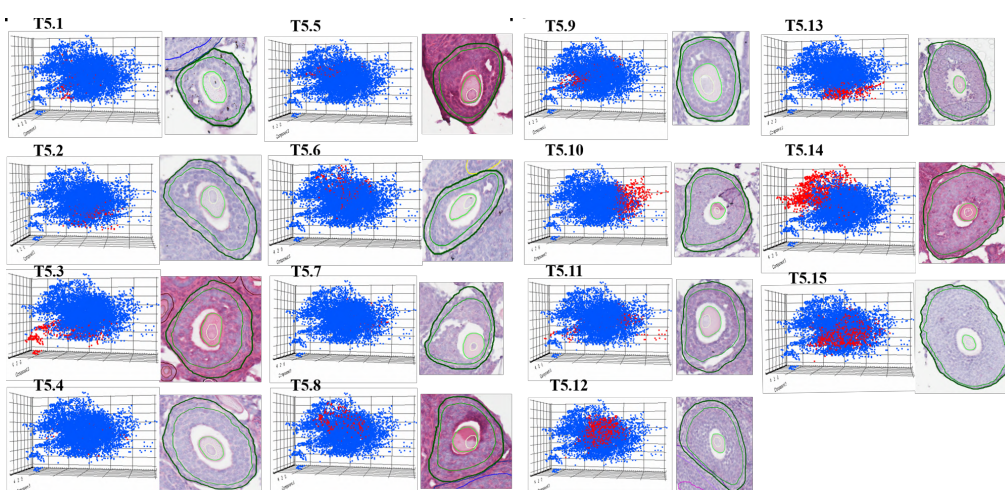


**Figure 28.** Principal component analysis of 8 T5 follicles mass spectra and their corresponding equatorial histological sections. In blue, the whole mass spectra of T5 follicles, whilst in red each selected follicle.

T6 are large follicles with many layers of granulosa cells that surround the oocyte, small cavities filled with follicular fluid, and the number of cells in the largest cross-section comprised between 401 and 600 [20].

The entire T6 class displayed an average number of follicle cells at the equatorial section of  $449 \pm 149$  and an average number of spectra of  $545 \pm 345$  (Table 5).

When analysed with PCA, T6.1, T6.2, T6.3, T6.4, T6.6, T6.8, T6.10 and T6.12 follicles resulted distributed on the left-hand side of the blue cloud; whereas T6.5, T6.7, T6.9, T6.11, T6.13 and T6.14 were located on the right-hand side (Figure 29). Most follicles on the left-hand side were T6 small follicles with an average number of follicle cells at the equatorial section of  $390 \pm 126$ . On the contrary, T6 follicles on the right-hand side of the PCA plot were larger in size and had a number of follicle cells at the equatorial section of  $528 \pm 150$ .

**Table 5.** Histological and Mass spectrometry parameters of 14 T6 follicles: number of spectra and number of follicle cells at the equatorial section.

<b>Follicle</b>	<b>Number of spectra</b>	<b>Number of follicle cells (equatorial section)</b>
T6.1	162	250
T6.2	665	308
T6.3	369	311
T6.4	455	328
T6.5	339	360
T6.6	293	385
T6.7	980	417
T6.8	328	418
T6.9	1,255	459
T6.10	209	467
T6.11	1,129	523
T6.12	452	650
T6.13	358	652
T6.14	634	755
<b>Mean <math>\pm</math> St. Dev.</b>	<b>545 <math>\pm</math> 345</b>	<b>449 <math>\pm</math> 149</b>

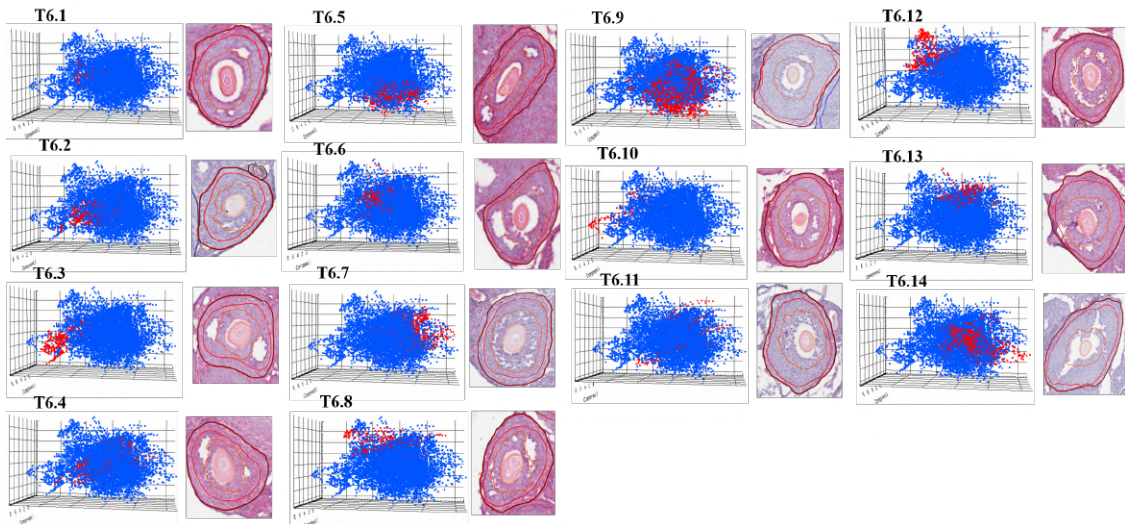


**Figure 29.** Principal component analysis of 14 T6 follicles mass spectra and their corresponding equatorial histological sections. In blue, the whole mass spectra of T6 follicles, whilst in red each selected follicle.

T7 are large follicles with a single cavity filled with follicular fluid and more than 600 cells on the largest cross-section [20]. Eight T7 follicles were annotated, with a number of follicle cells at the equatorial section between 477 and 1,310 (Table 6). The average number of follicle cells was  $993 \pm 254$ , and number of T7 mass spectra  $842 \pm 346$ .

After PCA, T7.2, T7.4 and T7.7 spectra appeared localised at top position within the blue cloud, whereas T7.3, T7.6 and T7.8 localised at the bottom and T7.1 and T7.5 showed a more dispersed localisation between top and bottom (Figure 30).

**Table 6.** Histological and Mass spectrometry parameters of 8 T7 follicles: number of spectra and number of follicle cells at the equatorial section.

<b>Follicle</b>	<b>Number of spectra</b>	<b>Number of follicle cells (equatorial section)</b>
T7.1	302	477
T7.2	763	895
T7.3	941	922
T7.4	455	963
T7.5	993	1,052
T7.6	1,193	1,098
T7.7	772	1,225
T7.8	1,321	1,310
<b>Mean ± St. Dev.</b>	<b>842 ± 346</b>	<b>993 ± 254</b>

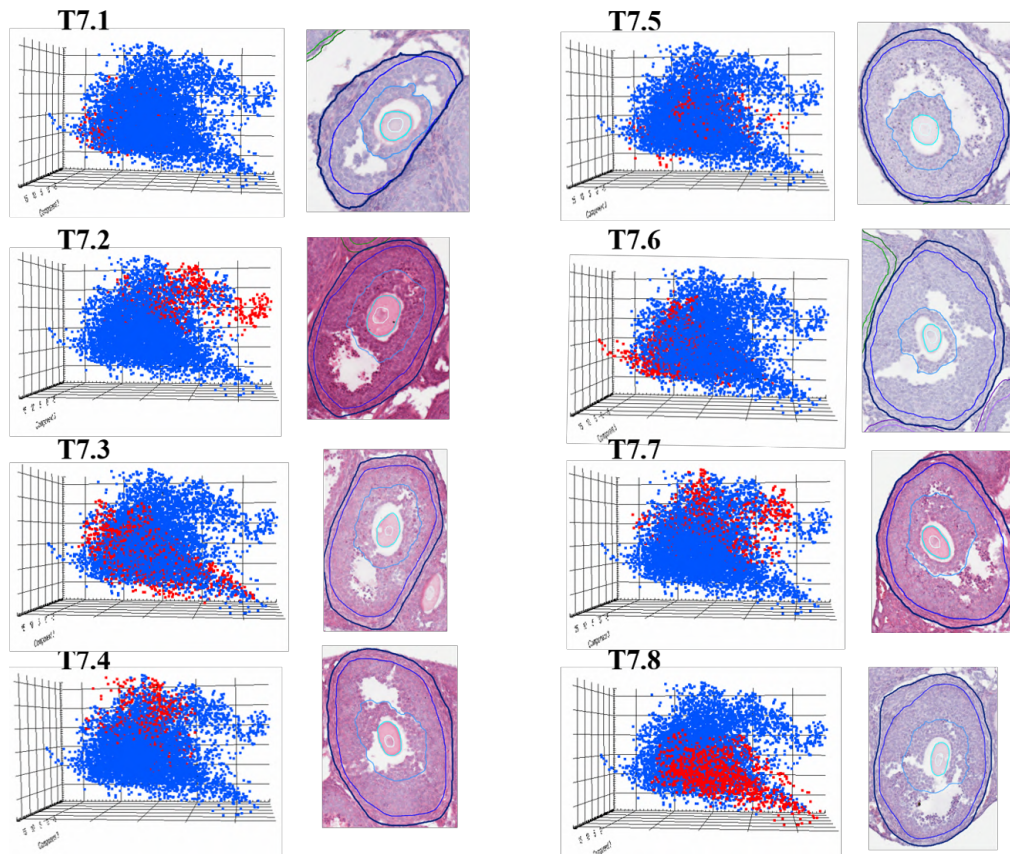


**Figure 30.** Principal component analysis of 8 T7 follicles mass spectra and their corresponding equatorial histological sections. In blue, the whole mass spectra of T7 follicles, whilst in red each selected follicle.

Finally, T8 are large pre-ovulatory follicles with a single cavity of follicular fluid and a well-formed cumulus stalk [20]. The 5 annotated T8 follicles displayed  $1,066 \pm 212$  follicle cells at the equatorial section (Table 7), and  $1,568 \pm 589$  mass spectra. PCA analysis highlighted the presence of two main spectra clusters: a major one formed by T8.1, T8.2, T8.3 and part of T8.5, and a smaller cluster constituted by T8.4 and part of T8.5 (Figure 31).

**Table 7.** Histological and Mass spectrometry parameters of 5 T8 follicles: number of spectra and number of follicle cells at the equatorial section.

Follicle	Number of spectra	Number of follicle cells (equatorial section)
T8.1	1,210	846
T8.2	2,412	872
T8.3	1,658	1,095
T8.4	849	1,164
T8.5	1,713	1,354
<b>Mean <math>\pm</math> St. Dev.</b>	<b>1,568 <math>\pm</math> 589</b>	<b>1,066 <math>\pm</math> 212</b>

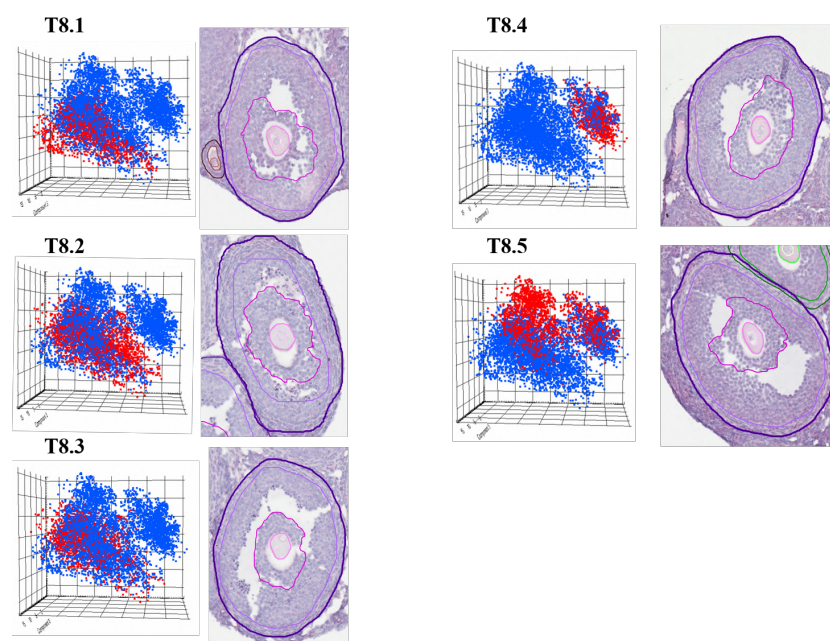


**Figure 31.** Principal component analysis of 5 T8 follicles mass spectra and their corresponding equatorial histological sections. In blue, the whole mass spectra of T8 follicles, whilst in red each selected follicle.

## 5.4. Receiver Operating Characteristic (ROC) analysis of T8 mass spectra highlights differences in the peptide content within the pre-ovulatory follicle class

To further investigate the differences emerged from the PCA, we performed a ROC analysis comparing the two follicles with the most separated spectra (T8.1 vs T8.4), which revealed the presence of 45 differentially expressed proteins ( $p < 0.001$ ), 43 up-regulated and 2 down-regulated in T8.1 follicle (Table 8). Nine of these 45 differentially expressed proteins have a specific key function in the biology of the ovary.

**Table 8.** Forty-five proteins differentially expressed in the comparison between T8.1 vs T8.4. In green, up-regulated proteins; in red, down-regulated proteins; in bold, proteins with a key function in the biology of the ovary.

Protein name	T8.1 vs T8.4	Protein name	T8.1 vs T8.4
<b>14-3-3T</b>		LRC47	
14-3-3Z		MYH11	
BD1L1		<b>NALP5</b>	
CO1A1		<b>NUCL</b>	
CO6A2		RAIN	
<b>CSPG2</b>		RANB3	
DDX17		RBMX	
<b>DNMT1</b>		RL19	
FNBP4		RL6	
FUBP1		RL7A	
H12		ROA0	
H15		ROA1	
H3C		ROA2	
H4		ROA3	
HNRPC		RS25	
HNRPK		RSSA	
HS90B		SAFB1	
<b>HYOU1</b>		SF3B1	
K1C14		<b>SMC1A</b>	
K1C17		SYEP	
<b>KHDC3</b>		TKT	
<b>LAMA2</b>		TPIS	
LAP2A			

This study is the first that combines the use of MALDI-MSI and LC-ESI MS/MS on the mammalian ovary and represents proof-of-concept of the possibility to draw a map of the peptide content of each follicle type growing inside the female gonad.

Through the use of LC-ESI-MS/MS analysis of the 25 dpn mouse ovary, we build up the first reference dataset for mouse ovarian proteins. Among the 382 proteins identified, the enrichment analysis highlighted the presence of molecules involved in ECM remodelling and PI3K-Akt signalling pathway, both crucial for primordial follicle activation and subsequent growth. In particular, when integrins, mechanoreceptors present in the oocyte membrane, receive strong biomechanical signals from the extracellular matrix surrounding the primordial follicle, they induce PI3K phosphorylation and activate a cascade of events that leads to the suppression of the transcriptional activity of FOXO3, an important quiescence regulator [29], [31].

The subsequent PubMed analysis highlighted 75 out of 382 proteins that play a key role in ovarian biology. Among these, we identified important maternal-effect factors, i.e., oocyte-stored molecules which regulate the early phase of differentiation and development beyond the two-cell stage, before the embryonic genome activation [123]. Worth mentioning are DNMT1, DNMT3A, NALP5 and KHDC3 [123]. DNA methyltransferases (DNMTs) are enzymes that add methyl groups to cytosines within CpG sites, causing an epigenetic modification of the DNA sequence. During oocyte growth, the expression of *DNMT* genes increases gradually [32]. DNMT1 contributes to the maintenance of CpG methylation in oocytes and early embryos, whilst DNMT3A is involved in *de novo* methylation, the transfer of methyl groups to unmethylated DNA regions. NALP5 and KHDC3 are maternal-effect factors whose accumulation inside the oocyte increases gradually during maturation. They participate in the subcortical maternal complex (SCMC) that is essential for cleavage-stage embryogenesis. Indeed, embryos lacking NALP5 fail to progress beyond the two-cell stage [124], and KHDC3 protein depletion during pre-implantation development causes an abnormal spindle assembly and chromosome misalignments that lead to a high incidence of aneuploidy [125].

Also, LC-ESI-MS/MS identified the presence of ZP3, one of the three mouse glycoproteins that form the zona pellucida, a specialised ECM critical for the oocyte and follicle growth, and involved, at the time of fertilisation, in species-specific sperm-egg binding, induction of acrosome reaction and prevention of polyspermy [113]. Recent studies demonstrated that in homozygous knockout mice for *Zp2* and *Zp3*, alterations to ZP layer result in infertility [126], [127].

Since the organ was entirely serially sectioned to allow the acquisition of information on the whole follicles throughout folliculogenesis, thousands mass spectra for each follicle type were recorded. The mass spectra generated with MALDI-MSI were analysed with PCA either to highlight the similarities and/or differences between different follicular classes during the folliculogenetic process, or to compare each single follicle to all those belonging to the same follicle class.

PCA comparing the mass spectra of individual follicle types with the entire folliculogenesis highlighted a clustered localisation that, although not

significantly different, suggests a progressive change in peptide content during follicle growth from the preantral T5 to the fully-grown antral T8 follicle (Figure 26). The inability of ROC analysis to highlight statistically significant differences in the comparison between the types of follicles during folliculogenesis may be explained by the high variability of data within each defined class. Moreover, a major problem when analysing a differentiation process like folliculogenesis, which is a *continuum* of growing moments, is the difficulty to define a clear separation between adjacent classes based on cytological features (e.g., the follicle diameter, the number of layers of granulosa cells, or the antrum composition), that do not fully reflect changes in terms of more subtle molecular markers.

Future work will be done to investigate more in depth and with more sensitive and specific statistical tools these differences, and, in order to account for possible biological individual differences and to strengthen the statistical analysis, we will increase the number of analysed ovaries to at least five from different mice.

Then, PCA pointed out that mass spectra of each single follicle tend to localise in a specific 3D space in respect to the mass spectra of the whole follicle class. Interestingly, PCA showed also the presence of two distinct mass spectra clusters in T8 follicle class (Figure 31). To further investigate this difference, we performed ROC analysis between T8.1 and T8.4, the two most separated T8 follicles, revealing a strong significant difference was between T8 follicles, with 45 proteins differentially expressed. Of them, 9 have a specific function in the folliculogenetic process: DNMT1, NALP5 and KHDC3 (maternal-effect factors previously described) 14-3-3T, HYOU1, CSPG2, LAMA2, SMC1A, NUCL.

As a member of the 14-3-3 family, 14-3-3T is involved in numerous regulatory processes, and is expressed in mouse oocytes and eggs to maintain the phosphorylated status of cell division cycle 25 (CDC25) and sequester it in the oocyte cytoplasm [128], [129]. This maintains the oocyte in meiotic arrest through the activation of protein kinase A (PKA), which phosphorylates and, in turn, activates the oocyte-specific kinase WEE2 and, at the same time, phosphorylates and inactivates CDC25B phosphatases. Both mechanisms cooperate in the maintenance of the inactive state of cyclin-dependent kinase 1 (CDK1), a molecule that promotes oocyte meiotic resumption [129].

Hypoxia upregulated 1 (HYOU1) belongs to the heat shock protein 70 family and has a pivotal role in cytoprotective cellular mechanisms triggered by oxygen deprivation. HYOU1 transcripts were significantly more abundant in cumulus cells from aged mares, perhaps indicating high levels of stress [130].

CSPG2 is an abundant ECM proteoglycan, produced by mural granulosa cells and accumulated within the COC expanding matrix. At the time of ovulation requires correct ECM cyclical remodelling and CSPG2 cleavage, induced by the extracellular metalloprotease ADAMTS1, is required for ECM remodelling and follicle rupture [131]. Importantly, knockout *Adamts1* mice display lower CSPG2 cleavage in COCs and reduction of ovulation rate and fertility [132]. Moreover, CSPG2 decreased serum levels in women affected by

PCOS suggest a possible role of this protein in the pathogenesis of this disease [133].

LAMA2 is mainly expressed in the theca compartment of growing follicles. As part of the follicular ECM, it supports oocyte growth, survival and maturation [134]. It plays also a role in the attachment, migration and organisation of cells into tissues during embryonic development [135].

SMC1A protein is a structural component of the cohesin complex that ensures correct chromosome segregation during mitosis and meiosis. In aged oocytes, reduction of cohesin during prophase I arrest contributes to chromosome segregation errors, and, if the aged oocyte is fertilized, zygotic trisomy occurs [136]

Nucleolin (NUCL) is a multifunctional protein involved in late stages of ribosome biogenesis, localised in the nucleolar compartment. Oocytes ready for ovulation contain atypical nucleoli, named nucleolus precursor bodies, that are essential for the re-establishment of a functional nucleolus in pre-implantation development [137]. Perhaps, NUCL protein of maternal origin is used for zygotic nucleolus genesis and it has protective functions under cellular stress conditions [138].

Even if preliminary, the different amount of the 9 proteins described above might be explained with the presence within the pre-ovulatory T8 compartment of follicles with different quality, thus reflecting the up-/downregulation of key maternal-effect proteins stored inside the oocyte and crucial for pre-implantation development.

An important step to improve our work will involve, in agreement with our collaborators at the University of Milano Bicocca (Prof. Magni, School of Medicine and Surgery), the use of a more accurate 10  $\mu\text{m}$  laser pixel width mass spectrometer, which should allow completion of the peptide profile throughout the whole adult folliculogenesis, including T1 – T3 follicles.

Also, when extended to the study of ovarian tissue and folliculogenesis under pathological conditions, MALDI-MSI could be a key instrument to better understand their aetiology, reconstructing the main molecular changes leading to the activation/silencing of involved signalling pathways, or could bring up new important diagnostic and therapeutic biomarkers [100].

---

# Chapter 6

---

## Histology

### 6.1. Confocal histology

A further layer of investigation that is intended to bring out cyto-functional information from the whole ovary is given by the histological analysis of the organ that has been previously studied with the methods described above. To this end, here I will describe a novel method that we developed, combining the use of the classical Eosin staining, its fluorescent properties and a confocal microscopy analysis.

#### 6.1.1. Two-photon microscopy brings up the fluorescent property of Eosin

Eosin Y (E) is an acidic histological dye, a derivate of fluorescein, that stains basic positively charged structures, i.e., mitochondria and cytosolic or ribosomal proteins [139].

A recent study showed that E displays also strong fluorescent properties when analysed in solution at 830 nm with two-photon excited fluorescence microscopy (TPEF) [140]; whereas, this feature was lacking for Hematoxylin (H), generally used in combination with E.

Using a TPEF designed and built at the Laboratory of Nonlinear Optics and Ultrarapid Spectroscopy (University of Pavia) headed by Profs. Tomaselli and Tartara, we investigated the E fluorescence property directly on 6- $\mu\text{m}$  ovary histological sections, used alone or in combination with H. Figure 32 summarises the results obtained with the TPEF analysis of serial sections from the same Bouin-fixed ovary in the absence of staining, stained with H&E, and with H or E only. The analysis was performed under the same imaging conditions at the excitation wavelength of 830 nm. Figure 32A-B shows that the Bouin's fixative did not present fluorescent properties when excited at 830 nm, therefore the signal subsequently obtained was exclusively dependent on the dye used. First, a fluorescent signal was visible in sections treated with the traditional combination of H and E (Figure 32C-D). Then, sections stained with

H only did not show fluorescence (Figure 32E-F), which instead was clearly detectable in those treated only with E (Figure 32G-H).

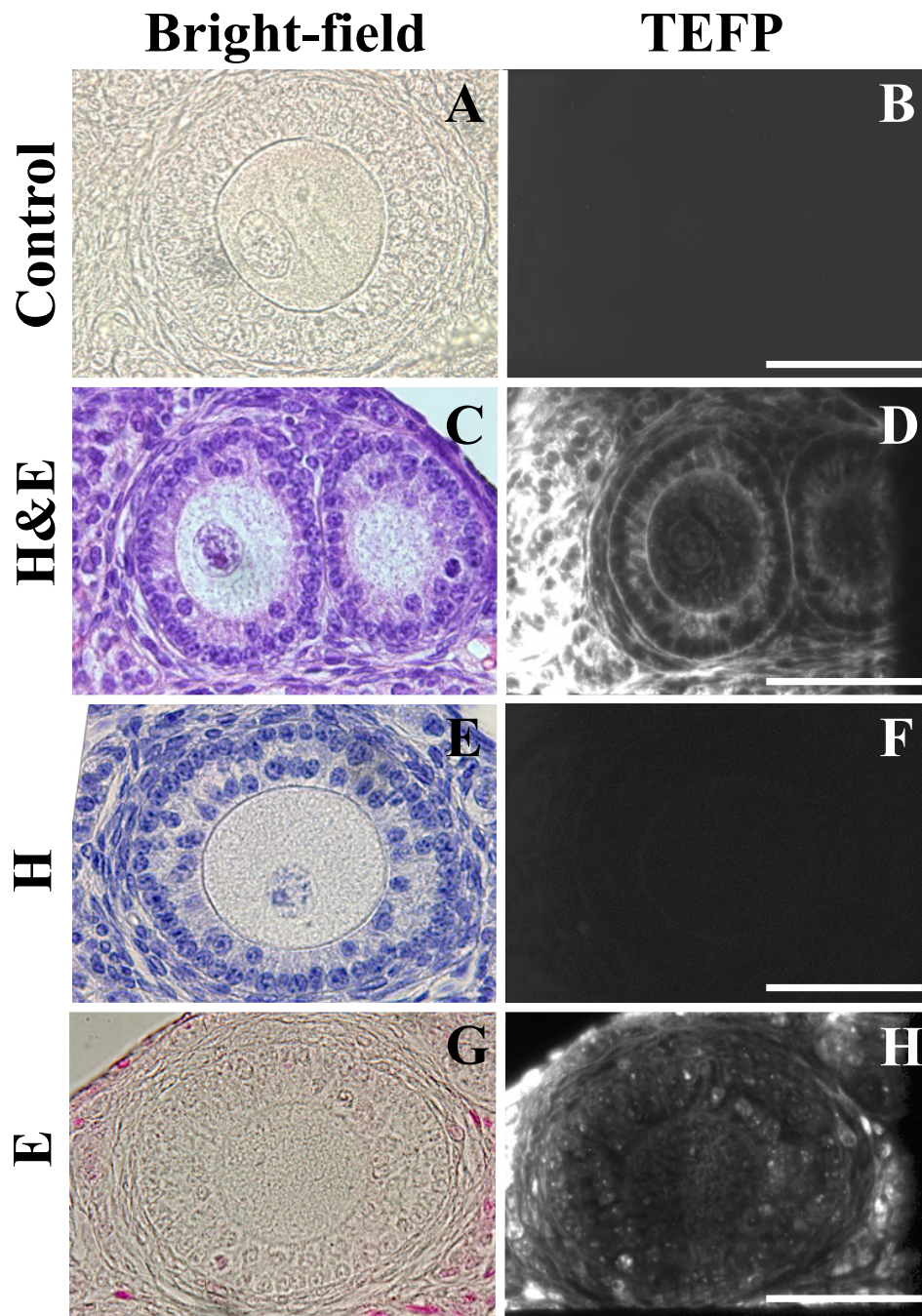


**Figure 32. Comparison of bright-field and TPEF imaging of ovarian follicle sections.** A-B) Section of a preantral follicle that, in absence of histological dyes, does not present fluorescent properties; C-D) Fluorescent signal in ovarian follicles section stained with H and E; E-F) Sections stained with H-only does not show fluorescence; G-H) Follicle section stained with E displays fluorescent signal. Bar, 50  $\mu\text{m}$ .

These results confirmed the observation made by Hasani et al. [140] on E fluorescence in solution; however, the major drawbacks of the TEPF instrument used were the limited field of view, due to the exclusive presence of a 60X objective, and the axial resolution in the range of 1.5-1.2  $\mu\text{m}/\text{pixel}$ , which made difficult the accurate imaging and identification of the subcellular elements localised within the histological section thickness.

Thus, these experimental data laid the bases to define an experimental approach that combined the E staining of ovarian sections and the analysis at the confocal microscope day (SP8, Leica), a more versatile instrument allowing not only a wider and tuneable field of view, but also the automated stitching of entire ovarian sections. Moreover, confocal microscopy allows the observation of the inside of a thicker histological section by returning digital serial images as thin as the instrumental axial resolution limit of 0.2  $\mu\text{m}/\text{pixel}$ .

### 6.1.2. Eosin stains the protein components of ovarian tissue, follicle cells and oocytes

Figure 33 shows a comparison between the same section of a preantral follicle acquired with TPEF (Figure 33A) or confocal microscopy (Figure 33B), in which it emerges that the confocal acquisition at the excitation wavelength of 520 nm generates a better signal-to-noise-ratio, allowing a clearer identification of protein-rich regions such as nuclei and cell membranes of all the ovarian cells, from stromal to follicular cells and oocytes, and, in particular, the zona pellucida and the oocyte's nucleolus (Figure 33B, white arrow and red arrowhead, respectively).

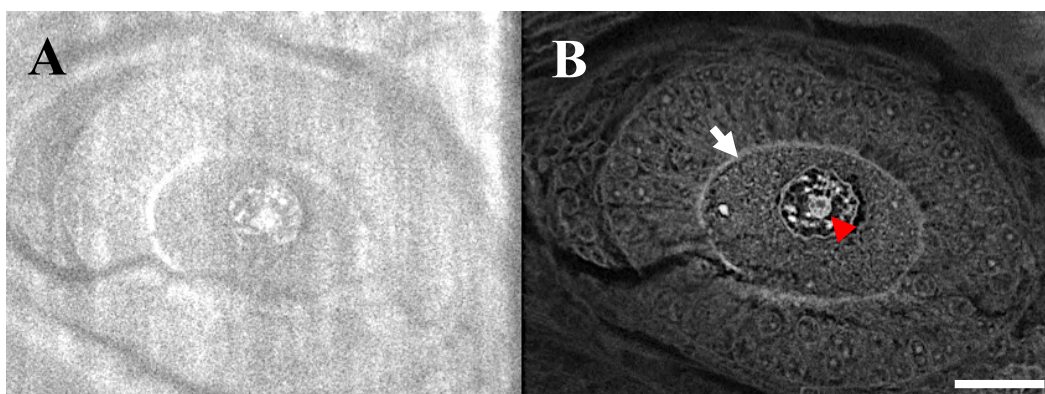
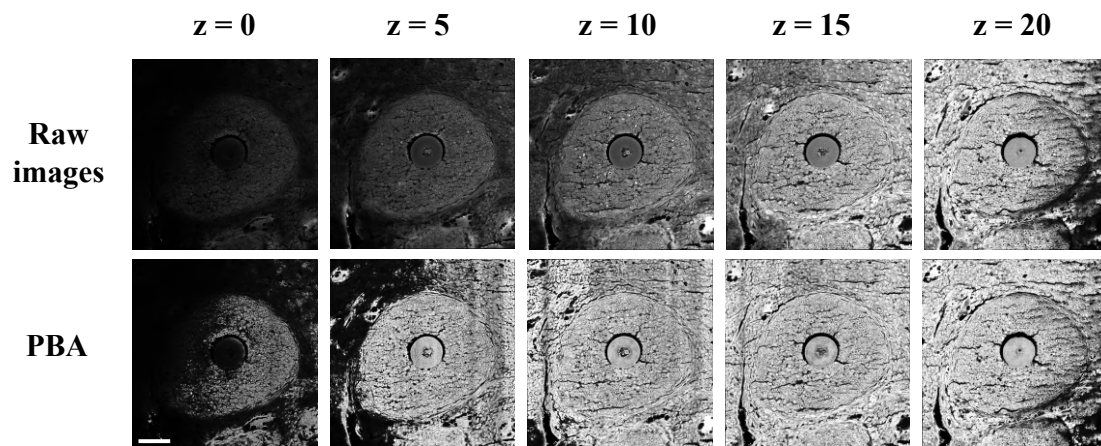


**Figure 33.** Representative cross section of a preantral follicle acquired with **A)** TPEF and **B)** Leica SP8 confocal microscope. Bar, 20  $\mu\text{m}$ .

### 6.1.3. Confocal microscopy reveals an accurate topography of follicles within the 20 $\mu\text{m}$ -thick ovarian sections and describes the chromatin organisation of the enclosed SN or NSN oocytes

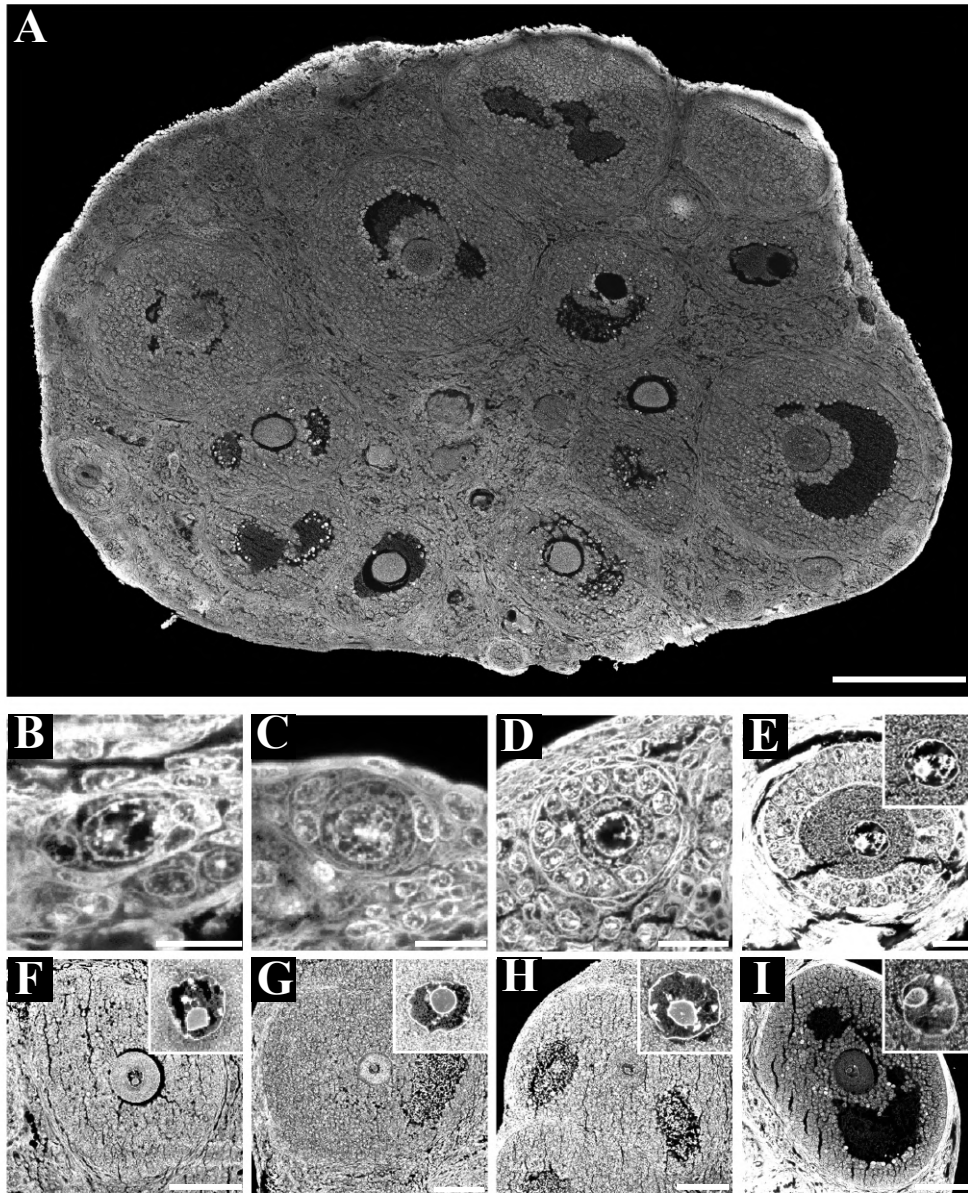
Paraffin-embedded samples were cut in 20, 30 or 50  $\mu\text{m}$ -thick serial sections. For each section thickness, three E staining time intervals were tested, namely 30 sec, 1 min or 1 min and 30 sec. Among these conditions, independently of the section thickness, 30 sec and 1 min resulted in inadequate staining, limited to the section surface or inhomogeneous across the depth, respectively; the 1 min and 30 sec staining of 20, 30, and 50  $\mu\text{m}$ -thick sections always displayed a good dye penetration until the nineteenth optical image, independently of the tissue thickness (data not shown). Thus, 20  $\mu\text{m}$  sections were those that allowed a more homogeneous penetration of Eosin throughout the whole thickness, and, at the same time, the not excessively long staining period prevented tissue saturation and the formation of dye precipitates.

The presence of a slight E staining gradient, from the section surface exposed to the dye to that stuck to the glass, was further corrected by processing the acquired image stacks with the Plane Brightness Adjustment plug-in implemented in ImageJ [141]. Figure 34 shows the improved signal-to-noise ratio of the processed stack compared to that of raw images.



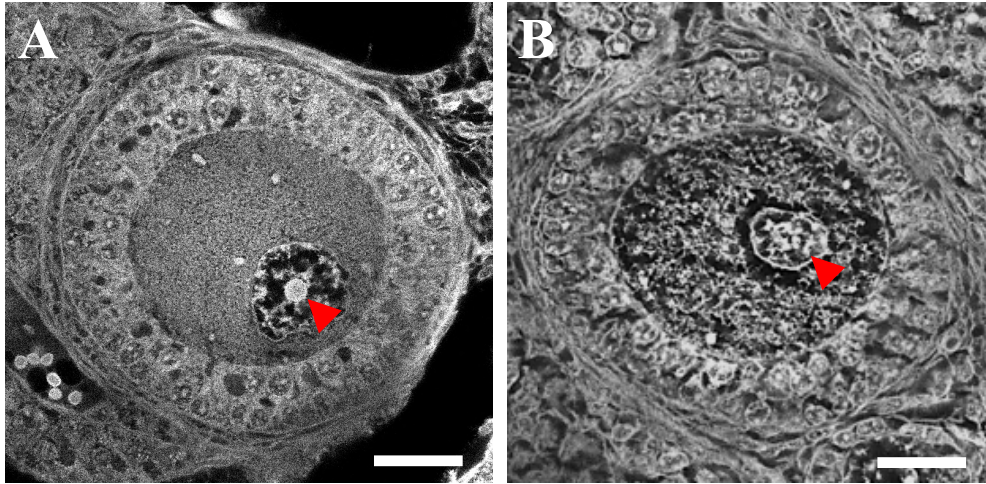
**Figure 34.** Representative optical sections of a preantral follicle acquired every 5  $\mu\text{m}$  before (upper row, Raw images) and after the Plane Brightness Adjustment (PBA) plug-in application (lower panel). Bar, 50  $\mu\text{m}$ .

Figure 35A shows the surface of a 20  $\mu\text{m}$ -thick ovarian section on which we identified all the follicle types from T1 (Figure 35B) to T8 (Figure 35I). Enlargements from the preantral T5 to the pre-ovulatory T8 display the SN nucleolar chromatin organisation type of the enclosed oocytes.



**Figure 35.** A) Representative E-stained ovarian section (40X) acquired with the SP8 Leica confocal microscope and put together using a stitching procedure; B-I) Confocal histology representation of the whole folliculogenesis, from T1 to T8. Enlargements (63X) from the secondary T4 to the pre-ovulatory T8 display the SN nucleolar chromatin organisation of the enclosed oocytes. Bar: A, 200  $\mu\text{m}$ ; B-C, 10  $\mu\text{m}$ ; D-E, 20  $\mu\text{m}$ ; F-I, 100  $\mu\text{m}$ .

Confocal histology of E-stained ovarian sections permitted to analyse the chromatin organisation of all the oocytes present within the ovarian tissue section allowing their classification into SN (Figure 36A) or NSN (Figure 36B).



**Figure 36.** **A)** Preantral follicle with E-positive chromatin ring (red arrowhead) within the nucleolus of the enclosed SN oocyte; **B)** Preantral follicle enclosing a NSN oocyte with dispersed chromatin in the nucleus (red arrowhead). Bar, 20  $\mu\text{m}$ .

## 6.2. Classical histology

Finally, another step that ends the pipeline of the ovary 3D analysis and is alternative to Confocal histology, concerns with the use of classical histology to produce 3D reconstructed models. The results that I present here lay the bases for a novel procedure that I will apply (see Chapter 7) for the reconstruction of the ovarian vasculature.

### 6.2.1. Hematoxylin and Eosin staining of ovarian sections pre-treated with Lugol's solution highlights the main vasculature and capillaries meshwork surrounding individual follicles

Interestingly, when stained with H and E, histological sections prepared from ovaries previously treated with Lugol's solution (Figure 37A) showed a remarkable variation in the colour tones compared to the expected pink/violet (Figure 37B).

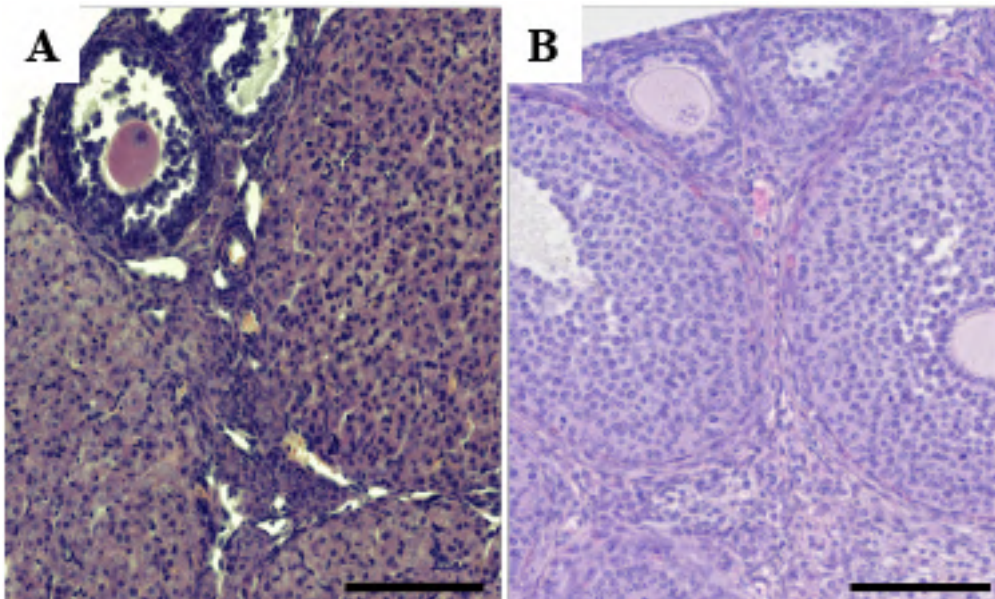


**Figure 37.** Representative ovarian sections **A)** stained with H and E after the treatment with Lugol's solution during microCT analysis, and **B)** stained with H and E. Bar, 100 µm.

In particular, this property highlighted individual red blood cells present in the tissue with an orange/brown colour, allowing an easy pinpointing of the smallest capillaries (Figure 38A, red arrowheads), including those not visible with tomography or tissue clearing. Figure 38B shows that, by using Adobe Photoshop CC 2015 Sampling function, it was possible to automatically segment all those structures within that orange/brown colour range.

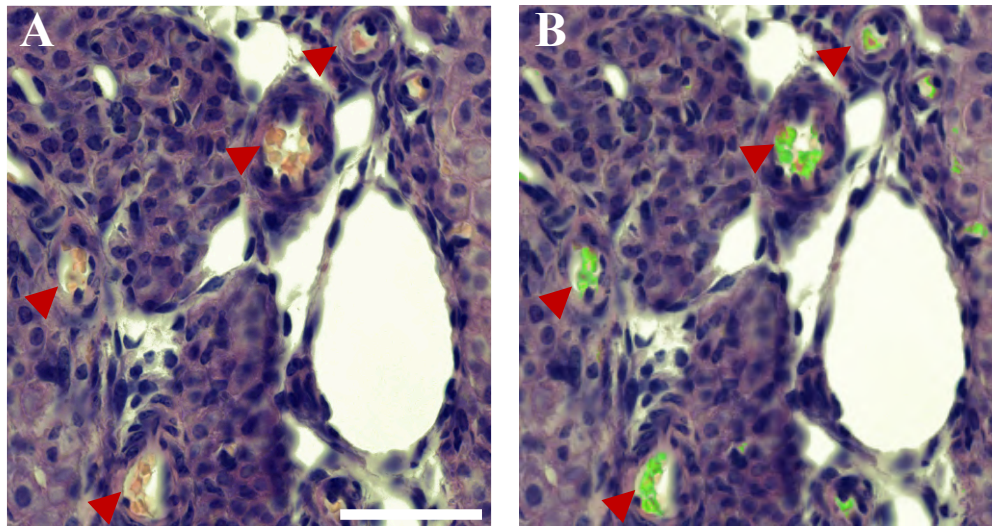


**Figure 38.** A) Portion of an ovarian section stained with H and E after Lugol's solution treatment; B) In green, automatic vessels segmentation made according to pixels RGB values. Bar, 50  $\mu\text{m}$ .

Overall, Confocal histology combines Eosin staining of 20  $\mu\text{m}$  histological sections with 3D confocal imaging for the analysis of the mouse ovary. This approach allows to define a topography of all the ovarian follicles, from T1 to T8, with extremely high resolution, and to classify the enclosed oocytes according to their chromatin organisation.

Although E is commonly used as histological stain for bright-field analysis, the usage we did as fluorophore to analyse the ovarian tissue with confocal microscopy is consistent with some previous fluorescence studies of elastic fibres [142], muscle cells [143], zymogen granules [144], meiotic spindles, basal lamina [145], mitochondria [146], as well as for biopsies histopathology [147], [148], [149].

E forms protein-dye complexes by binding to the carboxylic and phenolic groups of arginine, histidine, lysine and tryptophan protein residues [150]. Within the ovarian tissue, this property allows to identify protein-rich regions such as the nucleus and cell membranes of stromal, follicular cells and oocytes, together with the oocyte's zona pellucida and nucleolus. Particularly, the latter is well known to be responsible for the synthesis, processing and assembly of ribosomes [151] and has a pivotal role in the functional characterisation of oocytes [152], [153]. The nucleolus is composed of tandem arrays of ribosomal DNA (rDNA) located in nucleolus organiser regions (NORs) [154] and its activity is mainly coordinated by several proteins present within the fibrillar centre, the dense fibrillar component and the granular component [155], [156]. In addition, the nucleolus presents proteins involved in cell cycle regulation and cellular stress responses [157], [158].

This rich and dynamic protein content might account for the intense and wide nucleolus regions positive to E staining. The result suggests that E highlights the large number of regulative proteins that create complexes with rDNA, indirectly returning a 3D map of the chromatin organisation around the nucleus. This aspect allows us to qualitatively characterise the oocytes present in the ovary in developmentally competent oocyte (SN) or non-competent oocyte (NSN). When performed after tomographic 3D reconstruction of all the follicles present within the ovarian volume, it would help to reveal the 3D localisation of the enclosed developmentally competent and non-competent oocytes.

Future work will be done to perform co-localisation analysis of E-positive proteins with some proteins known to be abundant and nucleolar specific, e.g., fibrillarin [159], [160].

In conclusion, a further advantage of the proposed confocal histology is the possibility to acquire precious information below the specimen surface. Our method permits the confocal imaging of 20  $\mu\text{m}$ -thick section, but we are now working to increase the E penetration capacity by treating ovarian tissue with detergents. A thickness greater than 50  $\mu\text{m}$  were excluded from this analysis, since it is close to cutting limit of rotary microtomes, and it would require tissue clearing [161].

---

# Chapter 7

---

## Conclusions and future objectives

This thesis describes the results obtained during the process of building a pipeline that combines biological and engineering tools for the 3D morpho-functional analysis and reconstruction of the mouse ovary (Figure 39).

The results of this multi-step work serve as proof-of-concept and set sound bases for building a digital 3D functional Atlas of the mouse ovary, which will require a final step of merging of such various information within the precise spatial coordinates given by the *in-silico* 3D anatomical model.

# Conclusions and future objectives

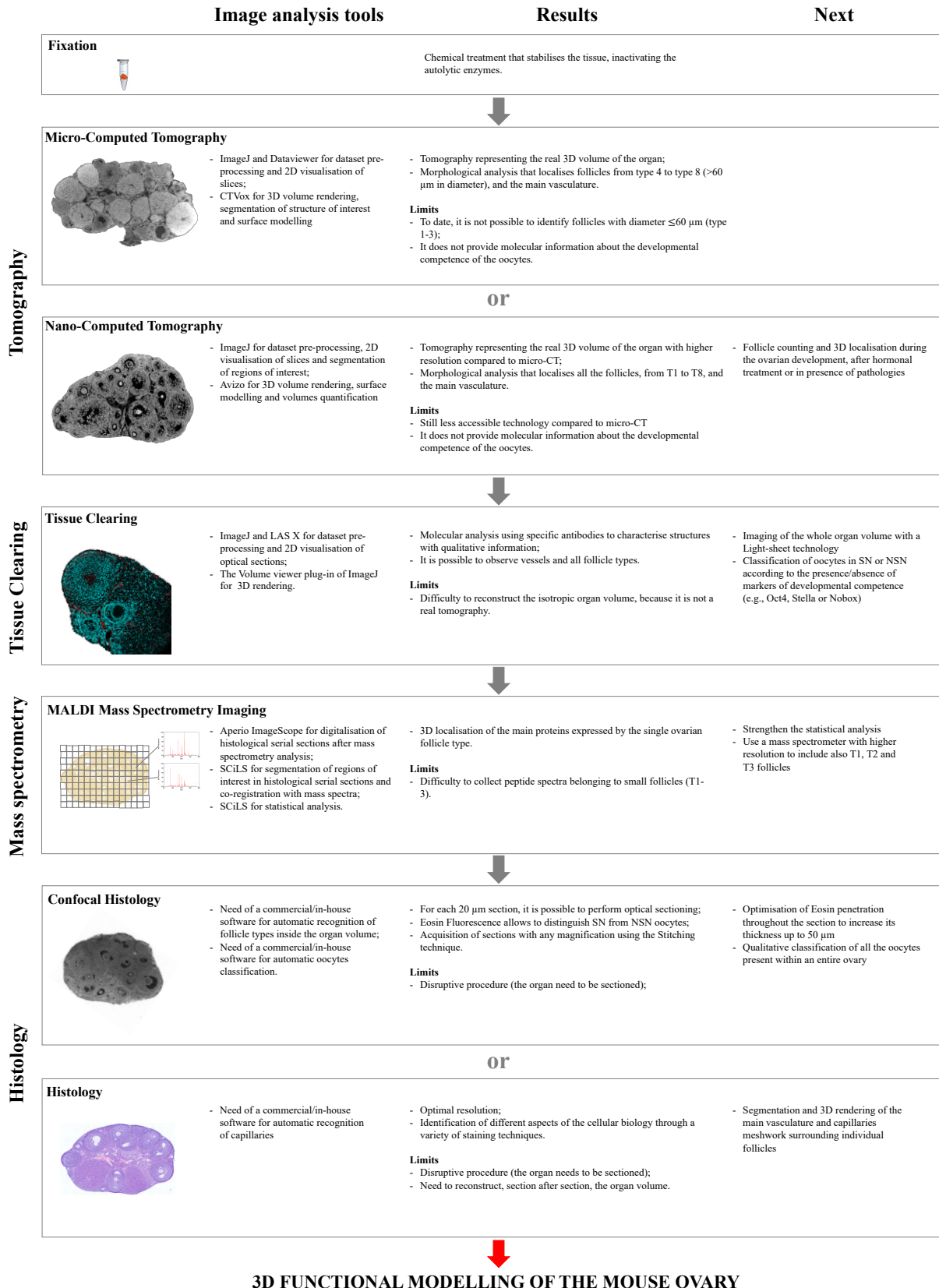


**Figure 39.** The main results and future objectives of the multi-step pipeline, whose integration of information will contribute to the functional 3D reconstruction of the mouse ovary.

In the next future, I plan to complete each of the proposed steps of analysis on individual ovaries and make them more robust. To this regard, the following will be my main objectives:

1. *NanoCT spatial analysis of follicles activated during early recruitment waves in the pre-pubertal mouse ovary, and 3D localisation of those pre-ovulatory follicles involved in the first ovulation.* These analyses aim to define the dynamics of early recruitment, to identify those ovarian regions where first recruitment and ovulation occur. This work will require the optimisation of the nanoCT analysis of the ovary during the early stages of the mouse life, from 4 to 13 days after birth, and, then, a spatial analysis similar to that used for microCT data, with follicles classification and 3D localisation in each of the eight ovarian sectors, drawn along the dorsal-ventral axis.
2. *Tissue clearing combined with 3D optical imaging of the mouse ovary to precisely localise developmentally competent oocytes.* The first question that will need to be addressed concerns with the evaluation of antibodies and dyes penetration throughout the whole organ volume by analysing the cleared ovary with light-sheet microscopy, the only technology able to allow *in toto* observation of large samples.  
Then, alongside with the morphological analysis, future work will be required to 3D map and qualitatively characterise the oocytes present in the ovary by using markers able to reveal their developmental potential (i.e., Oct4, Nobox or Stella [119], [121]).
3. *MALDI-MSI data generation and analysis.* Although the results obtained so far demonstrate the adaptability of MALDI-MSI to study the peptide content of ovarian follicles, future work will be needed to make this analysis more robust. Since PCA suggested an interesting shift in the 3D position of mass spectra during follicle growth from T5 to T8, we are now working, in collaboration with Prof. Bellazzi's group of bioengineers (University of Pavia), to define new methods for data visualisation and statistical analysis capable to bring out those peptides that most contribute to this shift.  
Also, in order to strengthen the statistical analysis, we will need to increase the number of analysed ovaries to at least five from different individuals. Then, to include also T1 – T3 follicles we plan to perform the next analyses with a 10- $\mu\text{m}$  laser pixel width mass spectrometer which should allow a more precise spectra identification, even in follicles whose diameter is in the range of 15-30  $\mu\text{m}$ .
4. *Innovative applications of confocal and classical histology.* The main advantage of the proposed Confocal histology is the possibility to visualise and classify oocytes nucleolar chromatin organisation. In the next future, we plan to employ this kind of analysis after tomographic 3D reconstruction of all the follicles present within the ovarian volume to characterise the oocytes developmental potential.

As for classical histology, the possibility to clearly distinguish structures according to their characteristic colour will be employed to automatically segment even thinner capillaries surrounding individual growing follicles to produce 3D reconstructed models of the ovarian vasculature with histological detail. To this end, we are collaborating with a group of engineers of the University of Pavia, to find the better strategies of registration and automatic capillaries segmentation to be implemented along the procedure of 3D reconstruction from serial histological sections.

*Applications.* As long-term goal, I will move to the application of the entire pipeline on the single 4% PFA-fixed mouse ovary, to have precise and coherent spatial coordinates in which integrate 3D and 2D morpho-functional data. This pipeline not only might contribute to our comprehension of folliculogenesis dynamics during the development of the organ under normal conditions, but it would be applied for the study of the changes occurring during ageing, in the presence of pathologies or after hormones or drugs administration. Furthermore, the final pipeline is intended to be tested and used also for the analysis of other mammalian ovaries in order to obtain a comparative 3D morpho-functional reconstruction of the evolutive history of the ovary, as well as for the analysis of other organs, such as the testis.

The results obtained might be used to build the Digital 3D Atlas of the mammalian ovary addressed to the scientific community, but also to design an educational tool combining a simplified digital 3D reconstruction with the support of a 3D printed hand-held models which will enable visual inspection and its direct manipulation.

---

## References

---

- [1] Kaufman M: "The Atlas of Mouse Development". 1992.
- [2] Regev A, Teichmann SA, Lander ES, Amit I, Benoist C, Birney E, et al.: "The Human Cell Atlas". *ELife* 2017;6. <https://doi.org/10.7554/eLife.27041>.
- [3] Song Y, Xu X, Wang W, Tian T, Zhu Z, Yang C: "Single cell transcriptomics: moving towards multi-omics". *The Analyst* 2019;144:3172–89. <https://doi.org/10.1039/c8an01852a>.
- [4] Rankov V, Locke RJ, Edens RJ, Barber PR, Vojnovic B: "An Algorithm for image stitching and blending". In: Conchello J-A, Cogswell CJ, Wilson T, editors., San Jose, CA: 2005, p. 190. <https://doi.org/10.1117/12.590536>.
- [5] Hofmann AP, Rätsep MT, Chen Z, Felker AM, Croy BA, Gerber SA: "Whole Mount In Situ Immunohistochemistry". In: Croy BA, Yamada AT, DeMayo FJ, Adamson SL, editors. *Guide Investig. Mouse Pregnancy*, Boston: Academic Press; 2014, p. 605–10. <https://doi.org/10.1016/B978-0-12-394445-0.00051-5>.
- [6] Richardson DS, Lichtman JW: "Clarifying Tissue Clearing". *Cell* 2015;162:246–57. <https://doi.org/10.1016/j.cell.2015.06.067>.
- [7] Richardson DS, Lichtman JW: "SnapShot: Tissue Clearing". *Cell* 2017;171:496-496.e1. <https://doi.org/10.1016/j.cell.2017.09.025>.
- [8] Grangeat P: "Introduction to Tomography". *Tomography*, John Wiley & Sons, Ltd; 2010, p. 1–20. <https://doi.org/10.1002/9780470611784.ch1>.
- [9] Ourselin S, Roche A, Prima S, Ayache N: "Block Matching: A General Framework to Improve Robustness of Rigid Registration of Medical Images". In: Delp SL, DiGoia AM, Jaramaz B, editors. *Med. Image Comput. Comput.-Assist. Interv. – MICCAI 2000*, Berlin, Heidelberg: Springer; 2000, p. 557–66. [https://doi.org/10.1007/978-3-540-40899-4\\_57](https://doi.org/10.1007/978-3-540-40899-4_57).
- [10] Davatzikos C. "Spatial transformation and registration of brain images using elastically deformable models". *Comput Vis Image Underst CVIU* 1997;66:207–22. <https://doi.org/10.1006/cviu.1997.0605>.
- [11] Aganj I, Fischl B: "Multimodal Image Registration through Simultaneous Segmentation". *IEEE Signal Process Lett* 2017;24:1661–5. <https://doi.org/10.1109/LSP.2017.2754263>.
- [12] Otsu N: "A Threshold Selection Method from Gray-Level Histograms" *IEEE Transactions on Systems, Man and Cybernetics*. 1979;9:62-66.
- [13] Sethian JA: "Level Set Methods and Fast Marching Methods". In: Sethian J, editor Cambridge, UK: Cambridge University Press; 1999.
- [14] Adams R, Bischof L: "Seeded region growing". *IEEE Trans Pattern Anal Mach Intell* 1994;16:641–7. <https://doi.org/10.1109/34.295913>.

- [15] Sahiner B, Pezeshk A, Hadjiiski LM, Wang X, Drukker K, Cha KH, et al.: "Deep learning in medical imaging and radiation therapy". *Med Phys* 2019;46:e1–36. <https://doi.org/10.1002/mp.13264>.
- [16] El Seoud MSA, Mady AS: "A Comprehensive Review on Volume Rendering Techniques". *Proc. 2019 8th Int. Conf. Softw. Inf. Eng.*, New York, NY, USA: Association for Computing Machinery; 2019, p. 126–131. <https://doi.org/10.1145/3328833.3328878>.
- [17] Lorensen WE: "History of the Marching Cubes Algorithm". *IEEE Comput Graph Appl* 2020;40:8–15. <https://doi.org/10.1109/MCG.2020.2971284>.
- [18] Lorensen WE, Cline HE: "Marching cubes: A high resolution 3D surface construction algorithm". *ACM SIGGRAPH Comput Graph* 1987;21:163–169. <https://doi.org/10.1145/37402.37422>.
- [19] Hennet ML, Combelles CMH: "The antral follicle: a microenvironment for oocyte differentiation". *Int J Dev Biol* 2012;56:819–31. <https://doi.org/10.1387/ijdb.120133cc>.
- [20] Pedersen T, Peters H: "Proposal for a classification of oocytes and follicles in the mouse ovary". *J Reprod Fertil* 1968;17:555–7. <https://doi.org/10.1530/jrf.0.0170555>.
- [21] Tajima K, Orisaka M, Mori T, Kotsuji F: "Ovarian theca cells in follicular function". *Reprod Biomed Online* 2007;15:591–609. [https://doi.org/10.1016/S1472-6483\(10\)60392-6](https://doi.org/10.1016/S1472-6483(10)60392-6).
- [22] McLaren A: "Meiosis and differentiation of mouse germ cells". *Symp Soc Exp Biol* 1984;38:7–23.
- [23] Magnúsdóttir E, Surani MA: "How to make a primordial germ cell". *Dev Camb Engl* 2014;141:245–52. <https://doi.org/10.1242/dev.098269>.
- [24] Lei L, Spradling AC: "Mouse primordial germ cells produce cysts that partially fragment prior to meiosis". *Dev Camb Engl* 2013;140:2075–81. <https://doi.org/10.1242/dev.093864>.
- [25] Byskov AG: "Differentiation of mammalian embryonic gonad". *Physiol Rev* 1986;66:71–117. <https://doi.org/10.1152/physrev.1986.66.1.71>.
- [26] McGee EA, Hsueh AJW: "Initial and Cyclic Recruitment of Ovarian Follicles". *Endocr Rev* 2000;21:200–14. <https://doi.org/10.1210/edrv.21.2.0394>.
- [27] Cecconi S, Mauro A, Cellini V, Patacchiola F: "The role of Akt signalling in the mammalian ovary". *Int J Dev Biol* 2013;56:809–17. <https://doi.org/10.1387/ijdb.120146sc>.
- [28] Kawashima I, Kawamura K: "Regulation of follicle growth through hormonal factors and mechanical cues mediated by Hippo signaling pathway". *Syst Biol Reprod Med* 2018;64:3–11. <https://doi.org/10.1080/19396368.2017.1411990>.
- [29] Shah JS, Sabouni R, Vaught KCC, Owen CM, Albertini DF, Segars JH: "Biomechanics and mechanical signaling in the ovary: a systematic review". *J Assist Reprod Genet* 2018;35:1135. <https://doi.org/10.1007/s10815-018-1180-y>.
- [30] Edson MA, Nagaraja AK, Matzuk MM: "The Mammalian Ovary from Genesis to Revelation". *Endocr Rev* 2009;30:624–712.

- <https://doi.org/10.1210/er.2009-0012>.
- [31] Hsueh AJW, Kawamura K, Cheng Y, Fauser BCJM: "Intraovarian Control of Early Folliculogenesis". *Endocr Rev* 2015;36:1. <https://doi.org/10.1210/er.2014-1020>.
- [32] Zuccotti M, Merico V, Cecconi S, Redi CA, Garagna S: "What does it take to make a developmentally competent mammalian egg?" *Hum Reprod Update* 2011;17:525–40. <https://doi.org/10.1093/humupd/dmr009>.
- [33] Zeleznik AJ: "The physiology of follicle selection". *Reprod Biol Endocrinol RBE* 2004;2:31. <https://doi.org/10.1186/1477-7827-2-31>.
- [34] Scaramuzzi RJ, Baird DT, Campbell BK, Driancourt M-A, Dupont J, Fortune JE, et al: "Regulation of folliculogenesis and the determination of ovulation rate in ruminants". *Reprod Fertil Dev* 2011;23:444–67. <https://doi.org/10.1071/RD09161>.
- [35] Kirkendoll SD, Bacha D: "Histology, Corpus Albicans". StatPearls, Treasure Island (FL): StatPearls Publishing; 2020.
- [36] Georges A, Auguste A, Bessière L, Vanet A, Todeschini A-L, Veitia RA: "FOXL2: a central transcription factor of the ovary". *J Mol Endocrinol* 2014;52:R17–33. <https://doi.org/10.1530/JME-13-0159>.
- [37] Amleh A, Dean J: "Mouse genetics provides insight into folliculogenesis, fertilization and early embryonic development". *Hum Reprod Update* 2002;8:395–403. <https://doi.org/10.1093/humupd/8.5.395>.
- [38] Depalo R, Nappi L, Loverro G, Bettocchi S, Caruso ML, Valentini AM, et al: "Evidence of apoptosis in human primordial and primary follicles". *Hum Reprod* 2003;18:2678–82. <https://doi.org/10.1093/humrep/deg507>.
- [39] Garagna S, Merico V, Sebastiano V, Monti M, Orlandini G, Gatti R, et al: "Three-dimensional localization and dynamics of centromeres in mouse oocytes during folliculogenesis". *J Mol Histol* 2004;35:631–8. <https://doi.org/10.1007/s10735-004-2190-x>.
- [40] Zuccotti M, Giorgi Rossi P, Martinez A, Garagna S, Forabosco A, Redi CA: "Meiotic and Developmental Competence of Mouse Antral Oocytes". *Biol Reprod* 1998;58:700–4. <https://doi.org/10.1095/biolreprod58.3.700>.
- [41] Zuccotti M, Ponce RH, Boiani M, Guizzardi S, Govoni P, Scandroglio R, et al: "The analysis of chromatin organisation allows selection of mouse antral oocytes competent for development to blastocyst". *Zygote Camb Engl* 2002;10:73–8. <https://doi.org/10.1017/s0967199402002101>.
- [42] Inoue A, Nakajima R, Nagata M, Aoki F: "Contribution of the oocyte nucleus and cytoplasm to the determination of meiotic and developmental competence in mice". *Hum Reprod* 2008;23:1377–84. <https://doi.org/10.1093/humrep/den096>.
- [43] Redmer DA, Reynolds LP: "Angiogenesis in the ovary". *Rev Reprod* 1996;1:182–92. <https://doi.org/10.1530/ror.0.0010182>.
- [44] Kosaka N, Sudo N, Miyamoto A, Shimizu T: "Vascular endothelial growth factor (VEGF) suppresses ovarian granulosa cell apoptosis in vitro". *Biochem Biophys Res Commun* 2007;363:733–7. <https://doi.org/10.1016/j.bbrc.2007.09.061>.

- [45] Barboni B, Turriani M, Galeati G, Spinaci M, Bacci ML, Forni M, et al.: "Vascular Endothelial Growth Factor Production in Growing Pig Antral Follicles". *Biol Reprod* 2000;63:858–64. <https://doi.org/10.1095/biolreprod63.3.858>.
- [46] Greenwald GS: "Temporal and Topographic Changes in DNA Synthesis after Induced Follicular Atresia". *Biol Reprod* 1989;41:175–81. <https://doi.org/10.1095/biolreprod41.1.175>.
- [47] Fraser HM: "Regulation of the ovarian follicular vasculature". *Reprod Biol Endocrinol* 2006;4:18. <https://doi.org/10.1186/1477-7827-4-18>.
- [48] Lugano R, Ramachandran M, Dimberg A: "Tumor angiogenesis: causes, consequences, challenges and opportunities". *Cell Mol Life Sci* 2020;77:1745–70. <https://doi.org/10.1007/s00018-019-03351-7>.
- [49] Fraser HM, Duncan WC: "Vascular morphogenesis in the primate ovary". *Angiogenesis* 2005;8:101–16. <https://doi.org/10.1007/s10456-005-9004-y>.
- [50] Xie Q, Cheng Z, Chen X, Lobe CG, Liu J: "The role of Notch signalling in ovarian angiogenesis". *J Ovarian Res* 2017;10. <https://doi.org/10.1186/s13048-017-0308-5>.
- [51] Martelli A, Berardinelli P, Russo V, Mauro A, Bernabò N, Gioia L, et al.: "Spatio-temporal analysis of vascular endothelial growth factor expression and blood vessel remodelling in pig ovarian follicles during the periovulatory period". *J Mol Endocrinol* 2006;36:107–19. <https://doi.org/10.1677/jme.1.01921>.
- [52] Mauro A, Martelli A, Berardinelli P, Russo V, Bernabò N, Di Giacinto O, et al.: "Effect of Antiprogestosterone RU486 on VEGF Expression and Blood Vessel Remodeling on Ovarian Follicles before Ovulation". *PLoS ONE* 2014;9. <https://doi.org/10.1371/journal.pone.0095910>.
- [53] Ko C, Gieske MC, Al-Alem L, Hahn Y, Su W, Gong MC, et al.: "Endothelin-2 in Ovarian Follicle Rupture". *Endocrinology* 2006;147:1770–9. <https://doi.org/10.1210/en.2005-1228>.
- [54] Berisha B, Schams D, Rodler D, Pfaffl MW: "Angiogenesis in The Ovary - The Most Important Regulatory Event for Follicle and Corpus Luteum Development and Function in Cow - An Overview". *Anat Histol Embryol* 2016;45:124–30. <https://doi.org/10.1111/ahe.12180>.
- [55] Lu E, Li C, Wang J, Zhang C: "Inflammation and angiogenesis in the corpus luteum". *J Obstet Gynaecol Res* 2019;45:1967–74. <https://doi.org/10.1111/jog.14076>.
- [56] Brown HM, Russell DL: "Blood and lymphatic vasculature in the ovary: development, function and disease". *Hum Reprod Update* 2014;20:29–39. <https://doi.org/10.1093/humupd/dmt049>.
- [57] Devesa J, Caicedo D: "The Role of Growth Hormone on Ovarian Functioning and Ovarian Angiogenesis". *Front Endocrinol* 2019;10:450. <https://doi.org/10.3389/fendo.2019.00450>.
- [58] Sun H, Gong T-T, Jiang Y-T, Zhang S, Zhao Y-H, Wu Q-J: "Global, regional, and national prevalence and disability-adjusted life-years for infertility in 195 countries and territories, 1990-2017: results from a global burden of disease study, 2017". *Aging* 2019;11:10952–91.

- <https://doi.org/10.18632/aging.102497>.
- [59] Belli M, Vigone G, Merico V, Redi CA, Zuccotti M, Garagna S: "Towards a 3D culture of mouse ovarian follicles". *Int J Dev Biol* 2012;56:931–7. <https://doi.org/10.1387/ijdb.120175mz>.
- [60] Telfer EE: "Future developments: In vitro growth (IVG) of human ovarian follicles". *Acta Obstet Gynecol Scand* 2019;98:653–8. <https://doi.org/10.1111/aogs.13592>.
- [61] Robinson RS, Woad KJ, Hammond AJ, Laird M, Hunter MG, Mann GE: "Angiogenesis and vascular function in the ovary". *Reprod Camb Engl* 2009;138:869–81. <https://doi.org/10.1530/REP-09-0283>.
- [62] Zhang J, Zhang J, Gao B, Xu Y, Liu H, Pan Z: "Detection of the effects and potential interactions of FSH, VEGFA, and 2-methoxyestradiol in follicular angiogenesis, growth, and atresia in mouse ovaries". *Mol Reprod Dev* 2019;86:566–75. <https://doi.org/10.1002/mrd.23133>.
- [63] Russell DL, Gilchrist RB, Brown HM, Thompson JG: "Bidirectional communication between cumulus cells and the oocyte: Old hands and new players?" *Theriogenology* 2016;86:62–8. <https://doi.org/10.1016/j.theriogenology.2016.04.019>.
- [64] Cordeiro MH, Kim S-Y, Ebbert K, Duncan FE, Ramalho-Santos J, Woodruff TK: "Geography of follicle formation in the embryonic mouse ovary impacts activation pattern during the first wave of folliculogenesis". *Biol Reprod* 2015;93:88. <https://doi.org/10.1095/biolreprod.115.131227>.
- [65] Faire M, Skillern A, Arora R, Nguyen DH, Wang J, Chamberlain C, et al.: "Follicle dynamics and global organization in the intact mouse ovary". *Dev Biol* 2015;403:69–79. <https://doi.org/10.1016/j.ydbio.2015.04.006>.
- [66] Malki S, Tharp ME, Bortvin A: "A Whole-Mount Approach for Accurate Quantitative and Spatial Assessment of Fetal Oocyte Dynamics in Mice". *Biol Reprod* 2015;93:113. <https://doi.org/10.1095/biolreprod.115.132118>.
- [67] Feng Y, Cui P, Lu X, Hsueh B, Möller Billig F, Zarnescu Yanez L, et al.: "CLARITY reveals dynamics of ovarian follicular architecture and vasculature in three-dimensions". *Sci Rep* 2017;7:44810. <https://doi.org/10.1038/srep44810>.
- [68] Kagami K, Shinmyo Y, Ono M, Kawasaki H, Fujiwara H: "Three-dimensional evaluation of murine ovarian follicles using a modified CUBIC tissue clearing method". *Reprod Biol Endocrinol RBE* 2018;16:72. <https://doi.org/10.1186/s12958-018-0381-7>.
- [69] Oren R, Fellus-Alyagor L, Addadi Y, Bochner F, Gutman H, Blumenreich S, et al: "Whole Organ Blood and Lymphatic Vessels Imaging (WOBLI)". *Sci Rep* 2018;8:1412. <https://doi.org/10.1038/s41598-018-19663-w>.
- [70] Chung K, Wallace J, Kim S-Y, Kalyanasundaram S, Andalman AS, Davidson TJ, et al: "Structural and molecular interrogation of intact biological systems". *Nature* 2013;497:332–7. <https://doi.org/10.1038/nature12107>.
- [71] Schermelleh L, Heintzmann R, Leonhardt H: "A guide to super-resolution fluorescence microscopy". *J Cell Biol* 2010;190:165–75. <https://doi.org/10.1083/jcb.201002018>.

- [72] Cremer C, Szczurek A, Schock F, Gourram A, Birk U. "Super-resolution microscopy approaches to nuclear nanostructure imaging". *Methods* 2017;123. <https://doi.org/10.1016/j.ymeth.2017.03.019>.
- [73] Mircea CN, Lujan ME, Jaiswal RS, Singh J, Adams GP, Pierson RA: "Ovarian imaging in the mouse using ultrasound biomicroscopy (UBM): a validation study". *Reprod Fertil Dev* 2009;21:579–86. <https://doi.org/10.1071/RD08295>.
- [74] Ginther OJ, Rakesh HB, Hoffman MM: "Complex interrelationships among CL, pre-ovulatory follicle, number of follicular waves, and right or left ovaries in heifers". *Theriogenology* 2014;81:481–9. <https://doi.org/10.1016/j.theriogenology.2013.11.003>.
- [75] Migone FF, Cowan RG, Williams RM, Gorse KJ, Zipfel WR, Quirk SM: "In vivo imaging reveals an essential role of vasoconstriction in rupture of the ovarian follicle at ovulation". *Proc Natl Acad Sci U S A* 2016;113:2294–9. <https://doi.org/10.1073/pnas.1512304113>.
- [76] Hensley H, Quinn BA, Wolf RL, Litwin SL, Mabuchi S, Williams SJ, et al.: "Magnetic resonance imaging for detection and determination of tumor volume in a genetically engineered mouse model of ovarian cancer". *Cancer Biol Ther* 2007;6:1717–25. <https://doi.org/10.4161/cbt.6.11.4830>.
- [77] Paulini F, Chaves SB, Rôlo JLJP, Azevedo RBD, Lucci CM: "Evaluation of ovarian structures using computerized microtomography". *An Acad Bras Cienc* 2017;89:2131–9. <https://doi.org/10.1590/0001-3765201720150864>.
- [78] Pascolo L, Sena G, Gianoncelli A, Cernogoraz A, Kourousias G, Metscher BD, et al.: "Hard and soft X-ray imaging to resolve human ovarian cortical structures". *J Synchrotron Radiat* 2019;26:1322–9. <https://doi.org/10.1107/S1600577519003680>.
- [79] Kim J, Choi YH, Chang S, Kim K-T, Je JH: "Defective folliculogenesis in female mice lacking Vaccinia-related kinase 1". *Sci Rep* 2012;2:468. <https://doi.org/10.1038/srep00468>.
- [80] Thavarajah R, Mudimbaimannar VK, Elizabeth J, Rao UK, Ranganathan K: "Chemical and physical basics of routine formaldehyde fixation". *J Oral Maxillofac Pathol JOMFP* 2012;16:400–5. <https://doi.org/10.4103/0973-029X.102496>.
- [81] Ritman EL: "Micro-Computed Tomography—Current Status and Developments". *Annu Rev Biomed Eng* 2004;6:185–208. <https://doi.org/10.1146/annurev.bioeng.6.040803.140130>.
- [82] Mussmann B, Overgaard S, Torfing T, Traise P, Gerke O, Andersen PE: "Agreement and precision of periprosthetic bone density measurements in micro-CT, single and dual energy CT". *J Orthop Res* 2017;35:1470–7. <https://doi.org/10.1002/jor.23417>.
- [83] Song Y, Zhu F, Lin F, Zhang F, Zhang S: "Bone quality, and the combination and penetration of cement–bone interface: A comparative micro-CT study of osteoarthritis and rheumatoid arthritis". *Medicine (Baltimore)* 2018;97:e11987. <https://doi.org/10.1097/MD.00000000000011987>.

- [84] Chałas R, Szlązak K, Wójcik-Chęcińska I, Jaroszewicz J, Molak R, Czechowicz K, et al.: "Observations of mineralised tissues of teeth in X-ray micro-computed tomography". *Folia Morphol* 2017;76:143–8. <https://doi.org/10.5603/FM.a2016.0070>.
- [85] Batool F, Strub M, Petit C, Bugueno IM, Bornert F, Clauss F, et al.: "Periodontal Tissues, Maxillary Jaw Bone, and Tooth Regeneration Approaches: From Animal Models Analyses to Clinical Applications". *Nanomaterials* 2018;8:337. <https://doi.org/10.3390/nano8050337>.
- [86] Velozo C, Albuquerque D: "Microcomputed Tomography Studies of the Effectiveness of XP-endo Shaper in Root Canal Preparation: A Review of the Literature". *Sci World J* 2019;2019:e3570870. <https://doi.org/10.1155/2019/3570870>.
- [87] Metscher BD: "MicroCT for comparative morphology: simple staining methods allow high-contrast 3D imaging of diverse non-mineralized animal tissues". *BMC Physiol* 2009;9:11. <https://doi.org/10.1186/1472-6793-9-11>.
- [88] Pauwels E, Loo DV, Cornillie P, Brabant L, Hoorebeke LV: "An exploratory study of contrast agents for soft tissue visualization by means of high resolution X-ray computed tomography imaging". *J Microsc* 2013;250:21–31. <https://doi.org/10.1111/jmi.12013>.
- [89] Silva JM de S e, Zanette I, Noël PB, Cardoso MB, Kimm MA, Pfeiffer F: "Three-dimensional non-destructive soft-tissue visualization with X-ray staining micro-tomography". *Sci Rep* 2015;5:14088. <https://doi.org/10.1038/srep14088>.
- [90] de Bournonville S, Vangrunderbeeck S, Kerckhofs G: "Contrast-Enhanced MicroCT for Virtual 3D Anatomical Pathology of Biological Tissues: A Literature Review". *Contrast Media X26 Mol Imaging* 2019;2019:e8617406. <https://doi.org/10.1155/2019/8617406>.
- [91] Kampschulte M, Langheinirch AC, Sender J, Litzlbauer HD, Althöhn U, Schwab JD, et al.: "Nano-Computed Tomography: Technique and Applications". *ROFO Fortschr Geb Rontgenstr Nuklearmed* 2016;188:146–54. <https://doi.org/10.1055/s-0041-106541>.
- [92] Lim C, Yan B, Yin L, Zhu L: "Simulation of diffusion-induced stress using reconstructed electrodes particle structures generated by micro/nano-CT". *Electrochimica Acta* 2012;75:279–87. <https://doi.org/10.1016/j.electacta.2012.04.120>.
- [93] Wagner R, Loo DV, Hossler F, Czymmek K, Pauwels E, Hoorebeke LV: "High-Resolution Imaging of Kidney Vascular Corrosion Casts with Nano-CT". *Microsc Microanal* 2011;17:215–9. <https://doi.org/10.1017/S1431927610094201>.
- [94] Mizutani R, Saiga R, Takeuchi A, Uesugi K, Terada Y, Suzuki Y, et al.: "Three-dimensional alteration of neurites in schizophrenia". *Transl Psychiatry* 2019;9:85. <https://doi.org/10.1038/s41398-019-0427-4>.
- [95] Busse M, Müller M, Kimm MA, Ferstl S, Allner S, Achterhold K, et al.: "Three-dimensional virtual histology enabled through cytoplasm-specific X-ray stain for microscopic and nanoscopic computed tomography". *Proc Natl Acad Sci* 2018;115:2293–8.

- <https://doi.org/10.1073/pnas.1720862115>.
- [96] Renier N, Wu Z, Simon DJ, Yang J, Ariel P, Tessier-Lavigne M: "iDISCO: a simple, rapid method to immunolabel large tissue samples for volume imaging". *Cell* 2014;159:896–910. <https://doi.org/10.1016/j.cell.2014.10.010>.
- [97] Lagarrigue M, Lavigne R, Guével B, Com E, Chaurand P, Pineau C: "Matrix-Assisted Laser Desorption/Ionization Imaging Mass Spectrometry: A Promising Technique for Reproductive Research". *Biol Reprod* 2012;86. <https://doi.org/10.1095/biolreprod.111.094896>.
- [98] Ly A, Buck A, Balluff B, Sun N, Gorzolka K, Feuchtinger A, et al.: "High-mass-resolution MALDI mass spectrometry imaging of metabolites from formalin-fixed paraffin-embedded tissue". *Nat Protoc* 2016;11:1428–43. <https://doi.org/10.1038/nprot.2016.081>.
- [99] Lagarrigue M, Becker M, Lavigne R, Deininger S-O, Walch A, Aubry F, et al.: "Revisiting rat spermatogenesis with MALDI imaging at 20-microm resolution". *Mol Cell Proteomics MCP* 2011;10:M110.005991. <https://doi.org/10.1074/mcp.M110.005991>.
- [100] Neagu A-N: "Proteome Imaging: From Classic to Modern Mass Spectrometry-Based Molecular Histology". *Adv Exp Med Biol* 2019;1140:55–98. [https://doi.org/10.1007/978-3-030-15950-4\\_4](https://doi.org/10.1007/978-3-030-15950-4_4).
- [101] Veuthey T, Herrera G, Doderio VI: "Dyes and stains: from molecular structure to histological application". *Front Biosci Landmark Ed* 2014;19:91–112. <https://doi.org/10.2741/4197>.
- [102] Alturkistani HA, Tashkandi FM, Mohammedsaleh ZM: "Histological Stains: A Literature Review and Case Study". *Glob J Health Sci* 2015;8:72–9. <https://doi.org/10.5539/gjhs.v8n3p72>.
- [103] Fiorentino G, Parrilli A, Garagna S, Zuccotti M: "Three-Dimensional Micro-Computed Tomography of the Adult Mouse Ovary". *Front Cell Dev Biol* 2020;8:566152. <https://doi.org/10.3389/fcell.2020.566152>.
- [104] Peters H: "The development of the mouse ovary from birth to maturity". *Acta Endocrinol (Copenh)* 1969;62:98–116. <https://doi.org/10.1530/acta.0.0620098>.
- [105] Feng Y, Tamadon A, Hsueh AJW: "Imaging the ovary". *Reprod Biomed Online* 2018;36:584–93. <https://doi.org/10.1016/j.rbmo.2018.02.006>.
- [106] McKey J, Cameron LA, Lewis D, Batchvarov IS, Capel B: "Combined iDISCO and CUBIC tissue clearing and lightsheet microscopy for in toto analysis of the adult mouse ovary". *Biol Reprod* 2020;102:1080–9. <https://doi.org/10.1093/biolre/iaaa012>.
- [107] Charleston JS, Hansen KR, Thyer AC, Charleston LB, Gougeon A, Siebert JR, et al.: "Estimating human ovarian non-growing follicle number: the application of modern stereology techniques to an old problem". *Hum Reprod* 2007;22:2103–10. <https://doi.org/10.1093/humrep/dem137>.
- [108] Hedreen JC: "What was wrong with the Abercrombie and empirical cell counting methods? A review". *Anat Rec* 1998;250:373–80. [https://doi.org/10.1002/\(SICI\)1097-0185\(199803\)250:3<373::AID-AR12>3.0.CO;2-L](https://doi.org/10.1002/(SICI)1097-0185(199803)250:3<373::AID-AR12>3.0.CO;2-L).

- [109] Myers M, Britt KL, Wreford NGM, Ebling FJP, Kerr JB: "Methods for quantifying follicular numbers within the mouse ovary". *Reprod Camb Engl* 2004;127:569–80. <https://doi.org/10.1530/rep.1.00095>.
- [110] Longo F, Garagna S, Merico V, Orlandini G, Gatti R, Scandroglio R, et al.: "Nuclear localization of NORs and centromeres in mouse oocytes during folliculogenesis". *Mol Reprod Dev* 2003;66:279–90. <https://doi.org/10.1002/mrd.10354>.
- [111] Hornick JE, Duncan FE, Shea LD, Woodruff TK: "Isolated primate primordial follicles require a rigid physical environment to survive and grow in vitro". *Hum Reprod Oxf Engl* 2012;27:1801–10. <https://doi.org/10.1093/humrep/der468>.
- [112] Seibert JA: "Flat-panel detectors: how much better are they?". *Pediatr Radiol* 2006;36 Suppl 2:173–81. <https://doi.org/10.1007/s00247-006-0208-0>.
- [113] Litscher ES, Wassarman PM: "Zona Pellucida Proteins, Fibrils, and Matrix". *Annu Rev Biochem* 2020;89:695–715. <https://doi.org/10.1146/annurev-biochem-011520-105310>.
- [114] Duffy DM, Ko C, Jo M, Brannstrom M, Curry TE: "Ovulation: Parallels With Inflammatory Processes". *Endocr Rev* 2019;40:369–416. <https://doi.org/10.1210/er.2018-00075>.
- [115] Heintzmann R, Ficz G: "Breaking the resolution limit in light microscopy". *Brief Funct Genomics* 2006;5:289–301. <https://doi.org/10.1093/bfpg/ell036>.
- [116] Costa EC, Silva DN, Moreira AF, Correia IJ: "Optical clearing methods: An overview of the techniques used for the imaging of 3D spheroids". *Biotechnol Bioeng* 2019;116:2742–63. <https://doi.org/10.1002/bit.27105>.
- [117] Ma T, Cui P, Tong X, Hu W, Shao LR, Zhang F, et al.: "Endogenous Ovarian Angiogenesis in Polycystic Ovary Syndrome-Like Rats Induced by Low-Frequency Electro-Acupuncture: The CLARITY Three-Dimensional Approach". *Int J Mol Sci* 2018;19. <https://doi.org/10.3390/ijms19113500>.
- [118] Chakraborty T, Driscoll MK, Jeffery E, Murphy MM, Roudot P, Chang B-J, et al.: "Light-sheet microscopy of cleared tissues with isotropic, subcellular resolution". *Nat Methods* 2019;16:1109–13. <https://doi.org/10.1038/s41592-019-0615-4>.
- [119] Susaki EA, Tainaka K, Perrin D, Kishino F, Tawara T, Watanabe TM, et al.: "Whole-Brain Imaging with Single-Cell Resolution Using Chemical Cocktails and Computational Analysis". *Cell* 2014;157:726–39. <https://doi.org/10.1016/j.cell.2014.03.042>.
- [120] Zuccotti M, Merico V, Sacchi L, Bellone M, Brink TC, Stefanelli M, et al.: "Oct-4 regulates the expression of Stella and Foxj2 at the Nanog locus: implications for the developmental competence of mouse oocytes". *Hum Reprod Oxf Engl* 2009;24:2225–37. <https://doi.org/10.1093/humrep/dep191>.
- [121] Zuccotti M, Merico V, Belli M, Mulas F, Sacchi L, Zupan B, et al.: "OCT4 and the acquisition of oocyte developmental competence during folliculogenesis". *Int J Dev Biol* 2012;56:853–8.

- <https://doi.org/10.1387/ijdb.120174mz>.
- [122] Belli M, Cimadomo D, Merico V, Redi CA, Garagna S, Zuccotti M: "The NOBOX protein becomes undetectable in developmentally competent antral and ovulated oocytes". *Int J Dev Biol* 2013;57:35–9. <https://doi.org/10.1387/ijdb.120125mz>.
- [123] Kim K-H, Lee K-A: "Maternal effect genes: Findings and effects on mouse embryo development". *Clin Exp Reprod Med* 2014;41:47–61. <https://doi.org/10.5653/cerm.2014.41.2.47>.
- [124] Zheng P, Dean J: "Oocyte-Specific Genes Affect Folliculogenesis, Fertilization, and Early Development". *Semin Reprod Med* 2007;25:243–51. <https://doi.org/10.1055/s-2007-980218>.
- [125] Zheng P, Dean J: "Role of Filia, a maternal effect gene, in maintaining euploidy during cleavage-stage mouse embryogenesis". *Proc Natl Acad Sci U S A* 2009;106:7473–8. <https://doi.org/10.1073/pnas.0900519106>.
- [126] Canosa S, Adriaenssens T, Coucke W, Dalmaso P, Revelli A, Benedetto C, et al.: "Zona pellucida gene mRNA expression in human oocytes is related to oocyte maturity, zona inner layer retardance and fertilization competence". *Mol Hum Reprod* 2017;23:292–303. <https://doi.org/10.1093/molehr/gax008>.
- [127] Wassarman PM, Litscher ES: "The Mouse Egg's Zona Pellucida". *Curr Top Dev Biol* 2018;130:331–56. <https://doi.org/10.1016/bs.ctdb.2018.01.003>.
- [128] De S, Marcinkiewicz JL, Vijayaraghavan S, Kline D: "Expression of 14-3-3 protein isoforms in mouse oocytes, eggs and ovarian follicular development". *BMC Res Notes* 2012;5:57. <https://doi.org/10.1186/1756-0500-5-57>.
- [129] Eisa AA, De S, Detwiler A, Gilker E, Ignatious AC, Vijayaraghavan S, et al.: "YWHA (14-3-3) protein isoforms and their interactions with CDC25B phosphatase in mouse oogenesis and oocyte maturation". *BMC Dev Biol* 2019;19:20. <https://doi.org/10.1186/s12861-019-0200-1>.
- [130] Cox L, Vanderwall DK, Parkinson KC, Sweat A, Isom SC: "Expression profiles of select genes in cumulus-oocyte complexes from young and aged mares". *Reprod Fertil Dev* 2015;27:914–24. <https://doi.org/10.1071/RD14446>.
- [131] Shozu M, Minami N, Yokoyama H, Inoue M, Kurihara H, Matsushima K, et al.: "ADAMTS-1 is involved in normal follicular development, ovulatory process and organization of the medullary vascular network in the ovary". *J Mol Endocrinol* n.d.;35:343–55. <https://doi.org/10.1677/jme.1.01735>.
- [132] Brown HM, Dunning KR, Robker RL, Boerboom D, Pritchard M, Lane M, et al.: "ADAMTS1 cleavage of versican mediates essential structural remodeling of the ovarian follicle and cumulus-oocyte matrix during ovulation in mice". *Biol Reprod* 2010;83:549–57. <https://doi.org/10.1095/biolreprod.110.084434>.
- [133] Özler S, Öztaş E, Tokmak A, Ergin M, Kuru Pekcan M, Gümüş Güler B, et al.: "Role of Versican and ADAMTS-1 in Polycystic Ovary Syndrome". *J Clin Res Pediatr Endocrinol* 2017;9:24–30.

- <https://doi.org/10.4274/jcrpe.3414>.
- [134] Berkholtz CB, Shea LD, Woodruff TK: "Extracellular matrix functions in follicle maturation". *Semin Reprod Med* 2006;24:262–9. <https://doi.org/10.1055/s-2006-948555>.
- [135] Yao Y: "Laminin: loss-of-function studies". *Cell Mol Life Sci CMLS* 2017;74:1095–115. <https://doi.org/10.1007/s00018-016-2381-0>.
- [136] Tsutsumi M, Fujiwara R, Nishizawa H, Ito M, Kogo H, Inagaki H, et al.: "Age-Related Decrease of Meiotic Cohesins in Human Oocytes". *PLOS ONE* 2014;9:e96710. <https://doi.org/10.1371/journal.pone.0096710>.
- [137] Fulka H, Langerova A: "The maternal nucleolus plays a key role in centromere satellite maintenance during the oocyte to embryo transition". *Dev Camb Engl* 2014;141:1694–704. <https://doi.org/10.1242/dev.105940>.
- [138] Terzaghi L, Luciano AM, Dall'Acqua PC, Modina SC, Peluso JJ, Lodde V: "PGRMC1 localization and putative function in the nucleolus of bovine granulosa cells and oocytes". *Reprod Camb Engl* 2018;155:273–82. <https://doi.org/10.1530/REP-17-0534>.
- [139] Bavle RM: "Eosinophilic nucleoli". *J Oral Maxillofac Pathol JOMFP* 2014;18:152–4. <https://doi.org/10.4103/0973-029X.140716>.
- [140] Hasani E, Tartara L, Tomaselli A: "A novel technique for the measurement of twophoton absorption spectra of dyes for nonlinear fluorescence microscopy". 2019 IEEE Int. Conf. BioPhotonics BioPhotonics, 2019, p. 1–3. <https://doi.org/10.1109/ICB47650.2019.8976316>.
- [141] Michálek J, Čapek M, Kubínová L: "Compensation of inhomogeneous fluorescence signal distribution in 2D images acquired by confocal microscopy". *Microsc Res Tech* 2011;74:831–8. <https://doi.org/10.1002/jemt.20965>.
- [142] de Carvalho HF, Taboga SR: "Fluorescence and confocal laser scanning microscopy imaging of elastic fibers in hematoxylin-eosin stained sections". *Histochem Cell Biol* 1996;106:587–92. <https://doi.org/10.1007/BF02473274>.
- [143] Capani F, Deerinck TJ, Ellisman MH, Bushong E, Bobik M, Martone ME: "Phalloidin-eosin followed by photo-oxidation: a novel method for localizing F-actin at the light and electron microscopic levels". *J Histochem Cytochem Off J Histochem Soc* 2001;49:1351–61. <https://doi.org/10.1177/002215540104901103>.
- [144] Wu Y, Li B, Gao XM: "Selective fluorescence of zymogen granules of pancreatic acinar cells stained with hematoxylin and eosin". *Biotech Histochem Off Publ Biol Stain Comm* 2002;77:291–3. <https://doi.org/10.1080/bih.77.5-6.291.293>.
- [145] Espada J, Valverde P, Stockert JC: "Selective fluorescence of eosinophilic structures in grasshopper and mammalian testis stained with haematoxylin-eosin". *Histochemistry* 1993;99:385–90. <https://doi.org/10.1007/BF00717051>.
- [146] Rashid F, Horobin RW: "Accumulation of fluorescent non-cationic probes in mitochondria of cultured cells: observations, a proposed

- mechanism, and some implications". *J Microsc* 1991;163:233–41. <https://doi.org/10.1111/j.1365-2818.1991.tb03175.x>.
- [147] Ali H, Ali S, Mazhar M, Ali A, Jahan A, Ali A: "Eosin fluorescence: A diagnostic tool for quantification of liver injury". *Photodiagnosis Photodyn Ther* 2017;19:37–44. <https://doi.org/10.1016/j.pdpdt.2017.03.016>.
- [148] Luo T, Lu Y, Liu S, Lin D, Qu J: "Enhanced Visualization of Hematoxylin and Eosin Stained Pathological Characteristics by Phasor Approach". *Anal Chem* 2017;89:9224–31. <https://doi.org/10.1021/acs.analchem.7b01999>.
- [149] Castellanos MR, Nehru VM, Pirog EC, Optiz L: "Fluorescence microscopy of H&E stained cervical biopsies to assist the diagnosis and grading of CIN". *Pathol Res Pract* 2018;214:605–11. <https://doi.org/10.1016/j.prp.2018.03.021>.
- [150] Waheed AA, Rao KS, Gupta PD: "Mechanism of dye binding in the protein assay using eosin dyes". *Anal Biochem* 2000;287:73–9. <https://doi.org/10.1006/abio.2000.4793>.
- [151] Schöfer C, Weipoltshammer K: "Nucleolus and chromatin". *Histochem Cell Biol* 2018;150:209–25. <https://doi.org/10.1007/s00418-018-1696-3>.
- [152] Zuccotti M, Garagna S, Merico V, Monti M, Alberto Redi C: "Chromatin organisation and nuclear architecture in growing mouse oocytes". *Mol Cell Endocrinol* 2005;234:11–7. <https://doi.org/10.1016/j.mce.2004.08.014>.
- [153] Bogolyubova I, Bogolyubov D: "Heterochromatin Morphodynamics in Late Oogenesis and Early Embryogenesis of Mammals". *Cells* 2020;9:1497. <https://doi.org/10.3390/cells9061497>.
- [154] McStay B: "Nucleolar organizer regions: genomic “dark matter” requiring illumination". *Genes Dev* 2016;30:1598–610. <https://doi.org/10.1101/gad.283838.116>.
- [155] Boisvert F-M, van Koningsbruggen S, Navascués J, Lamond AI: "The multifunctional nucleolus". *Nat Rev Mol Cell Biol* 2007;8:574–85. <https://doi.org/10.1038/nrm2184>.
- [156] Hernandez-Verdun D, Roussel P, Thiry M, Sirri V, Lafontaine DLJ: "The nucleolus: structure/function relationship in RNA metabolism". *Wiley Interdiscip Rev RNA* 2010;1:415–31. <https://doi.org/10.1002/wrna.39>.
- [157] Boulon S, Westman BJ, Hutten S, Boisvert F-M, Lamond AI: "The nucleolus under stress". *Mol Cell* 2010;40:216–27. <https://doi.org/10.1016/j.molcel.2010.09.024>.
- [158] Tiku V, Jain C, Raz Y, Nakamura S, Heestand B, Liu W, et al: "Small nucleoli are a cellular hallmark of longevity". *Nat Commun* 2017;8:16083. <https://doi.org/10.1038/ncomms16083>.
- [159] Ochs RL, Lischwe MA, Spohn WH, Busch H: "Fibrillarin: a new protein of the nucleolus identified by autoimmune sera". *Biol Cell* 1985;54:123–33. <https://doi.org/10.1111/j.1768-322X.1985.tb00387.x>.
- [160] Amin MA, Matsunaga S, Ma N, Takata H, Yokoyama M, Uchiyama S, et al.: "Fibrillarin, a nucleolar protein, is required for normal nuclear morphology and cellular growth in HeLa cells". *Biochem Biophys Res*

- Commun 2007;360:320–6. <https://doi.org/10.1016/j.bbrc.2007.06.092>.
- [161] Muntifering M, Castranova D, Gibson GA, Meyer E, Kofron M, Watson AM: "Clearing for Deep Tissue Imaging". *Curr Protoc Cytom* 2018;86:e38. <https://doi.org/10.1002/cpcy.38>.



---

# Appendix

---

## Materials and Methods

### 8.1. Animals and reagents

CD1 female mice were purchased from Charles River (Como, Italy). Animals were maintained under controlled conditions of 21°C, 60% air humidity and a light/dark cycle of 12:12 hours. Research on mice was conducted with permission from the Ministry of Health (No. 1100/2016-PR) in accordance with the guiding principles of European (No. 2010/63/UE) and Italian (No. 26/2014) laws protecting animals used for scientific research.

All reagents were bought from Sigma-Aldrich (Merck, Germany), unless otherwise stated.

### 8.2. Micro-Computed Tomography

#### 8.2.1. Ovaries preparation

Ovaries of eight-week-old females were isolated and, after removal of the fat residuals, individually fixed either in Carnoy's solution (60% Ethanol, 30% Chloroform, 10% Glacial acetic acid) for 8 hr at room temperature (RT), Bouin's solution (15 mL Picric acid, 5 mL 40% Formaldehyde, 1 mL Glacial acetic acid) for 2 hr at RT, or 4% Paraformaldehyde (PFA; 4 gr Paraformaldehyde in 100 mL 1X PBS) overnight (o/n) at 4°C with shaking.

The excess of fixative was washed out with its specific solvent. Following fixation, ovaries were treated at room temperature (RT) with 25% Lugol's solution (2.5 gr Potassium iodide and 1.25 gr Iodine in 100 mL distilled water), Phosphotungstic acid (0.2 gr PTA in 100 mL distilled water), or Uranyl acetate (1 gr in 100 mL distilled water). Different treatment times were tested, ranging from a minimum of 15 min up to a maximum of 8 hr. Each contrast agent was washed out with its solvent, for a period ranging from 30 sec to 15 hr.

#### 8.2.2. MicroCT imaging and 3D model reconstruction

Following contrast treatment, ovaries were fixed with orthodontic wax at the bottom of a 0.5 mL Eppendorf tubes filled with deionised water (dH<sub>2</sub>O) to avoid organ dehydration and shrinkage. Then, samples were scanned by microtomographic system Skyscan 1172 (BrukerMicroCT, Kontich, Belgium).

To determine the best preparation protocol, comparative studies of the different preparations were performed, at a source voltage of 60 kV, 165  $\mu$ A current, using a 0.5 mm aluminium filter, and adopting a scanning resolution of 5  $\mu$ m/pixel for nearly 25 min. Samples were rotated to 180° with a rotation step of 0.4°. Terminated the cone beam acquisition, the dataset acquired was of approximately 500 images in 16-bit tiff format. Three ovaries from three different females were fixed in 4% PFA, treated with Lugol's solution for 3 hours, washed for 15 hr and scanned at a source voltage of 59 kV, 167  $\mu$ A current, with a resolution of 1.5  $\mu$ m/pixel for nearly 5 hr. Sample were rotated to 180° with a rotation step of 0.1°. The scanning dataset consisted of about 2000 images in 16-bit tiff format. The final microCT sections were reconstructed using the NRecon software (BrukerMicroCT, Kontich, Belgium) in 8-bit jpg format (2000×2000 pixels). Then, sections were visualised with Fiji ImageJ (NIH) and follicles and blood vessels were manually segmented and isolated, combing the use of ROIs manager, thresholding and logical operations.

3D rendering of the follicular and vascular components was obtained with the volren module of the Avizo-9 software (Thermo Fisher Scientific) that approximates the organ isosurface from the segmented perimeters, resulting in a final model with a shaded surface and optimised transparency/opacity values.

### **8.2.3. Histology**

Histology was used as a cross-checking technique to validate the results of the microCT analysis. After microCT scanning, samples were individually dehydrated through an ascending ethanol series (50/70/90/100%), clarified with xylene and embedded in paraffin wax. Sagittal serial 6- $\mu$ m cross sections of the whole ovary were prepared using a RM2125RT microtome (Leica Biosystems) and, then, were stained with Mayer's Hematoxylin and 0.5% Eosin Y.

Sections were examined and digitalised at 63X magnification, using a Leica DMI6 light microscope equipped with a motorised XY scanning stage controlled by the LAS X Navigator stitching software (Leica Biosystems).

### **8.2.4. Follicle classification, counting and 3D localisation**

Watching through microCT sections of each ovary, follicular structures were individually counted and assigned to one follicle type among T4, T5, T6, T7, T8, and CL, based on a combination of morphological parameters and their size in diameter. The morphological features considered were the presence/absence and size of the antrum, the thickness of the follicle cells layer surrounding the oocyte [20], and the presence/absence of a well-visible zona pellucida. The follicle size was recorded at the major diameter with Fiji ImageJ software

(NIH), and compared to that measured on histological sections prepared after microCT acquisition. More specifically, follicles were classified as T8 when they showed a size in diameter of  $321.0 \pm 21.3 \mu\text{m}$ , the presence of a large single antrum cavity, a cumulus stalk, and a well-visible zona pellucida space in between the oocyte and the surrounding cumulus cells; T7 displayed a  $218.9 \pm 36.9 \mu\text{m}$  diameter, a single antrum cavity smaller than T8, the presence of a cumulus oophorus and a zona pellucida; T6 exhibited a  $137.0 \pm 24.9 \mu\text{m}$  diameter, several scattered small antral cavities and a zona pellucida space; T5 showed a  $89.0 \pm 11.2 \mu\text{m}$  diameter, the absence of antrum cavities, and the presence of a zona pellucida space separating the oocyte from the surrounding granulosa cell layers; T4, the smallest identifiable follicles by microCT, had a size in diameter of  $53.2 \pm 12.7 \mu\text{m}$ , they lacked of a zona pellucida and showed a lower radiopacity compared to that of the other follicle types.

The spatial reference system used for follicle localisation within each ovary was the anatomical orientation of the organ in relation to the anterior-posterior and dorsal-ventral body axes. The series of microCT sections of each ovary were divided into two halves along the dorsal-ventral axis, obtaining a dorsal and a ventral subset. Then, using Fiji ImageJ, each subset was partitioned into four, equally distributed, sectors, of which I and IV were positioned on the anterior region, while II and III on the posterior. A follicle was attributed to a specific sector when more than 50% of its volume belonged to that sector.

### 8.2.5. Statistical analysis

Student's t-test was used to evaluate differences in total follicles number or in the distribution of each follicle type along the anterior-posterior or dorsal-ventral axes. One-way ANOVA followed by the Bonferroni's *post-hoc* test were used to estimate differences in total follicles number or in the number of each follicle type present in the eight dorsal and ventral sectors. All statistical analyses were performed using the RStudio software (RStudio, Inc., version 1.1.423). Data were considered significantly different when  $p < 0.05$ .

## 8.3. Nano-Computed Tomography

### 8.3.1. Ovaries preparation

Ovaries of 4 to 25 dpn mice were isolated and fixed in 4% PFA o/n at 4°C with shaking. After the removal of fixative excess with dH<sub>2</sub>O, ovaries were treated with 25% Lugol's solution at RT for a contrast period depending on the sample size and synthesised in Table 9. Then, contrast agent was washed out with dH<sub>2</sub>O for 15 hr.

**Table 9.** Contrast times used for ovaries at different days post natal.

<b>dpn</b>	<b>Contrast time</b>
4	1 min
7	2 min
10	4 min
13	5 min
16	3 h
19	3 h
22	3 h
25	3 h

### 8.3.2. NanoCT imaging and 3D model reconstruction

As for microCT analysis, following contrast treatment, ovaries were placed in a nest of orthodontic wax fixed at the bottom of a 0.1 mL Eppendorf tube filled with dH<sub>2</sub>O to avoid dehydration and shrinkage. Samples were scanned by nanotomographic EasyTom XL system (RX Solutions). Analysis was performed at a source voltage of 60 kV, 100  $\mu$ A current reaching a scanning resolution in a range of 1-0.65  $\mu$ m/pixel. Samples were rotated with a step of 0.25°. The 16 dpn paraffin-embedded ovary was scanned with the same instrument at a source voltage of 45 kV, 130  $\mu$ A current, adopting a scanning resolution of 0.25  $\mu$ m/pixel and a rotation step of 0.15°. After the cone beam acquisition with either flat panel or CCD detector, the final nanoCT sections were reconstructed using the unreconstruction software (version 1.1) in 16-bit tiff format. Sections were visualized with Fiji ImageJ and follicles were 3D reconstructed as described above for microCT-scanned samples.

## 8.4. Tissue clearing

### 8.4.1. Immunostaining and clearing

After 4% PFA fixation, ovaries from six-week-old female mice were washed in 1X PBS, and gradually dehydrated in methanol (40/60/80/100%) at RT. Then samples were incubated in 33% methanol, 66% Dichloromethane (DCM) o/n at RT with shaking, washed twice in methanol for 15 min at RT, and treated with a solution of 5% H<sub>2</sub>O<sub>2</sub> /methanol o/n at 4°C with shaking. The day after, following a progressive rehydration to 1X PBS, samples were washed twice in PTx.2 (1x PBS/ 0.2% Triton X-100) for 1 hr at RT, permeabilized for 36 hr in Ptx.2/2.3% glycine/20% DMSO, and blocked for 36h at 37°C in PTx.2/10% DMSO/ 3% foetal bovine serum. Both permeabilisation and blocking were performed at 37°C with shaking. Then, after been incubated in 1:200 Alexafluor 488 anti-mouse (Abcam, USA) diluted in PTwH (PTx.2/ 0.001% heparin)/3% horse serum/10% DMSO for 72h at 37 °C with shaking, ovaries were washed in PTwH for a total of 15 hr and incubated for 24 hr with 0.5%

DAPI in 48h in PTwH at 37°C with shaking. After washing three times for a total of 15 hr in PTwH, samples were progressively dehydrated to 100% methanol o/n and, then, were incubated for 3h in 33%methanol/ 66% DCM at RT with shaking. Following two 15-minute washes in DCM, samples were kept o/n in Dibenzyl ether (DBE) for optical clearing.

### 8.4.2. Confocal imaging

For imaging ovaries cleared with iDISCO, samples were mounted into a well of 5 mm in diameter modelled with Sugru (inert modulable glue, Tesa, Beiersdorf, Germany), directly stack to a coverslip and filled with DBE. Confocal images were collected at 358 and 493 nm excitation wavelength by a Leica SP8 microscope equipped with a 25X NA 0.45 water objective with a 1.5 mm working distance (Leica Biosystems), a motorised XYZ stage and the LAS X software, reaching a final 1024x1024 image resolution. Stitching of multiple fields of view was performed with LAS X Navigator (Leica Biosystems).

### 8.4.3. Data analysis

Then, optical sections were visualised and processed with Fiji ImageJ. Specifically, a 3D rendering of the follicular and vascular components was obtained with the 3D viewer plug-in that approximates the texture-based volume.

## 8.5. Mass spectrometry

### 8.5.1. Ovary fixation and slides preparation

A 25 dpn mouse ovary was fixed in 10% Formalin, dehydrated, embedded in paraffin wax, and a total of 133 6- $\mu$ m serial sections were placed onto four conductive indium tin oxide (ITO) glass slides.

### 8.5.2. MALDI-MSI

After paraffin removal, sections were incubated with 20 ng/ $\mu$ L trypsin in a humid chamber o/n at 40°C for protein digestion. Then, by using the iMatrixSpray automated system, sections were coated with a matrix of  $\alpha$ -cyano-4-hydroxycinnamic acid (10 mg/mL in 50:50 acetonitrile:water w/0.4% trifluoroacetic acid) allowing peptides extraction and their *in-situ* crystallization. The ultrafleXtreme MALDI-TOF mass spectrometer (Bruker Daltonik GmbH) was calibrated using a mixture of standard peptides with m/z comprised in the range of 750-3150 (PepMix 1, Bruker Daltonik), and mass spectra of the ovarian sections were acquired in a reflectron-positive ionisation

mode, within the mass range of  $m/z$  750 to 3,500. The matrix was irradiated by a Smartbeam 3D laser with a pixel width of 20  $\mu\text{m}$ , allowing peptides ionisation. Then, mass spectra were imported into the SCiLS Lab MVS 2019c Pro software (<http://scils.de/>; Bremen, Germany) to perform intensity normalisation and remove background noise. Furthermore, peak-picking function was applied to remove weak spectra and select only mono-isotopic signals.

To perform *in-situ* histological localisation of each peptide, after matrix removal, histological serial sections were stained with the Mayer's Hematoxylin and 0.5% Eosin Y, digitalised using the ScanScope CS digital scanner (Aperio, Park Center Dr., Vista, CA, USA) and imported in the SCiLS Lab MVS 2019c Pro software to co-register each section with the corresponding mass spectra. Then, sections were analysed to classify each follicle, from T1 to T8, according to the classification proposed by Pedersen and Peters (1968). Starting from the equatorial section, identified as the largest section containing the nucleus of the oocyte, each follicle was annotated, section by section, using SCiLS Lab MVS 2019c Pro software.

### 8.5.3. LC-ESI-MS/MS

Following MALDI-MSI, the matrix was removed from the sections surface by washing with a 50:50 acetonitrile:water w/0.4% trifluoroacetic acid solution, and collected. Using an HETO vacuum concentrator (Thermo Scientific, Italy), this matrix solution was concentrated to an elution volume of 20  $\mu\text{L}$ , and then resuspended in 100  $\mu\text{L}$  of phase A (98/2/0.1; water/acetonitrile/trifluoroacetic acid) to reach a final volume of 120  $\mu\text{L}$ , before the storage at  $-20^\circ\text{C}$  prior to the LC-ESI-MS/MS analysis.

LC-ESI-MS/MS analysis was performed using a Dionex UltiMate 3000 rapid separation (RS) LC nano system coupled with an Impact HD™ UHR-QqToF (Bruker Daltonik, Germany). Matrix desalting and concentration were achieved by using a pre-column (Dionex, Acclaim PepMap 100 C18, cartridge, 300  $\mu\text{m}$ ) and peptides were separated by using a 50 cm column (Dionex, ID 0.075 mm, Acclaim PepMap100, C18) with a 120 min gradient at  $40^\circ\text{C}$  from 96% to 2% of phase A (0.1% formic acid), whilst in phase B 0.08% formic acid:- acetonitrile (80:20) was used.

### 8.5.4. Proteins identification

Peptides obtained were identified using the Mascot software (version 2.4.0), in Swissprot proteins database (accessed in January 2020; 561,568 sequences; 201,997,950 residues), with a peptide tolerance of 20 ppm, a fragment mass tolerance of 0.05 Da, and trypsin as digestive enzyme. Variable modifications were considered as +12 and +30 Da - as the results of formalin-fixed paraffin-embedded treatment and methionine oxidation, respectively – and an automatic decoy database search and a built-in Percolator algorithm were applied. Only

peptide sequences matched to a putative protein with  $p \leq 0.05$  were considered as positive results.

Then, each MALDI-MSI peptide signal was recognised as a protein when a mass error < 100 ppm ([https://warwick.ac.uk/fac/sci/chemistry/research/barrow/barrowgroup/calculators/mass\\_errors/](https://warwick.ac.uk/fac/sci/chemistry/research/barrow/barrowgroup/calculators/mass_errors/)) was found between the m/z values observed during MALDI-MSI and LC-ESI-MS/MS.

### **8.5.5. STRING (Search Tool for the Retrieval of Interacting Genes/Proteins) analysis**

Protein-Protein Interaction Networks Functional Enrichment Analysis of multiple proteins was performed by using STRING (version 11.0) with a “full network” type, “0.9” confidence in the interaction score, and selecting “Textmining”, “Experiments”, “Databases”, “Co-expression”, “Neighborhood”, “Gene Fusion” and “Co-occurrence” as active interaction sources.

### **8.5.6. PubMed analysis**

We conducted a search on PubMed and retrieved all relevant publications on mammalian models obtained by crossing each individual protein name with a keyword such as “ovarian”, “ovary”, “follicle”, “follicular”, “oocyte”, “meiosis”, or “cumulus”.

### **8.5.7. Statistical analyses**

Using SCiLS Lab MVS 2019c Pro software, Principal Component Analysis (PCA), Receiver operating characteristic (ROC) analysis and were performed on MALDI-MSI mass spectra of individual follicle,

PCA, was used to explore data in a new simplified 2D or 3D space, with Pareto scaling. In ROC analysis, a threshold  $\geq 0.8$  was applied.

## **8.6. Confocal histology**

### **8.6.1. Ovary preparation and staining**

Ovaries of 25 dpn females were fixed with Bouin’s solution, dehydrated through an ascending ethanol series (50/70/90/100%), clarified with xylene, and embedded in paraffin wax. Sagittal serial 6- $\mu$ m cross sections were prepared using a RM2125RT microtome and stained with Mayer’s Hematoxylin and 0.5

% Eosin Y or only one of these dyes at a time. Then, sagittal serial 20  $\mu\text{m}$  sections of the whole ovary were stained with 0.5% Eosin Y for 1min and 30sec.

### **8.6.2. Two-photon imaging**

Ovarian sections were analysed with a in lab-assembled two-photon microscope equipped with a Ti:Sapphire laser source (Tsunami, Spectra-Physics), a CoolSNAP EZ CCD camera (Photometrics), a Piezomotor Microstep Driver 101 stage, an oil-immersion 60x objective (Nikon), and controlled by the  $\mu$ Manager software (UCSF). Image acquisition was performed at excitation wavelength of 830 nm and with 1.5  $\mu\text{m}$  z-step.

### **8.6.3. Confocal imaging**

Using a Leica SP8 confocal microscope equipped with a motorised XY stage and controlled by the LAS X Navigator stitching software (Leica Biosystems), sections were examined and digitalised at 40 or 63X magnification. 20  $\mu\text{m}$  z-stack of individual follicles or entire sections were acquired at 1024x1024 resolution, a ScanSpeed between 400 to 100 Hz, line average of 2, a z-step of 1  $\mu\text{m}$  and a laser excitation wavelength of 520 nm.

### **8.6.4. Data processing and analysis**

To make the fluorescent signal more homogeneous throughout the section thickness, 20  $\mu\text{m}$  z-stack were processed by using the ImageJ Plane Brightness Adjustment plug-in, with Slope = 3.000, Threshold = 30.000000000 and MaxFactor = 8.000000000. Then antral oocytes were classified in SN or NSN according to the organisation of the Eosin-positive chromatin around the nucleolus.

## **8.7. Histology**

### **8.7.1. Ovary preparation and staining**

After fixation in 4% PFA or Bouin's solution, ovaries of six/eight-weeks-old CD1 females were individually dehydrated through an ascending ethanol series (50-70-90-100%), clarified with xylene and embedded in paraffin wax. Sagittal serial 5- $\mu\text{m}$  cross sections of the whole ovary were prepared using a RM2125RT microtome and, then, were stained with Mayer's Hematoxylin and 0.5% Eosin Y.

### **8.7.2. Sections digitalisation and analysis**

Sections were digitalised at 40x magnification, using a Leica DMi6 light microscope equipped with a motorised XY scanning stage controlled by the LAS X Navigator stitching software (Leica Biosystems). Tiff images were analysed with Adobe Photoshop CC 2015 to select all those structures with pixels characterised by a similar orange/brown colour value. The Magic wand function with low tolerance (10) was used as sampling tool for the first orange/brown pixel and, then, the selection was extended to similar pixels.